Novel concept for the formulation of printing pastes for printable electronics based on the capillary suspension phenomenon

Zur Erlangung des akademischen Grades eines
Doktors der Ingenieurwissenschaften
(Dr.-Ing.)

bei der Fakultät für Chemieingenieurwesen und Verfahrenstechnik
des Karlsruher Instituts für Technologie (KIT)

genehmigte
DISSERTATION

von

Dipl.-Ing. Monica Schneider
aus Würzburg

Referent: Prof. Dr. Norbert Willenbacher
Korreferent: Prof. Dr. Wilhelm Schabel
Tag der mündlichen Prüfung: 24. März 2017

Acknowledgments

First of all I want to thank my supervising professor Prof. Dr. Norbert Willenbacher for offering me the chance to grow with a challenging research topic, helping me with advice, motivation and dissipating my doubts when necessary.

Many thanks also to Prof. Dr.-Ing. Dr. h. c. Wilhelm Schabel for being the second reviewer of this thesis.

Further I want to thank Bernhard Hochstein and Erin Koos for their support, advice and fruitful discussions.

I also want to thank Suresh Garlapati Kumar, Florian Gang and Klaus Plewa for their help in the external laboratories. Many thanks also to Maximilian Pospischil from the Fraunhofer Institute in Freiburg.

Thanks also to my smart and eager students Johannes Fath, Karim Abdel Al and Tobias Bek.

A lot of fruitful discussions also took place during lunch with my lovely colleagues Clara Weis, Susanne Wollgarten, Dirk Sachsenheimer and Leon Jampolski. Many thanks to them for supporting me in times of despair and giving me a lot of happy and unforgettable moments in the lab and leisure time.

Last but really not least, I also want to thank my husband Christian for his support, motivation and endurance to finish this thesis.

Abstract

The rheology of suspensions can be altered dramatically by adding small amounts of a secondary liquid, which is not miscible with the continuous phase of the suspension. The addition of the secondary liquid changes the suspension rheology from fluid-like or weakly elastic to gel-like with high yield stresses possible depending on the amount of added liquid. Small droplets of the secondary liquid form a stable network together with the solid phase of the suspension regardless of whether the secondary liquid wets the solid better or worse than the bulk phase. These so-called capillary suspensions are divided into pendular and capillary state systems depending on the three-phase contact angle θ. The contact angle θ is the angle made by the secondary fluid against the particles when surrounded by the bulk fluid. A capillary suspension with contact angles $\theta < 90°$ is placed in the pendular state with the secondary liquid forming small liquid bridges between adjacent particles. For contact angles $\theta > 90°$ solid phase and secondary liquid form a capillary state network, where small volumes of secondary liquid are enclosed by particle clusters. The capillary suspension phenomenon has been demonstrated as versatile tool, for example for the formulation of low-fat cocoa spreads or as novel processing route for highly porous ceramics.

This thesis focuses on the formulation of a novel, conductive printing paste for application in the printable electronics industry based on the capillary suspension phenomenon which excludes typical components of established formulations such as rheological additives and stabilizers. First experiments were conducted with a model system, here titanium oxide (TiO_2) dispersed in n-octanol and water as secondary liquid. The addition of the secondary liquid leads to a strong pendular state network and the strength of the capillary network as function of the secondary liquid content was quantified by measuring the yield stress. Viscosity was investigated at low shear rates ($\dot{\gamma} < 100\ s^{-1}$) and high shear rates ($\dot{\gamma} > 100\ s^{-1}$) to examine the applicability for the printing process. The TiO_2 based capillary suspensions show a shear-thinning viscosity function, which is favored for the printing process. The low shear viscosity is gradually increased by the addition of the secondary liquid and therefore the capillary network avoids sedimentation or agglomeration when the paste is at rest. At high shear rates the capillary network collapses and viscosity is determined by the solids loading only. Furthermore, the response of TiO_2 based capillary suspensions with different amounts of added secondary liquid to high deformations was investigated by oscillatory shear. A printing process was simulated by a measurement procedure consisting of three intervals, starting with a rest interval and therefore a low deformation amplitude, followed by the simulated printing process with a high deformation amplitude and finally again a rest interval. It is shown, that the addition of the water leads to a tunable increase of elasticity, which is able to recover promptly after a high deformation interval. This is a beneficial characteristic for the printing process, because spreading of the paste on the substrate is suppressed and shape accuracy provided. Finally, the capillary suspensions with 0 %, 3 % and 5 % secondary liquid were printed using a dispenser and the shape of the printed lines was characterized using a 3d

laser microscope. The height to width aspect ratio of the profile and contact angle formed between printed line and substrate are discussed as function of the secondary liquid amount. It is shown that the secondary liquid and the inherent capillary network support the shape accuracy of the printed pattern as spreading on the substrate is suppressed. This leads to an increase of the aspect ratio and contact angle by a factor of three and the line width drops down to 40 % of the width achieved with the suspensions with no added secondary liquid.

Additionally, a model system was used to study the drying behavior of capillary suspensions with varying fractions of secondary liquid. Thin layers were coated on polyester foils and dried at room temperature in a fume hood. The evaluation of the dry films shows a remarkable correlation of crack formation and secondary liquid content, which is a decrease in crack number and size for increasing secondary liquid amounts. The same experiments were also made with zinc oxide (ZnO) and aluminum oxide (Al_2O_3) particles and the result is again an increase in yield stress with increasing secondary liquid amount when using n-octanol as bulk and water as secondary liquid phase. And again, crack formation is reduced for increasing secondary liquid content. Besides of crack formation, also drying rate is influenced by the secondary liquid content. Infrared absorption measurements during drying were performed for the TiO_2 suspensions with varying water fractions. These experiments indicate that drying time is significantly reduced when adding water to the suspension.

Further experiments were performed with conductive particles, such as nickel and silver particles. Capillary suspensions were made using either paraffin oil (bulk phase) and water-dimethyl formamid (DMF) mixtures (secondary liquid) as solvent combination or, alternatively, using terpineol and water. Yield stress measurements were performed, in order to investigate the formation of a capillary network and the strength of the resulting network. Viscosity measurements were made with nickel based capillary suspensions showing a shear-thinning behavior, which is preferred for printing pastes. The low-shear viscosity of the suspension is gradually increased due to the addition of increasing amounts of secondary liquid. This high viscosity of capillary suspensions at low shear rates avoids sedimentation and agglomeration of the solid phase, which is an important feature during storage of the paste. The high-shear viscosity remains unaffected by this stabilization method and is only influenced by the solid fraction of the conductive particles. Furthermore, the influence of interfacial tension on the strength of the capillary network was investigated using nickel particles dispersed in paraffin oil and adding either water, a water-DMF mixture (50:50 by volume) or pure DMF as secondary liquid. As expected, a correlation was found between network strength and interfacial tension. The higher the initial interfacial tension between the solvent combinations, the higher was the yield stress of the capillary suspension at a constant secondary liquid content.

To investigate the electronic properties of the metal based capillary suspensions, samples were coated on a heat stable substrate and sintered. The sheet resistivity of each layer was measured with the van-der-Pauw method and compared with the resistivity of commercial samples or formulations following

a patent. Together with the sheet thickness measurements made after the sintering step, these experiments showed that capillary suspensions are able to create thinner, and therefore denser films after sintering with about twice the conductivity of the commercial samples and the pastes based on the patent. The profiles of the coated, wet layers, which were applied by stencil printing, were investigated with a 3D laser microscope and revealed that the capillary suspension based samples are able to compete with the commercial pastes. It is possible to generate profiles with steep edges when printing the capillary suspensions, which can be attributed to the high yield stress on account of the capillary network, and this is a desired characteristic when printing fine lines. For the capillary suspensions, the line width of the coated lines is significantly reduced with addition of the secondary liquid. The capillary suspension samples barely spread on the substrate maintaining the original stencil opening size.

Finally, this thesis demonstrates further experiments to improve conductivity of the metal layers made from capillary suspensions, e.g. by employing flake shaped particles, a polydisperse size distribution of the solid phase or a variation of the sintering atmosphere.

Zusammenfassung

Die Rheologie von Suspensionen kann durch die Zugabe von geringen Mengen einer zweiten Flüssigkeit, welche mit der kontinuierlichen Phase nicht mischbar ist, signifikant verändert werden. Das Fließverhalten der Suspension ändert sich von flüssig oder schwach viskoelastisch zu gelartig und es entstehen sogenannte Kapillarsuspensionen. Die Zugabe der Zweitflüssigkeit führt zu einem Anstieg der Viskosität und zur Ausbildung einer Fließgrenze oder zu einem deutlichen Anstieg einer bereits vorhandenen Fließgrenze, welche abhängig ist von der zugeführten Menge an Zweitflüssigkeit. Kleine Tropfen der zweiten flüssigen Phase lagern sich zwischen den Partikeln an und formen so, gemeinsam mit der festen Phase, ein stabiles Netzwerk. Die Ausbildung eines solchen Netzwerkes ist dabei unabhängig von den Benetzungseigenschaften der Zweitflüssigkeit. Unterschieden wird allerdings zwischen dem sogenannten „pendular state“ und dem „capillary state“. Im ersten Fall benetzt die Zweitflüssigkeit die Partikel besser als die kontinuierliche Phase. Für den Drei-Phasen-Kontaktwinkel θ gilt hier $\theta < 90°$ und die Zweitflüssigkeit lagert sich in kleinen Flüssigkeitsbrücken zwischen den Partikeln an. Für $\theta > 90°$ ist die kontinuierliche Phase besser benetzend und ein stabiles Netzwerk entsteht hier durch die Abschirmung kleiner Tropfen der Zweitflüssigkeit durch die Bildung von Partikelclustern. Das Prinzip der Kapillarsuspensionen wurde schon als vielseitiges Konzept vorgestellt, zum Beispiel zur Formulierung von fettreduzierten Schokoladenaufstrichen oder als innovatives Verfahren zur Herstellung hochporöser Keramiken.

Diese Dissertation beschäftigt sich nun mit der Formulierung von neuartigen, leitfähigen Pasten zur Herstellung von gedruckten Elektronikbauteilen unter Ausnutzung des Phänomens der Kapillarsuspensionen. Dies beinhaltet die Entwicklung eines neuen Formulierungskonzeptes ohne die Verwendung von rheologischen Additiven oder Stabilisatoren, wie sie in klassischen Formulierungen üblich sind. Erste Experimente wurden mit einem Modelsystem durchgeführt, hier Titandioxid (TiO_2) Partikel dispergiert in n-Octanol und Wasser als Zweitflüssigkeit. Die Zugabe der Zweitflüssigkeit führt zu einem starken Netzwerk im „pendular state“, dessen Festigkeit als Funktion der Menge an Zweitflüssigkeit mittels Fließgrenzenmessungen quantifiziert wurde. Zusätzlich wurde auch die Viskosität im niedrigen ($\dot{\gamma} < 100\ s^{-1}$) und hohen ($\dot{\gamma} > 100\ s^{-1}$) Scherratenbereich untersucht, um die Anwendbarkeit für den Druckprozess zu untersuchen. Alle untersuchten Suspensionen zeigen ein strukturviskoses Verhalten, was für die Anwendung als Druckpaste bevorzugt ist. Bei niedrigen Scherraten ist die Viskosität eine Funktion der Menge an Zweitflüssigkeit und steigt mit zunehmendem Anteil an Zweitflüssigkeit. Im Ruhezustand, z.B. während der Lagerung, verhindert das Kapillarnetzwerk so die Sedimentation und Agglomeration der festen Phase. Im hohen Scherratenbereich ist die Viskosität unabhängig von der Zweitflüssigkeit und nur eine Funktion des Feststoffvolumenanteils. Große Deformationen wie sie im Druckprozess auftreten wurden mittels oszillatorischer Messungen simuliert. Der Druckprozess wurde hierfür in drei Intervalle geteilt. Diese sollen den Ruhezustand (kleine Deformationsamplitude), den Druckprozess (große

Deformationsamplitude) und den abschließenden Ruhezustand (kleine Deformationsamplitude) darstellen, um die korrespondierenden, viskoelastischen Materialeigenschaften der Kapillarsuspensionen mit unterschiedlichen Zweitflüssigkeitsanteilen zu untersuchen. Diese Versuche haben gezeigt, dass Kapillarsuspensionen und das damit verbundene Netzwerk aus Partikel und Zweitflüssigkeit im Ruhezustand eine hohe Elastizität aufweisen, welche sich zügig nach dem simulierten Druckprozess regeneriert und somit ein sauberes Druckbild ohne Verlaufen unterstützt. Abschließend wurde die auf TiO_2 basierten Kapillarsuspensionen mittels Dispenser verdruckt und die Profile der gedruckten Linien mit einem 3D Lasermikroskop untersucht. Der Einfluss des Zweitflüssigkeitanteiles und die daraus resultierende Güte des Druckmotives wurden anhand des Aspektverhältnisses aus Höhe und Breite der Profile und dem Kontaktwinkel zwischen Probe und Substrat beurteilt. Durch die Zugabe der Zweitflüssigkeit und das daraus resultierende Kapillarnetzwerk wird ein Verlaufen des Druckmotives auf dem Trägermaterial unterdrückt und somit die Druckqualität verbessert. So erhöht sich der Kontaktwinkel und das Aspektverhältnis durch die Zugabe von 5 vol% Zweitflüssigkeit um den Faktor drei und die Linienbreite fällt auf 40% des Wertes, der mit der Suspension ohne Zweitflüssigkeit erzielt werden konnte.

Zusätzlich zu den Fließ- und Druckeigenschaften, wurde das Modelsystem auch genutzt, um die Trocknung von Kapillarsuspensionen als Funktion der zugesetzten Menge an Zweitflüssigkeit zu untersuchen. Hierzu wurden kleine Mengen der Suspension als dünne Filme auf Polyester-Folien aufgebracht und zur Trocknung bei Raumtemperatur in einen Abzug gelegt. Die Auswertung der getrockneten Filme zeigt, dass ein bemerkenswerter Zusammenhang zwischen Zweitflüssigkeitsanteil und Rissbildung existiert. So ist die Anzahl der Risse und deren Größe mit zunehmender Menge an Zweitflüssigkeit in der ursprünglichen Kapillarsuspension Schritt für Schritt zurückgegangen. Trocknungsversuche wurden zusätzlich auch mit Zinkoxid (ZnO) und Aluminiumoxid (Al_2O_3) Partikeln durchgeführt. Diese wurden ebenso in n-Octanol dispergiert und Wasser als Zweitflüssigkeit zugegeben. Mit Zugabe der Zweitflüssigkeit bildet sich ein starkes Netzwerk aus, was in einem Anstieg der Fließgrenze deutlich wird. Ähnlich zu den TiO_2 Proben, wird auch die Rissbildung wird mit zunehmendem Zweitflüssigkeitsanteil unterdrückt. Neben der Morphologie der getrockneten Proben mit ursprünglich unterschiedlichem Zweitflüssigkeitsanteil, unterscheiden sich diese auch hinsichtlich ihrer Trocknungsgeschwindigkeit. Infrarot-Absorptionsmessungen deuten darauf hin, dass die Trocknung durch die Zugabe der Zweitflüssigkeit signifikant beschleunigt wird.

Weitere Versuche wurden mit leitfähigen Silber- und Nickelpartikeln durchgeführt. Kapillarsuspensionen wurden mit Paraffinöl als Hauptphase und Wasser bzw. Wasser-Dimethylformamid(DMF)-Gemischen als Zweitflüssigkeit hergestellt. Alternativ wurde Terpineol als Hauptphase eingesetzt. Fließgrenzenmessungen wurden durchgeführt, um die Ausbildung eines Kapillarnetzwerkes und dessen Festigkeit zu untersuchen. Die Bestimmung der Viskosität von Nickel-basierten Kapillarsuspensionen mit variierendem Zweitflüssigkeitsanteil zeigt ein strukturviskoses

Fließverhalten, wie es für den Druckprozess gewünscht ist. Im niedrigen Scherratenbereich ist die Viskosität umso höher je mehr Zweitflüssigkeit enthalten ist. Durch diese erhöhte Viskosität kann die Stabilität der Paste zum Beispiel während der Lagerung gewährleistet werden. Im hohen Scherratenbereich zeigt die Formulierungsmethode als Kapillarsuspension keinen Einfluss. Die Viskosität ist unabhängig von der Menge an Zweitflüssigkeit und nur eine Funktion des Volumenanteils der festen Phase. Der Einfluss der Grenzflächenspannung zwischen Haupt- und Zweitflüssigkeit wurden anhand von Nickelpartikeln in Paraffinöl untersucht. Als Zweitflüssigkeit wurde Wasser, ein Wasser-DMF-Gemisch (je 50 vol%) und reines DMF eingesetzt. Wie erwartet, zeigt sich hier ein direkter Zusammenhang zwischen Grenzflächenspannung und gemessenen Fließgrenzen. Je höher die Grenzflächenspannung der Lösungsmittelkombination, desto höher war die gemessene Fließgrenze der jeweiligen Kapillarsuspension bei einer konstanten Menge an Zweitflüssigkeit.

Um die elektrischen Eigenschaften der Kapillarsuspensionen mit Metallpartikeln zu untersuchen, wurden diese auf hitzebeständige Substrate aufgetragen und gesintert. Die resultierenden Schichtwiderstände wurden mittels der Van-der-Pauw-Methode bestimmt und mit den Werten für kommerzielle Druckpasten bzw. für ein patentiertes Formulierungsrezept verglichen. Zusätzlich wurden auch die Schichtdicken der gesinterten Filme untersucht. Anhand von Schichtdicken und Widerstandswerten kann gezeigt werden, dass Kapillarsuspensionen nach dem Sinterprozess dünnere und somit dichtere Schichten und zeitgleich auch eine hinreichend gute Leitfähigkeiten (ca. Faktor zwei gegenüber den kommerziellen Produkten) aufweisen. Die Profile der per Schablonendruck applizierten, feuchten Schichten wurden mit einem 3D Lasermikroskop untersucht. Mit Kapillarsuspensionen können aufgrund der hohen Fließgrenzen Profile mit steilen Kanten generiert werden, welche im Feinliniendruck gewünscht sind. Kapillarsuspensionen sind somit konkurrenzfähig gegenüber bereits etablierten, kommerziellen Pasten. Für Kapillarsuspensionen zeigt sich auch, dass die Linienbreite des Druckmotives durch die Zugabe der Zweitflüssigkeit deutlich reduziert wird. So spreiten Kapillarsuspensionen mit entsprechendem Zweitflüssigkeitsanteil kaum auf dem Substrat und erlauben so eine präzise Darstellung des Druckmotives beim hier verwendeten Schablonendruck.

Im letzten Abschnitt werden weitere Formulierungsansätze für Kapillarsuspensionen vorgestellt, die sich darauf konzentrieren die bisher erzielten Leitfähigkeiten zu verbessern. Zum Beispiel wurden Nickelplättchen statt kugelförmiger Partikel verwendet, die Partikelgrößenverteilung oder auch die Sinteratmosphäre variiert.

Table of Content

Acknowledgments I

Abstract III

Zusammenfassung VI

Table of Content IX

List of symbols XI

1 Introduction 1

1.1 State of the art 1

1.2 Scope of this work 2

2 Theoretical background 4

2.1 Capillary Suspensions 4

2.2 Printable Electronics 8

2.2.1 Aims in Photovoltaics 9

2.2.2 Screen printing and Rheology 10

2.2.3 Paste formulation 11

2.3 Drying and Crack formation 12

3 Materials and Methods 14

3.1 Sample preparation 14

3.1.1 TiO_2 and ZnO based capillary suspensions 16

3.1.2 Nickel and silver based capillary suspensions 16

3.1.3 Preparation of the organic vehicle 17

3.1.4 Synthesis of the silver nanoparticle dispersion 18

3.2 Contact angle measurements 18

3.3 Interfacial tension 19

3.4 Rheological characterization 20

3.4.1 Yield Stress 20

3.4.2 Viscosity 21

3.4.3 Structural Recovery 23

3.5 Coating and Printing 24
3.6 Heat treatment 25
3.7 Sheet Resistance Measurement 26
3.8 3D Laser Microscopy 26
3.9 Infrared spectroscopy 27
4 Results and discussion 29
4.1 Capillary suspensions with TiO_2 particles - a model system 29
4.1.1 Influence of the secondary fluid content on the rheological properties 29
4.1.2 Structural recovery of the capillary network after LAOS 31
4.1.3 Printing TiO_2 capillary suspensions 34
4.1.4 Yield stress and crack formation as function of secondary fluid content 35
4.1.5 Crack formation as function of secondary fluid content for ZnO and Al_2O_3 particles 38
4.1.6 Drying time as function of secondary fluid content 39
4.2 Capillary suspensions with metal particles 40
4.2.1 Rheological properties 40
4.2.2 Electrical properties 44
4.2.3 Shape Profile of wet contact lines 46
4.2.4 Capillary suspensions with nickel flakes 48
4.2.5 Comparison of nitrogen and hydrogen as sintering atmosphere 50
4.2.6 Using particles with a polydisperse size distribution 52
4.2.7 Metal capillary suspensions with low solid loading 54
5 Summary 55
References 58
List of figures 65

List of symbols

Greek Symbols:

θ	wetting angle
γ	surface tension
φ	volume fraction
σ	stress
ρ	density
Θ	angle
δ	phase angle shift
ν	wave number
λ	wave length

Latin symbols:

D	diameter
d	distance
F	force
g	gravitational constant
G	modulus
h	thickness
L	length
M	coordination number
M_w	Molar weight
n	refractive index
p	pressure
r	radius
R	resistance
rpm	rounds per minute
S	saturation
s	separation distance
t	temperature
v	piston speed
V	volume
x	coordinates
y	coordinates

Indices:

2l	two liquid
c	capillary
crit	critical
dr	droplet
l	liquid
LVE	linear viscoelastic
m	melting
max	maximum
p	pore
pen	penetration
rcp	random close packing
w	wall
y	yield

1 Introduction

1.1 State of the art

Almost every step we make today is accompanied by electronic devices ranging from microscopic transistors in our computers and smartphones or, thinking in large scale, supported by e.g. manufacturing robots. Producing electronic devices via printing is preferable over other techniques because it is inexpensive and time efficient due to the easy transition to large-scale production with ready availability of industrial devices. This demand for printable electronics is rapidly increasing with the potential to grow to a $50 billion global market in the next few years.[1] Solution-based deposition has become increasingly popular due to the decrease in material wastage and ambient pressure processing at moderate temperatures leading to lower investment costs over other methods such as physical vapor deposition.[2] Printable electronic products range from microscale devices as well as large scale units, made of either inorganic (e.g. front side metallization of solar cells) or organic material systems (e.g. OLEDs). A large variety of established printing equipment can be used during manufacturing, such as screen printing, where the ink is pushed through a partially permeable screen; gravure printing or flexography, where the ink is transferred roll to roll; or via drop-on-demand methods like inkjet printing, where the controlled deposition of micro-sized droplets can produce fine structures.[3] Ink formulations have to meet several requirements depending on the printing technique and product application. For example, highly viscous printing pastes are necessary for the screen printing process (0.5-50 Pas), whereas inkjet printing requires far lower viscosities (0.001-0.04 Pas).[3] Rheological additives, usually polymers, are used to adapt the flow behavior. Furthermore, inks containing insoluble components need a stabilizing agent to avoid sedimentation or agglomeration, such as e.g. alkanethiols on gold nanoparticles.[4] Also other organic additives such as binders are often included in the paste formulation. A major disadvantage of these crucial components is the inability to completely remove the additives in subsequent processing steps (e.g. annealing).[3–6] Residues of the additives can detrimentally affect the product properties, e.g. by reducing the conductivity.

To avoid these impurities, a novel formulation strategy based on capillary suspensions is presented here. In capillary suspensions, sedimentation of particles is inhibited by adding of small amounts of a secondary liquid to a suspension, which is immiscible with the bulk phase.[7–9] The secondary liquid forms a sample-spanning network of particles and droplets, which avoids particle agglomeration and also dramatically changes the rheological behavior from fluid-like to gel-like or from a weak gel to a strong gel. The viscosity and yield stress of capillary suspensions can be tuned by varying the amount of secondary liquid. Capillary suspensions can be created regardless of whether the secondary liquid wets the solid phase better or worse than the bulk fluid.[10,11] Further additives become superfluous in this kind of formulation as the capillary network is able to stabilize the particles from sedimentation

and also acts as a rheology control agent, which controls the flow behavior and hence printing properties. As a further advantage, the secondary liquid can be easily removed by evaporation leading to high product purity. Capillary suspensions were previously shown to increase the edge sharpness of coated layers for lithium-ion battery electrode pastes.[12] The new formulation route is demonstrated here for nickel (Ni), silver (Ag) and titanium dioxide (TiO_2), as a model system, and can be easily adapted to other inorganic particulate systems. Nickel layers have been applied, e.g., in multilayer capacitors in order to reduce production costs by replacing the internal electrodes with cheaper base metal electrodes, or as porous electrodes for molten carbonate fuel cells (MCFCs).[13–15] Silver particle based pastes are employed in the manufacture of the front side metallization of silicon solar cells as well as other specialized applications.

Besides of the improved product properties regarding the shape of the printed lines, capillary suspensions also offer the ability to suppress crack formation. Crack formation during drying is an ubiquitous phenomenon important in soil science as well as industrial material and processing development. Dried mud, paint coatings, ceramics and many other materials can show this effect after solvent evaporation. Understanding crack formation in particle films and developing strategies to suppress crack formation is an important field of research, as desired product properties generally decline with the occurrence of cracks. Hard particle coatings, used in e.g. printed electronic devices such as battery electrodes,[16] photonic crystals or antireflective coatings,[17,18] but also filtration operations or processing of catalysts and ceramic materials are plagued by this phenomenon.[19] Common solutions proposed to achieve fracture-free layers from suspensions include the use of soft particles with a sufficient low glass transition temperature to allow for a relaxation of the drying induced inter-particle tensile stress by deformation, the addition of a plasticizer, or a blend of soft and hard particles to provide the required deformability of the particles.[20,21] Another approach is to coat a colloidal precursor. The evaporation of the solvent leads to an in-situ growth of the particles, which replaces the arising void volume and thus avoids crack formation while drying.[22] Certain applications preclude the use of soft particles or plasticizers and the use of a multi-step approach can be time consuming and costly.

Capillary suspensions offer a generic novel strategy to suppress crack formation during drying of particle suspensions by taking advantage of capillary forces inferred via the addition of a small amount of a second liquid that is immiscible with the main or bulk fluid of the suspensions. The phenomenon of capillary suspensions and the benefits of this material class regarding the printing and drying behavior will be described in detail in the following chapters.

1.2 Scope of this work

This thesis shows the formulation of capillary suspensions based on oxidic particles (titanium oxide TiO_2, zinc oxide ZnO and aluminum oxide Al_2O_3) and metal particles (silver Ag and nickel Ni),

aiming at the development of printing pastes which show the required rheological properties, such as shear thinning and a high viscosity at low shear rates. On the one hand to avoid phase separation during the storage time and on the other hand in order to reduce spreading of the freshly printed ink pattern on the substrate. The benefit of using the capillary suspension phenomenon as formulation route is the total relinquishment of any additives necessary to control the rheology or stabilizers usually utilized to ensure a long shelf-life without phase separation.

In the first section the results gained with the oxidic particles are presented. The yield stress was measured in order to evaluate the strength of the capillary network. Furthermore, relaxation after high shear, as it appears during printing, was investigated and the ability of the network to outlast this kind of stress. For this purpose TiO_2 particles were dispersed in n-octanol and stabilized as capillary suspension by adding water as secondary liquid. Besides of the rheological properties during high and low shear, also the drying behavior, e.g. drying time and crack formation, after coating the suspensions as films has been investigated. The change of the surface appearance has also been examined for ZnO and Al_2O_3 particles dispersed in n-octanol and using water as stabilizing secondary liquid.

The second part shows the formulation of metal based capillary suspensions with nickel and silver particles of different size and shape. Low and high shear viscosity measurements have been performed with the capillary suspensions made with spherical nickel particles in order to be able to judge their qualification for the printing process. Both, nickel and silver capillary suspensions were coated on quartz carriers, sintered and the resulting electric resistance measured via the Van-der-Pauw method. For comparison with existing commercial formulations, silver pastes were prepared following supplier`s recipe and samples characterized the same way as for the capillary suspensions. Also commercial silver pastes were investigated. Different approaches will be presented to improve the electronic properties of the printed and sintered films, such as using irregular shaped particles or polydispers size distributions in the formulation step.

2 Theoretical background

2.1 Capillary Suspensions

Capillary forces can lead to the formation of a particulate gel comprising a sample-spanning particle network, regardless of whether the secondary liquid wets the particles better or worse than the bulk phase.[7] Such ternary particle-liquid-liquid systems are termed capillary suspensions.[7,10] Two types of capillary suspensions are distinguished depending on the two-liquid wetting angle $\boldsymbol{\theta_{2l}}$ the secondary liquid forms against the solid surface in the bulk phase environment. The terminology has been derived from the theory of wet granular material.[23] In the pendular state ($\boldsymbol{\theta_{2l} < 90°}$), the secondary liquid wets the solid phase better than the continuous phase and forms pendular shaped bridges between the particles. In the case where $\boldsymbol{\theta_{2l} > 90°}$, termed the capillary state, the particles form clusters around small volumes of the second liquid.[8]

Capillary suspensions can clearly be distinguished from other particle-liquid-liquid systems. Figure 1 gives an overview of possible states for particles suspended in an emulsion for varying relative volume fractions of the two involved liquids and the solid phase.

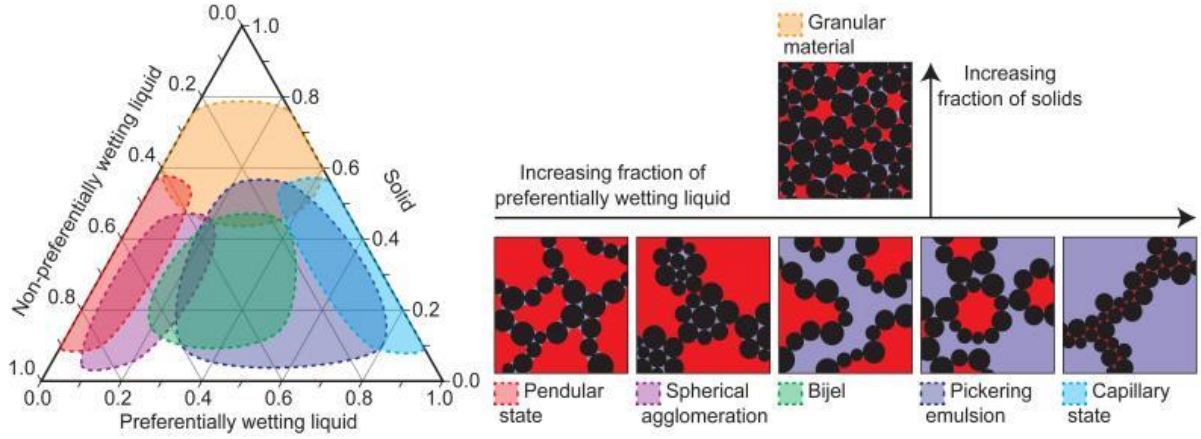

Fig. 1. Left: Ternary diagram of particle-liquid-liquid systems showing the approximate regions of stability as a function of the relative volume fractions. Right: Corresponding diagram showing the particle-liquid-liquid systems in the different states, when increasing the fraction of the preferentially wetting liquid.[24]

For capillary suspensions, either in the pendular or in the capillary state, traces of the secondary fluid are sufficient to create a stable system, placing these materials at the edges of the ternary diagram. Moreover, the droplets of secondary liquid with volume V_l are typically smaller or similar to the particle volume $\sim r^3$ ($\frac{V_l}{r^3} \leq 1$). Starting from the pendular state higher amounts of the preferentially wetting liquid lead at first to spherical agglomeration, where particles are trapped in a bigger droplet of the preferentially wetting liquid. For increasing liquid volume fractions of the better wetting fluid Bijels, a bicontinuous network of two immiscible liquids stabilized with jammed particles,[25] are

formed, followed by the Pickering emulsions. For the latter, droplets with $\frac{V_l}{r^3} \gg 1$ are covered with particles and gelation occurs due to the attractive van der Wals force between the particles on the surface of adjacent droplets. In the pendular state the gelation of the capillary suspension is caused by capillary forces exerted by the small liquid bridges between the particles. The amount of secondary liquid corresponds to the number of available liquid bridges, whereas wetting angle and interfacial tension directly affect the strength of the capillary force.

As mentioned before, terminology of capillary suspensions has been adapted from wet granular matter science, where particles surrounded by air or any other gas are also connected by pendular, liquid bridges with the surface tension γ and the wetting angle θ the liquid forms against the solid, see figure 2.

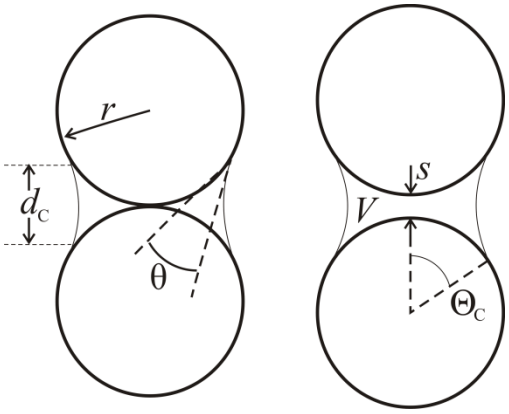

Fig. 2: Pendular, liquid bridge between two adjacent particles. Left: Particles directly in contact. Right: particles are separated by distance s.[26,27]

A pendular shaped liquid bridge exerts a capillary force F_c between two adjacent particles of same radius r which is given by

$$F_c = \pi\gamma \frac{\cos\theta}{\cos\Theta_C}\left(2r + \frac{d_C}{2}\right) \tag{1}$$

This equation is reduced to

$$F_c = 2\pi r\gamma\cos\theta \tag{2}$$

with the assumptions that the particle separation s is zero and the liquid bridge is smaller than the particle size $r \gg d_C$.[23,26,28] More generally, the force will depend on the volume of the liquid bridge as well as the filling angle and the shape of the droplet.[29,30] Further corrections can be included for particles that are not in contact and for rough particles.[31,32] Generally, the capillary attraction is significantly higher and acts over larger distances than the omnipresent van der Waals force.[7]

In capillary suspensions suspended particles connected by pendular bridges can assemble into sample-spanning networks even at low particle volume fractions ϕ, where ϕ is given by

$$\phi = \frac{V_{solid}}{V_{solid} + V_{liquid}} \tag{3}$$

To be able to employ equation (1) and equation (2) for capillary suspensions the surface tension and wetting angle need to be replaced by the interfacial tensions γ_{2l} and the two liquid wetting angle θ_{2l}. Such particulate gels exhibit a yield stress σ_y, which for equally sized particles is given by

$$\sigma_y = f(\phi)g(S,\tilde{s})\frac{\gamma_{2l}\cos\theta_{2l}}{r} \tag{4}$$

where the number of contacts per particle is captured by the function $f(\phi)$.[27,33] The normalized particle separation $\tilde{s} = \frac{s}{r}$ is considered in the term $g(S,\tilde{s})$ along with the amount of secondary liquid added to the suspension, described by the saturation S.[7,34]

$$S = \frac{V_{\text{better wetting fluid}}}{V_{\text{total fluid}}} \tag{5}$$

In the following the amount of secondary liquid will be either specified by the parameter S or is, alternatively, referred to as secondary liquid volume fraction (vol%). Figure 3a shows each an example for the yield stress σ_y development as function of the saturation S for a capillary state network (polyvinyl chloride PVC particles in water with different amounts of diisononyl phthalate DINP) and a pendular state network (hematite particles in DINP with varying amounts of water).[10] For the PVC particles, figure 3a shows a steep increase of the yield stress for $S \to 1$, placing this system in the capillary state, whereas hematite particles in DINP with added water form a pendular state network and show a maximum in the yield stress for $S \to 0$. Both systems show an increase of yield stress for at least one decade, when adding small amounts of secondary liquid and give a good example for the strong influence of the capillary force on the strength of the sample-spanning network. Figure 3b is a 3D reconstruction of the capillary network for three different droplet contact angles.[35] For this purpose index matched particle-liquid-liquid systems with a defined solid and secondary liquid volume fraction were investigated using an inverted confocal laser scanning microscope. From top to bottom the images show the networks for contact angles θ of 40° (top), 61° (center) and 94° (bottom). For a contact angle $\theta = 61°$ the secondary liquid (shown in yellow) forms toroidal shaped bridges at the contact point between the particles and the entire secondary liquid contributes to the network formation. For the smaller contact angle $\theta = 40°$ the image shows toroidal shaped bridges as expected for a pendular state system, but also clusters of particles surrounding a larger droplet of secondary liquid which is comparable to the funicular state in wet granular materials.[36] In case of the capillary state network with $\theta > 90°$ particles are partially covered with single droplets of secondary liquid that

do not contribute to the network. Other secondary liquid droplets are located between particle clusters consisting of three or more particles. These clusters are the building blocks of the sample-spanning, percolating network. In this case the yield stress is not given by equation 4, but is controlled by the cohesive strength of the clusters. This strength is also determined by capillary forces and depends on the shape of the encapsulated fluid volume and the number of particles included in the cluster. Despite of the differences in type of network, figure 3b shows percolating particle-droplet networks for all depicted contact angles.

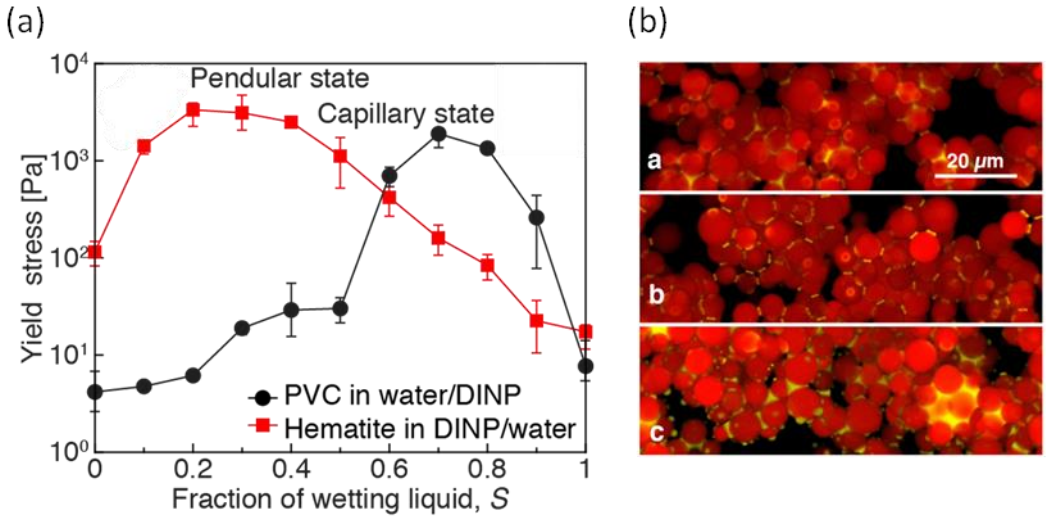

Fig. 3: (a) Yield stress as function of saturation *S* shown for a capillary state network: polyvinyl chloride (PVC) particles in water with diisononyl phtalate (DINP) as secondary liquid. And for a pendular state network: hematite particles suspended in DINP with water as secondary liquid.[10] (b) 3D network of capillary suspensions with varying three phase contact angles: 40°(a), 61°(b) and 94°(c).[35] The secondary liquid is highlighted yellow. The secondary liquid fraction during sample preparation was equal for each image.

Moreover, computational models, such as the computational code Surface Evolver, designed by Brakke,[37] where used to investigate possible network formations for capillary state systems in more detail.[8] They revealed that these particle-droplet-networks show various possibilities for the configuration of close-packed clusters depending on the saturation, in order to minimize the energy of the fluid surface.[8] Figure 4 shows the state diagram with the minimum energy regions for different particle clusters as function of the contact angle and the normalized secondary fluid volume. For contact angles $\theta \to 90°$ and increasing secondary fluid amount the particle clusters change from tetrahedral to polytetrahedal. At higher contact angles ($\theta \sim 140°$) these tetrahedral configurations rearrange to form octahedral particle clusters. Particle structures were investigated for a maximum particle number of $n = 7$. Further information about simulations and calculations referring to cluster formation and gelation and can be found in literature.[38,39]

Reported technical applications of capillary suspensions cover a broad range of materials and products including novel food products, such as heat stable or low calorie chocolate spreads,[40] or capillary

suspension based foams as well as precursor for highly porous ceramic and glass membranes,[41,42] or as pastes for printed electronics like e.g. slot-die-coated lithium-ion battery electrodes.[12]

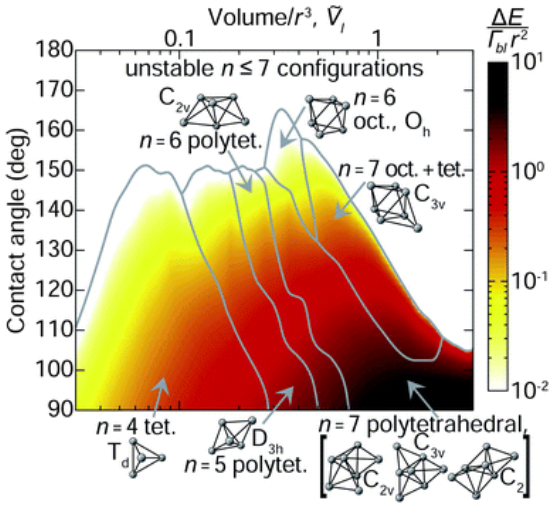

Fig. 4: Minimum energy regions for various particle clusters as a function of the normalized secondary fluid droplet volume $\tilde{V}_l$ and the wetting angle θ.[8]

2.2 Printable Electronics

Besides of the mentioned slot-die coating technique, there is a wide range of printing and coating methods. Table 1 shows a selected number of printing techniques applied in the printable electronics industries and their corresponding characteristics regarding e.g. resolution or printing speed.

Table 1. Characteristics of selected printing processes applied for printable electronics and corresponding ink requirements.[43]

Printing method	**Flexography**	**Offset lithography**	**Gravure printing**	**Screen printing**	**Inkjet printing**
Printing form	Relief (polymer plate)	Flat (Al plate)	Engraved cylinder	Stencil and mesh	Digital
Typical resolution (lines/cm)	60	100-200	100	50	60-250
Ink viscosity (Pas)	0.05-0.5	30-100	0.01-0.2	0.1-50	0.002-0.1
Substrates	Paper, boards, polymers	Paper, boards, polymers	Coated paper and boards, polymers	All	All, 3-D possible
Film thickness (µm)	0.5-2	0.5-2	0.5-2	5-25	0.1-3
Line width (µm)	20-50	10-15	10-50	50-150	1-20
Throughput (m^2/sec)	10	20	10	<10	0.01-0.1
Printing speed (m/min)	100-500	200-800	100-1000	10-15	15-500

2.2.1 Aims in Photovoltaics

In photovoltaic industries, silver pastes for the front side metallization on silicon solar cells are most commonly applied by screen printing with the aim to print narrow contact lines (≈30 µm)[44] with increased aspect ratio (height to width ratio) in order to increase efficiency of the solar cell by reducing grid shading loss.[45,46] Figure 5 shows a scheme of such a silicon solar cell. When exposed to sunlight the electron-hole-pairs are separated by the electric field of the space charge region located between the n- and p-doped silicon, and electrons are discharged at the front contacts.[47] Shape and area coverage of these front contacts play a striking role for the efficiency of the solar cell.

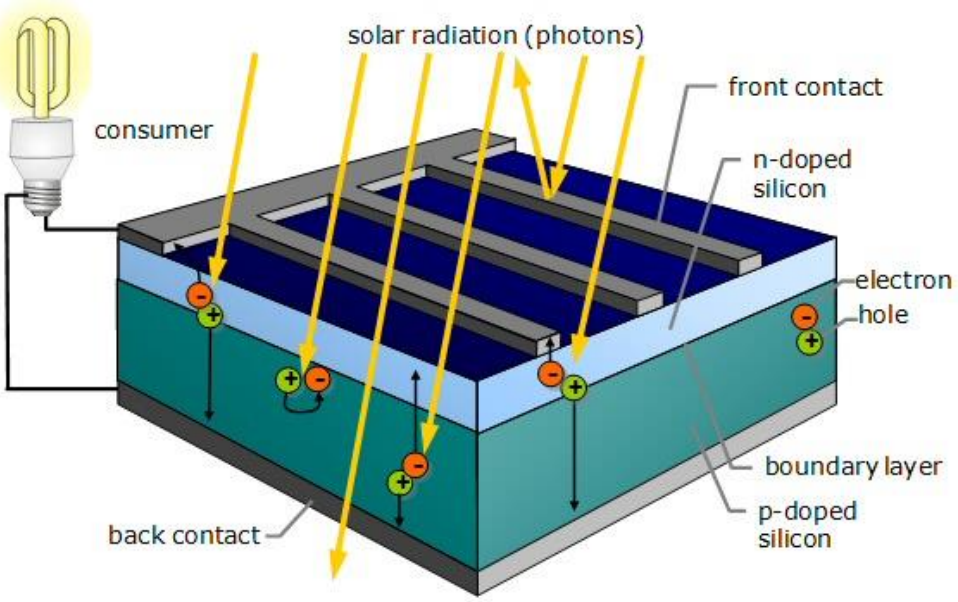

Fig. 5: Scheme of a silicon solar cell with a p- and n-type layer. The electric circuit is closed by the back and front contacts on the cell.[48]

The rate of grid shading loss can be quantified by the ratio of the area covered by the contacts and the total surface area.[49] As silver is an expensive raw material, but required to achieve a desired conductivity, strong efforts are made to improve paste formulation as well as printing technology aiming at uniform lines with optimized cross-sectional shape thus minimizing silver consumption. Figure 6 shows possible cross-sectional profiles for the printed front side metallization on silicon solar cells and the interaction with the incident sunlight. Some of the incident light is reflected by the metal contacts and will not be able to contribute to the current generation. A fraction of the reflected light is reflected again at the glass/air interface and redirected to the silicon surface. Comparing the semi-circle shape of left finger with the flat, right finger in figure 6, it is obvious that for equivalent cross sectional areas an increased height to width ratio (to some extent) is beneficial to decrease grid shading.

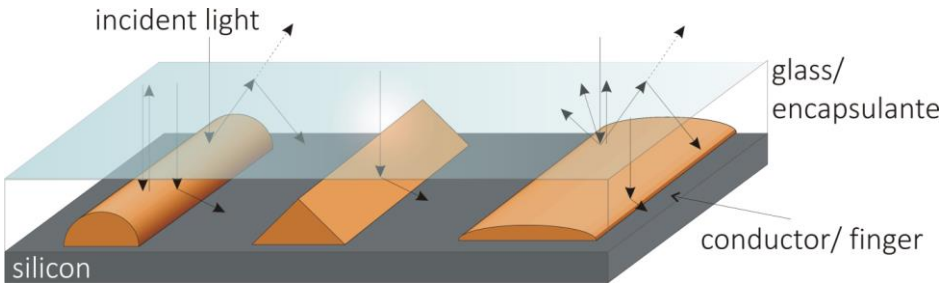

Fig. 6: Incident light hits the silicone surface by direct reflection from the metallization and by indirect reflection from the glass/air interface. From left to right: Profile of a typically plated contact, an advanced plated contact[50] and a screen printed contact.[47]

At the same time the fraction of the light, which does not contribute to power generation due to the reflection on the metal fingers, is also decreased when the geometry changes from rather plane (figure 6, right finger) to a higher and narrower cross section as can be seen for the left, semicircle shaped finger with an increased aspect ratio $AR = \frac{height_{contact}}{width_{contact}}$. The triangular finger in the center is an example for an advanced plated contact. Incident light is redirected to the silicon surface only, without any loss of contribution to power generation.[47]

Reducing the finger width solely is not sufficient to increase cell efficiency. Furthermore, an appropriate cross sectional area is required to maintain a good conductivity.[46] Attempts to achieve this optimized shape for front contacts include of course the improvement of paste rheology resp. the formulation,[51] but also innovative methods for application are suggested, such as multiple line deposition (e.g. double screen printing).[44]

2.2.2 Screen printing and Rheology

In general this method is favored for applying the front side metallization on silicon solar cells because of the high throughput when printing fairly simple designs. A schematic of screen printing is shown in figure 7a. In general, ink is squeezed through a mesh (metal mesh or synthetic fiber) which has been pretreated with an emulsion and UV curing, in order to make the mesh permeable only for the desired pattern.[3] Firstly, the mesh is covered with the ink. As next step the ink is pushed through the mesh openings by a squeegee, which simultaneously presses the mesh against the substrate. After the squeegee has passed the mesh snaps off from the substrate and the coated layer of ink levels and closes the gaps in the pattern, which occur due to the screen mesh. In each of the described steps of the screen printing process the printing paste is exposed to different shear rates, which can be taken from figure 7b.

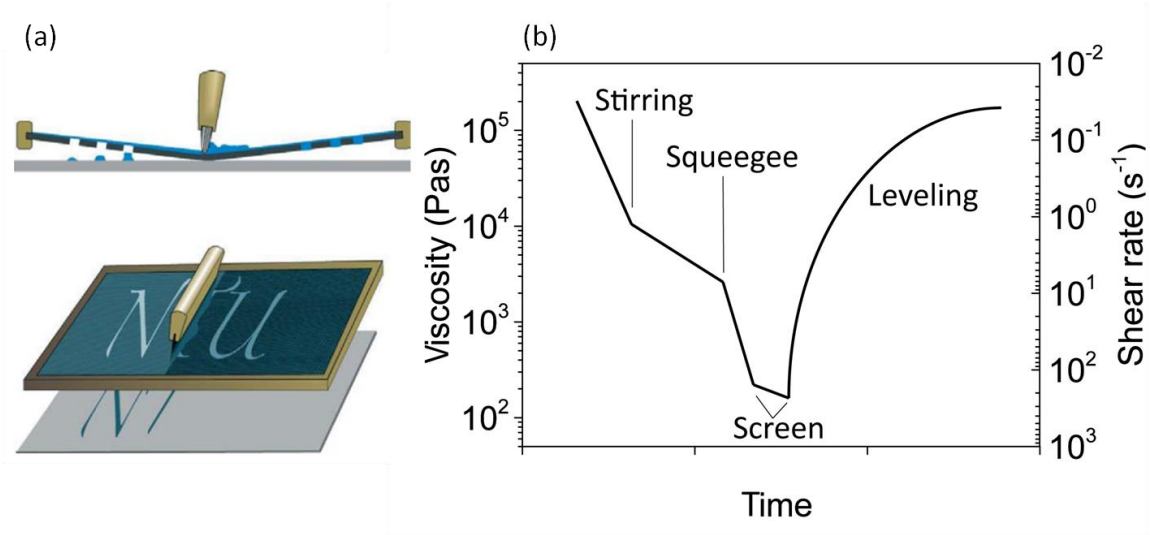

Fig. 7: a) Schematic of screen printing: squeegee pushes the ink through a pretreated mesh.[3] **b) Shear rate and viscosity function for a screen printing process as function of time.**[52]

2.2.3 Paste formulation

Ink formulations for printable electronics such as the front side metallization of silicon solar cells typically comprise a huge number of inorganic and organic components. Inorganic materials are the active material (e.g. conducting particles), materials responsible for the contact formation, oxides or other additives. Solvents, binders and dispersants, which are responsible for the printability, the image and the stability of the ink are usually organic components and summarized as so-called organic vehicle.[53]

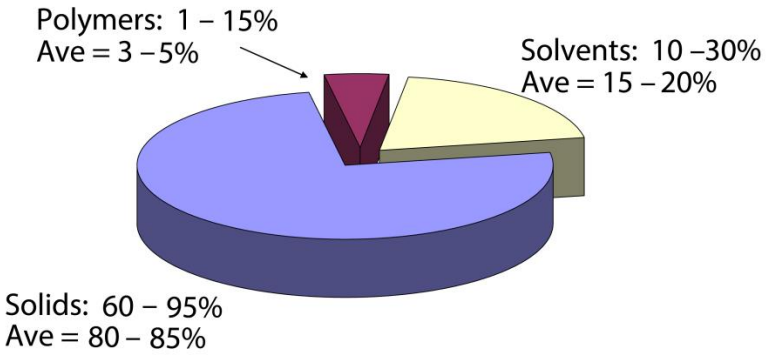

Fig. 8: Overview of weight fractions of polymers, solvents and solids in a thick film printing paste (average is abbreviated with Ave in the image).[46]

The organic vehicle includes also several rheological additives. Ethyl cellulose of various molecular weights and grades is added for example as thixotropic agent, but also acts as a binder. Other examples for binders are polyvinylpyrrolidone (PVP), poly (methyl methacrylate) (PMMA) or polyvinyl butyral (PVB). Further the organic vehicle can include plasticizers and organic or inorganic

thickening agents, e.g. acrylics resp. fumed silica.[46,54] In general the ink has to meet several requirements during storage and print. At rest, stabilizers are necessary to avoid sedimentation of the inorganic materials, e.g. the conductive particles or oxides. During processing shear-thinning is desired with fast relaxation times after the coating step to avoid spreading of the wet pattern and is achieved by the addition of the polymeric additives. In figure 8 this fraction sums up to 1-15 wt%, whereas the solids comprise the majority of 60-95 wt%. Taking the volume fractions into account, there is a huge deviation from figure 8, because the material density of polymers and typical solvents strongly differ from the inorganic components. Assuming an average density of ~1 g/cm³ for the polymer and solvents (assumption based on material densities of e.g. $\rho_{PVP-Luvitec\,K30} = 1.2$ g/cm³, $\rho_{Terpineol} = 0.93$ g/cm³)[55,56] and for a e.g. silver based paste with $\rho_{inorganics,Ag} = 10.5$ g/cm³, the volume fractions shift to 72.3 vol% solvent and 24.1 vol% polymer, remaining only 3.6 vol% of the active material, here silver.[a] Considering the volume fractions, it is obvious that the presence of additives and finally the residues thereof are a lot more important for the efficiency of a paste formulation, than it is evident from figure 8. As mentioned before in the introduction, small fractions of the organic additives can remain in the product after the firing process and affect the physical properties (e.g. conductivity).

2.3 Drying and Crack formation

Suspensions of hard, underformable particles are often used in many industrial applications. Due to their high shear modulus, suspensions of hard spheres are more prone to exhibit cracking during drying. Possible crack patterns range from isotropic cellular to lamellar ordered crack patterns, with a radial direction of crack growth or spirals also being possible, examples see figure 9.[57,58]

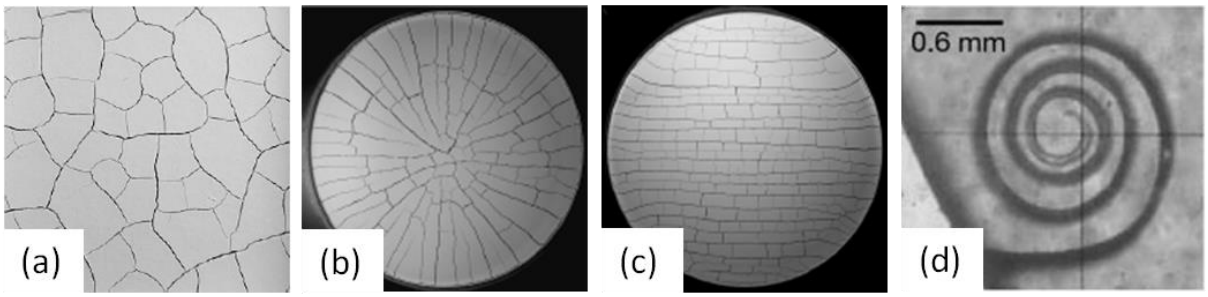

Fig. 9: Crack patterns: (a) isotropic cellular, (b) radial, (c) lamellar and (d) spiral crack growth. [57,58] **Image width of (a) is 150 mm, the discs in (b) and (c) each have a diameter of 500 mm.**

During the drying process of suspensions, evaporation leads to a solvent retention into the particle network. Menisci form between the particles at the liquid-gas-solid interface, inducing capillary forces and a capillary pressure.

The capillary pressure p_c can be expressed by

[a] Conversion made for a paste composition of 5 wt% polymers, 15 wt% solvent and 80 wt% solids loading.

$$p_c = \frac{2\gamma \cos\theta}{r_p} \tag{6}$$

assuming a cylindrical pore with radius r_p is wetted by a solvent with wetting angle θ and surface tension γ.[59] Hence, a decreasing pore size results in a higher capillary pressure, which acts on the particles and pulls them together. In real systems, pore sizes vary and broad distributions lead to a more pronounced inhomogeneity in the resulting drying stress [60–63].

The critical stress σ_{crit}, necessary to nucleate a crack during drying of a suspension of identical elastic spheres with radius r scales as a function of particle shear modulus G, surface tension γ and film thickness h_{max}.[64]

$$\frac{\sigma_{\text{crit}} r}{2\gamma} = 0.1877 \left[\frac{2r}{\mathrm{h_{max}}}\right]^{2/3} \left[\frac{GM\phi_{\text{rcp}} r}{2\gamma}\right]^{1/3} \tag{7}$$

ϕ_{rcp} is the solid fraction at random close packing and M the coordination number. For hard spheres, however, σ_{crit} and the calculation of the maximum crack-free sheet thickness h_{max}, given by

$$h_{\text{max}} = 0.64 \left[\frac{GM\phi_{\text{rcp}} \mathrm{r^3}}{2\gamma}\right]^{1/2} \left[\frac{2\gamma}{(-p_{\text{max}})r}\right]^{3/2} \tag{8}$$

is additionally a function of the maximum capillary pressure $p_{\text{max}} = -3\gamma \cos\theta\, \phi_{\text{rcp}}/[r(1-\phi_{\text{rcp}})]$.[65] Besides particle size or shear modulus, inter-particle forces, thermodynamic properties like temperature, humidity or gas flow rate also affect the shape and appearance of cracks.[66] Rheological properties, such as the yield stress of the suspension, and vibrational preconditioning of the paste have also been shown to correlate with crack development.[57] For biological and biomimetic materials, a spatial variation of the elastic moduli on the microscopic scale has shown to affect and hinder crack propagation.[67]

The thermodynamics of drying capillary suspensions is very complex. Mass transfer is influenced by numerous parameters such as the diffusivity of the secondary liquid in the bulk fluid, the low solubility of the secondary liquid in the bulk phase, the Laplace pressure in the liquid bridges or the equilibrium partial pressure of both liquid components in the ambient gas phase according to Henry's law for the secondary liquid and Raoult's law for the bulk phase.[68] The drying process of binary liquid mixtures in porous media has been investigated before, but research is essentially limited to miscible liquid combinations.[69,70] This complexity can be used to tune the drying process allowing the structure and drying rate to be controlled. Examples, of how the capillary suspension enables to control the drying behavior and appearance of the dry film will be demonstrated in the following.

3 Materials and Methods

3.1 Sample preparation

Table 2 gives an overview of the particles, which were used in this study to create the capillary suspensions. The solvents used as bulk or secondary liquid are listed in table 3 (nonpolar) and 4 (polar) together with their viscosity η at 20°C.

Table 2: Particles used for the capillary suspension formulations.

Component name	Particle size	Supplier
TiO_2 *Aeroxid P25*	$x_{50,3}$=2.45 µm	Evonik (Essen, Germany)
ZnO *VP ADnano ZnO 20*	0.18 µm[b]	Evonik (Essen, Germany)
Al_2O_3 *CT3000SG*	$x_{50,3}$=0.67 µm	Almatis (Ludwigshafen, Germany)
Nickel spheres *Nickel powder 3-7µm*	$x_{50,3}$=9.6 µm	Alfa Aesar (Karlsruhe, Germany)
Nickel powder, < 1µm	$x_{50,3}$<1 µm[b]	Sigma Aldrich (Steinheim, Germany)
Nickel Flakes *Conductive Nickel Flake HCA-1*	$x_{50,3}$=11 µm	Novamet (Lebanon, TN, USA)
Silver particles *Silverpulver GE C50*	5-15 µm[b]	Doduco (Pforzheim, Germany)
Solder glass *lead-free solder glass 8470*	$x_{50}\leq$12µm, $x_{99}\leq$63µm[b]	SCHOTT AG (Mainz, Germany)

Table 3: Nonpolar solvents used for the capillary suspension formulations.

Component name	Viscosity at 20°C (mPas)	Supplier
Terpineol *mixture of isomers, anhydrous*	67[71]	Sigma Aldrich (Steinheim, Germany)
Paraffin oil *low viscosity paraffin oil*	29-36[72]	Carl Roth (Karlsruhe, Germany)
n-Octanol	9[73]	Merck (Darmstadt, Germany)
Diisononyl phthalate (DINP)	103[74]	Henkel AG (Düsseldorf, Germany)

[b] According to the supplier.

Table 4: Polar solvents used for the capillary suspension formulations.

Component name	Viscosity at 20°C (mPas)	Supplier
N,N-Dimethylformamide (DMF)	1.1[75]	VWR Chemicals (Darmstadt, Germany)
Distilled water	1[76]	

Figure 10 gives an overview of the measured particle size distributions of the used particles nickel spheres and flakes, TiO_2 and ZnO. The particle size of TiO_2 and ZnO was measured using a LALLS (Low Angle Laser Light Scattering, Sympatec HELOS H0309). Particle size distribution of the nickel particles was examined with a Multisizer MSII (Beckman Coulter Inc., CA, USA).

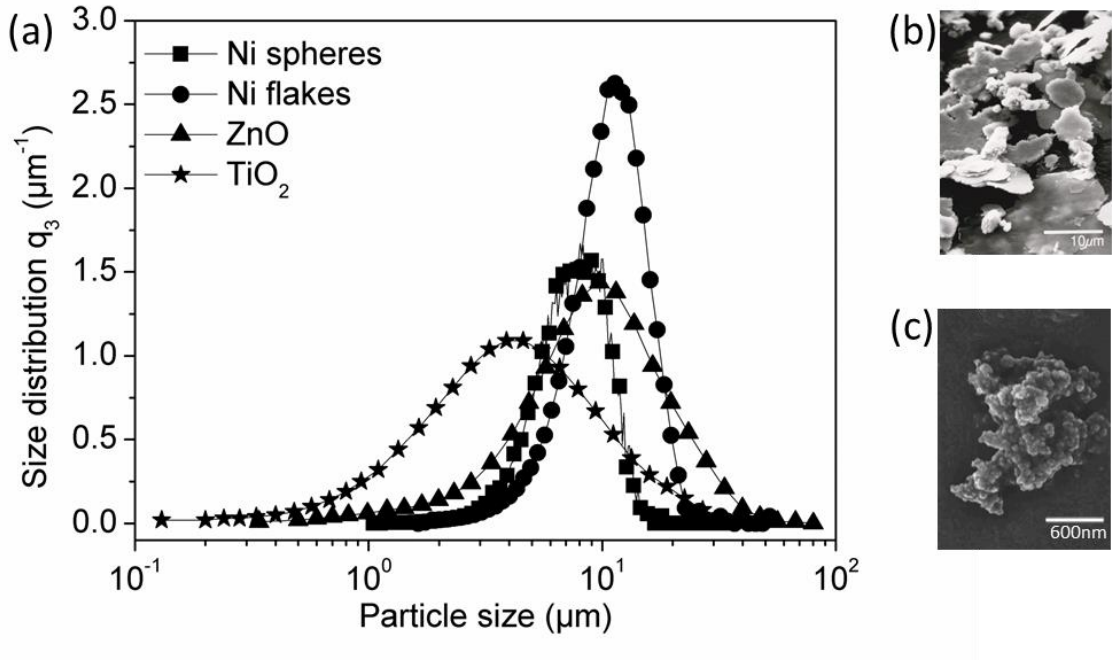

Fig. 10: (a) Particle size distribution q_3 by volume for the used nickel spheres and flakes, ZnO and TiO_2. Irregular shapes of the (b) nickel flakes and (c) TiO_2 particles.

In general, the nickel spheres have a broader size distribution with an $x_{50,3}$=7.4 µm, whereas the size distribution of the flakes with $x_{50,3}$=9.6 µm show a sharp peak at 11 µm. For the latter, it must be taken into account that, due to the measurement set-up of a coulter counter, the measured particle size of flakes strongly depends on the orientation of the irregular shaped particle. According to the supplier aspect ratio of the flakes is ~20:1.[77] The particle size of TiO_2 and of the ZnO particles are shifted to higher particle sizes compared to the information provided by the supplier with $x_{50,3}$=2.45 µm resp. $x_{50,3}$=9.3 µm. According to the supplier primary particle size of the TiO_2 particles synthesized by pyrolysis is 25 nm. The ZnO particles are listed with a particle size of $x_{50,3}$<0.18 µm. Table 5 gives an overview of selected physical properties of the solid materials used in this study.

Table 5: Physical properties of the solid materials.

	Density ρ (g/cm³) T=20°C	**Melting point t_m (°C)**	**Bulk resistance R_{bulk} (Ωm) T=0°C**
TiO_2	3.8	1850	
ZnO	5.61	1975	
Ag	10.49	960.5	1.51×10^{-8} [78]
Ni	8.91	1455	6.84×10^{-8} [78]

3.1.1 TiO_2 and ZnO based capillary suspensions

To create the capillary suspensions, TiO_2 particles (Evonik, Aeroxid P25, Essen, Germany, 2.45 µm average aggregate size in n-octanol) and ZnO particles (Evonik, VP ADnano ZnO 20, Essen, Germany, mean aggregate size according to supplier <0.18 µm) were dispersed in n-octanol (Merck, Emplura, Darmstadt, Germany) and distilled water was added as secondary liquid. For the infrared spectroscopy measurements the distilled water was replaced by deuterium oxide D_2O (Carl Roth, Karlsruhe Deutschland), which has a clearly distinguishable absorbance peak. During sample preparation, the particles were slowly added to the bulk fluid while stirring at low speed with a turbulent beater blade (200 rpm), the mixture was then stirred at high speed (30 min, 1000 rpm) to ensure a homogeneous distribution. Finally, the capillary network formation was induced by adding varying amounts of the secondary liquid and maintaining the high stirrer speed for another 5 minutes. The TiO_2 samples containing surfactant were prepared with an aqueous surfactant solution (Evonik, Tego Dispers 752W, Essen, Germany, 10 vol%) as secondary liquid.

3.1.2 Nickel and silver based capillary suspensions

The metal particles were first dispersed into the appropriate nonpolar solvent and then water was added to create the capillary suspension. Details about the particles and solvents can be found in table 2, 3 and 4. The particle quantity, (specified by the desired volume fraction), was added to the bulk phase while slowly stirring with a turbulent beater blade. After adding the solids, the stirrer speed was increased to 1000 rpm for 20 minutes to ensure homogenization. Finally, the capillary network formation was induced by adding the secondary liquid volume with a pipette and stirring at high speed for another 5 minutes. An additional sample using a combination of silver particles and solder glass was prepared as above where the volume of silver particles was supplemented by an additional 6 vol% solder glass. The samples were prepared using distilled water with the exception of capillary suspensions with paraffin oil as bulk phase, which were also prepared using DMF and a DMF/water mixture. DMF acts as reducing agent and also employed here to remove the oxidation layer, which often happens to be on the surface of small metal particles and can affect the conductivity. Pastoriza-Santos suggested following formula for the aqueous reduction of Ag^+ particles with DMF[79]

$$HCON(CH_3)_2 + 2Ag^+ + H_2O \rightarrow 2Ag + (CH_3)_2NCOO + 2H^+$$

where a successful reduction can be detected by an increase of conductivity due to the higher mobility of the H^+ ions. Similar reaction was assumed for the nickel particles and tested by measuring the conductivity of a DMF-water solution (1:1 by weight) with added nickel flakes in a closed beaker. Temperature and conductivity were measured as function of time, see figure 11. Conductivity of the solution increased to the two-fold of the initial value, while the temperature remains fairly constant and allows for excluding thermal causes for the change in conductivity. This also confirms that the increase of conductivity is likely due to the addition of the reducing agent DMF.

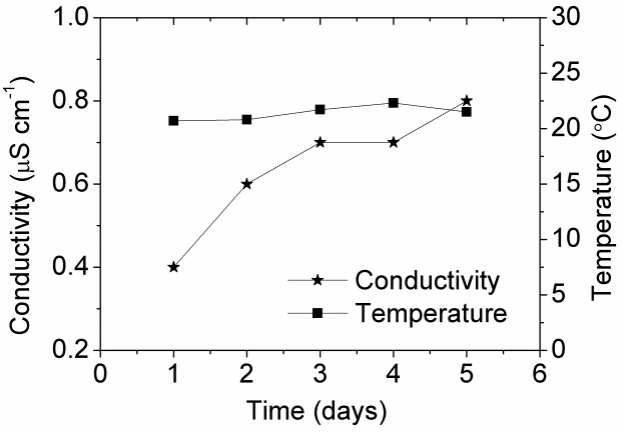

Fig. 11: Conductivity and temperature as function of time for nickel particles in a DMF-water solution.

Nickel capillary suspensions containing nickel flakes were prepared as described above, with the addition of the nickel flakes to the suspension after creating the capillary suspension purely with nickel spheres. Homogenization of the nickel flakes was performed at low stirrer speed (300 rpm) with a propeller stirrer for another 5 minutes.

3.1.3 Preparation of the organic vehicle

Additional silver and nickel samples were used, to compare the rheological and electronic properties of the capillary suspension based products with conventional formulations. The silver samples, obtained from Heraeus Precious Metals (Hanau, Germany), are referred to as Heraeus I (SOL9610A, 90.5 ± 1 wt% solids) and Heraeus II (SOL9020C, 90 ± 1.5 wt% solids). Additionally, two nickel samples were prepared following a patent for an organic vehicle.[80] This organic vehicle contained 60 wt% terpineol as solvent. To this solvent, a polymeric stabilizer (5 wt% polyvinylpyrrolidone K30, average M_w=40,000 g/mol, Sigma-Aldrich, Steinheim, Germany), a dispersing agent (20 wt% TEGO Dispers 656, Evonik, Essen, Germany), a cellulose based binder (10 wt% sodium carboxymethylcellulose CRT 200PA, DOW Europe GmbH, Bomlitz Germany) as well as 5 wt% dispersing and thixotropic agent with either hydrophilic (Aerosil 150, Evonik, Essen, Germany) or hydrophobic properties (Aerosil R805, Evonik, Essen, Germany) were added. The components were homogenized by slowly stirring with a turbulent beater blade (370 rpm) at a constant temperature of

70 °C for two hours. After preparation, the organic vehicle was cooled to room temperature. The nickel particles (Alfa Aesar, Nickel powder 3-7µm, Karlsruhe, Germany) were added to the organic vehicle and the sample was stirred for another 30 minutes at 400 rpm. The nickel particles and volume fraction were the same as in the capillary suspensions ($\phi_{\mathrm{Ni}} = 0.29$).

3.1.4 Synthesis of the silver nanoparticle dispersion

A dispersion of silver nanoparticles was created following the synthesis published by Kim.[81] Silver nitrate $AgNO_3$ (99.9999 trace metal basis, Sigma Aldrich, Steinheim, Germany) was dissolved in a PVP (K30, average M_w=40,000 g/mol, Sigma-Aldrich, Steinheim, Germany) and ethanol (type 642, 99.9% purity, Dr. Wieland GmbH + Co. KG, Marbach am Neckar, Germany) mixture (0.57 wt% PVP in ethanol) in a closed beaker at 70°C. The weight ratio of PVP and $AgNO_3$ was chosen to be 5:1. According to Kim, the size of the formed nanoparticles is dependent on the ratio of polymer and silver salt and a weight ratio of 5:1 is appropriate for the synthesis of 4-8 nm sized particles. The silver nitrate concentration in ethanol was 5×10^{-3} mol/l. After 15 minutes the dispersion color changed to yellow indicating that the synthesis took place. To ensure a high conversion, the total reaction time was 180 minutes. After the synthesis the dispersion was centrifuged (9000 rpm, 9 minutes) and the sediment redispersed in distilled water. Assuming a total conversion of the silver salt, the final silver dispersion contained 1.3 vol% of silver nanoparticles.

3.2 Contact angle measurements

The three phase contact angle θ_{2l} was measured to characterize the solid-liquid-liquid system. A layer of the solid material (e.g. sintered and polished tablet or foil) was placed in a glass container and covered with the fluid of lower material density. A droplet of the second liquid with the higher material density was placed on the solid surface (sessile drop) using a syringe and the resulting static three phase contact angle θ_{2l} evaluated immediately via an image analysis program (Krüss, Drop Shape Analysis, Hamburg, Germany).[82] The contour of the droplet was fitted using the Young-Laplace method, applicable for symmetrical drop shapes not affected by sample tilting or contact with the deposition needle.[83]

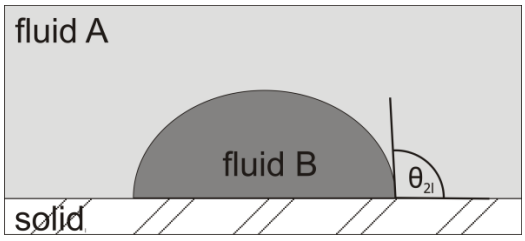

Fig. 12: Sessile drop of fluid B placed on a solid surface surrounded by fluid A with $\rho_A < \rho_B$. The three phase contact angle θ_{2l} is formed between baseline (substrate) and the droplet contour tangent.

Depending on each solid phase used for the capillary suspension formulation, different approaches were made to receive a smooth material surface for the contact angle measurement. In case of the TiO_2 samples the loose powder was densified and sintered. The particles were pressed to a dense tablet under a pressure of 19 MPa and sintered at 1000 °C for five hours in order to achieve a dense packed structure. As final step the sintered tablet was polished to ensure a smooth surface.

For the nickel capillary suspension a nickel film was prepared by thermal annealing at 800 °C. The surface roughness after heat treatment was negligible compared to the size of the droplet that was placed on the surface for the contact angle measurement. The detailed procedure of the thermal treatment can be taken from chapter 5.7.

In case of the silver samples a silver foil of 999/1000 material purity (Dukatshop, silver foil 999/1000 purity, Berlin, Germany) was used to investigate the three phase contact angle.

3.3 Interfacial tension

Further characterization of the solid-liquid-liquid system was done by measuring the interfacial tension γ_{2l} between the bulk and secondary fluid via the pendant drop method. Therefore, a droplet of fluid B which is attached to the tip of a needle is placed in a chamber with fluid A ($\rho_A < \rho_B$). If the image scale is known as well as the density difference between both fluids, it is possible to calculate the surface tension between the two liquids.[83,84]

Bashforth and Adams correlated the interfacial tension γ and drop shape through a nonlinear differential equation

$$\frac{1}{\frac{r_{dr}}{h_{dr}}} + \frac{sin\Theta_{dr}}{\frac{x}{h_{dr}}} = -B \cdot \frac{z}{h_{dr}} + 2 \tag{9}$$

where B is given by

$$B = \frac{{h_{dr}}^2 \cdot g \cdot \Delta\rho}{\gamma} \tag{10}$$

with the gravitational constant g, the interfacial tension γ and the difference in densities $\Delta\rho$. h_{dr} is the radius of curvature at the apex of the droplet, x,z and Θ_{dr} are the coordinates, see figure 13, and r_{dr} describes the radius of curvature at the point with coordinates (x,z).[85,86]

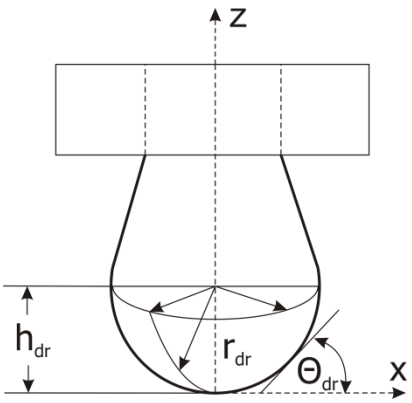

Fig. 13: Geometry of a pendant drop.[86]

3.4 Rheological characterization

After sample preparation a successful network formation due to the capillary bridges was investigated by measuring the viscosity and yield stress. The measurement temperature was 20 °C for all described measurements.

3.4.1 Yield Stress

The apparent yield stress σ_y (for brevity subsequently termed yield stress) of the TiO_2 suspensions was determined with a stress-controlled rotational rheometer (Thermo Scientific, Mars II, Karlsruhe, Germany) and a sandblasted plate/plate (35 mm diameter) geometry. For the metal based capillary suspensions yield stress values were determined using a vane geometry (10 mm vane diameter) placed in a cylindrical cup (Z20 DIN).

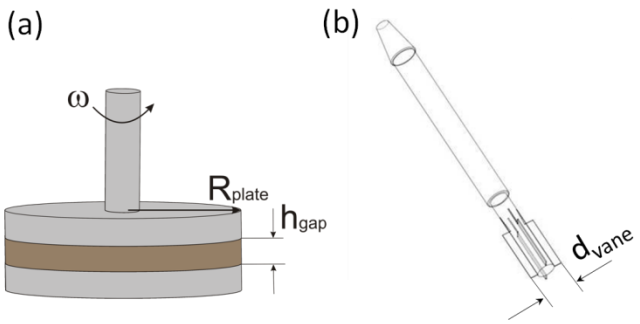

Fig. 14: (a) Plate/plate geometry with radius R_{plate} and gap height h_{gap}. (b) Vane geometry with diameter d_{vane}.[87]

In a plate/plate geometry with radius R_{plate} the sample is filled into the gap with height h_{gap}. Using a stress-controlled device, the applied torque results in a certain angular frequency ω for the top plate, while the bottom plate remains fixed. Taking into account the surface area of the plate, the transmitted stress results in a shear rate $\dot{\gamma}$ (or rate of deformation), which is given by[88]

$$\dot{\gamma} = \frac{d\gamma}{dt} = \frac{\omega \cdot x}{h_{gap}} \text{ with } 0 \leq x \leq R_{plate} \tag{11}$$

By applying successively increasing stress values and measuring the resulting equilibrium deformation, two distinct linear regimes can be found in a double-logarithmic plot, see figure 15. The yield stress is then defined as the intersection of the two linear curve fits representing the onset of irreversible deformation.[89]

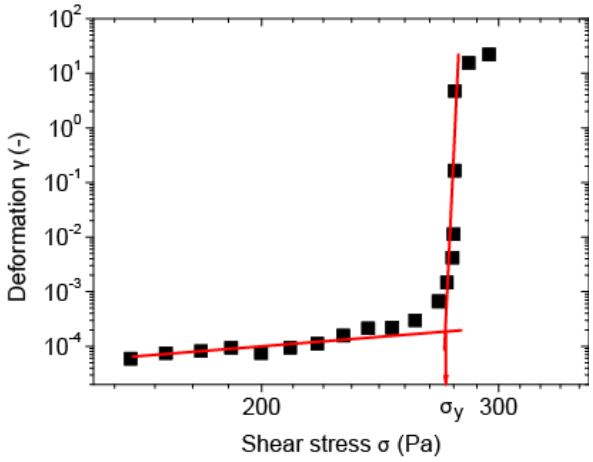

Fig. 15: Deformation as function of shear stress for TiO_2 particles suspended in octanol with *S*=0.05 and the evaluation of the yield stress σ_y via tangent method.

3.4.2 Viscosity

Viscosity in the low-shear regime ($\dot{\gamma} < 100$ s^{-1}) has been determined using the same set-up as for the yield stress measurement and applying stresses above the yield stress using a rotational rheometer and a plate/plate geometry. Viscosity at higher shear rates than 100s^{-1} were measured using a modified Göttfert Rheograph 2000 (Göttfert Werkstoff-Prüfmaschinen GmbH, Buchen Germany) capillary rheometer (capillary length: 40 mm, diameter: 1 mm). The principle of a capillary rheometer is shown in figure 16. Sample is stored in a cylindrical reservoir. A piston, moving with velocity *v*, squeezes the sample through a small capillary and the corresponding pressure right above the capillary is detected with a 200 bar pressure transducer (Gefran, Seligenstadt, Germany). The pressure difference between the capillary inlet and outlet (ambient pressure) is correlated to the wall shear stress inside the capillary, whereas the piston speed is related to the wall shear rate.

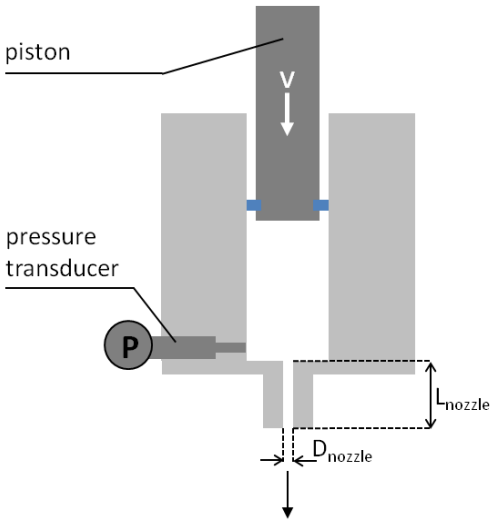

Fig. 16: Schematic of a capillary rheometer. The piston is moved with velocity *v* towards the capillary with length L_{nozzle} and diameter D_{nozzle}. The pressure transducer *P* records the difference in pressure between sample chamber and the ambient pressure.

The shear stress σ_w close to the capillary inside wall as function of the pressure difference Δp is given by[90]

$$\sigma_w = \frac{\Delta p}{L_{nozzle}} \cdot \frac{D_{nozzle}}{4} \tag{12}$$

The flow rate $\dot{V}$

$$\dot{V} = v \left(\frac{D_{sample\ chamber}}{2}\right)^2 \pi \tag{13}$$

and therefore the shear rate $\dot{\gamma}$

$$\dot{\gamma} = \frac{4\,\dot{V}}{\pi\,(\frac{D_{nozzle}}{2})^3} \tag{14}$$

are given by the piston speed *v* and diameter of the sample chamber.

Further measurement corrections, e.g. for wall-slip, were not performed. Therefore, the high shear data should be treated as apparent viscosity values rather than the true viscosity of the sample (for brevity subsequently termed viscosity).

3.4.3 Structural Recovery

The response of the sample after applying a high deformation has been adapted from previous published experiments. Hoornstra et al. chose an oscillatory measurement set-up to simulate a printing process and to evaluate the recovery of elastic properties after a high deformation interval, followed by a sequence with small deformation. [51]

Oscillatory measurements are a possibility to investigate visco-elastic properties of a material. A small stress amplitude is applied to the material with defined frequency and the resulting deformation of the sample is measured. Elastic and viscous properties of the material can then be described by the storage modulus G'

$$G' = \frac{\hat{\sigma}}{\hat{\gamma}} cos\delta \tag{15}$$

and the loss modulus G'', resp.

$$G'' = \frac{\hat{\sigma}}{\hat{\gamma}} sin\delta \tag{16}$$

with storage and loss modulus being a function of the strain-amplitude $\hat{\gamma}$, the applied stress-amplitude $\hat{\sigma}$ and the phase angle shift δ

$$tan\delta = \frac{G''}{G'} \tag{17}$$

between applied stress and resulting deformation. Within the linear-viscoelastic regime (LVE) storage and loss modulus are independent of the applied amplitude (either stress or strain). To determine the LVE regime frequency is kept constant and the amplitude is gradually increased. In suspensions with attractive interactions, e.g. due to capillary bridges or Van-der-Wals attraction, elastic properties dominate and the storage modulus G' dominates over the loss modulus. But after exceeding a critical stress resp. strain amplitude the material response changes to a non-linear behavior, which is mostly attributed to a structural break-down, followed by a cross-over of G' and G'', see figure 17, left image.[88] σ_{crit} describes here the stress, where the value of G' has dropped by 10 % of the initial value and $\sigma_{cross\text{-}over}$ is the corresponding stress at the intersection of G' and G''.

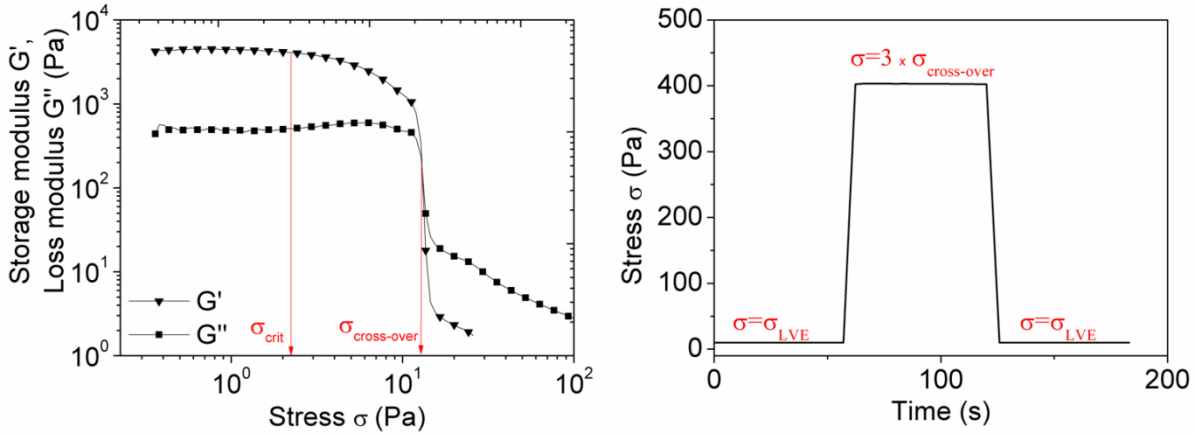

Fig. 17: Left: Storage and loss modulus as function of applied stress in an amplitude sweep measurement. Right: Example of the applied stress as function of time (in a structure recovery measurement). The critical stress values σ_{LVE} and $\sigma_{cross\text{-}over}$ have been determined in the preceding amplitude sweep. Frequency f=1 Hz is kept constant for all three stress periods.

As mentioned at the beginning of this section Hoornstra et al. applied varying oscillatory shear amplitudes to evaluate sample properties as response to high deformation instead of steady shear. Sample is exposed firstly to small amplitude (sample is at "rest"), followed by a large amplitude section simulating the coating process, after which the amplitude changes again to the low initial value to allow for material recovery as it also happens after the paste has been printed on the substrate. Frequency is kept constant. This experiment has been adapted here with minor changes. At first the LVE regime with the corresponding amplitude range is determined via amplitude sweep, which gives the information about the stress values σ_{LVE}, where storage and loss modulus show a linear dependency on the applied stress, and $\sigma_{cross\text{-}over}$. In the subsequent structure recovery measurement fresh sample is exposed to oscillatory shear with the amplitude σ_{LVE} and a frequency of 1 Hz for 300 s. In the second step the amplitude changes to the three-fold of $\sigma_{cross\text{-}over}$ (duration: 600 s). Finally, the amplitude is reduced to the initial value to allow for the structural recovery. Material response in the final interval is measured for 300 s.

3.5 Coating and Printing

Films with a defined area were created via doctor blading in order characterize the electronic properties by measuring the sheet resistance resulting from the different formulations. The doctor blade gap height was 300 µm and accurate shapes of 1 cm² were achieved by confining the pattern with a 60 µm thick adhesive tape, which was removed promptly after film application. The suspensions were coated on heat stable quartz carriers (PELCO Quartz Substrate Discs, Ted Pella Inc., Redding, Calif.).

For printing of fine lines, the adhesive tape was replaced by a glass stencil (171 µm thickness) with a 300 µm line width. After squeezing the sample through the stencil with a blade, the stencil was carefully removed and the height profile examined with the 3D laser microscope.

A further printing technique which was used to evaluate the printing properties of capillary suspensions is a dispenser, which is located at the Fraunhofer Institute for Solar Energy Systems in Freiburg, Germany. Figure 18 shows a schematic of the device.

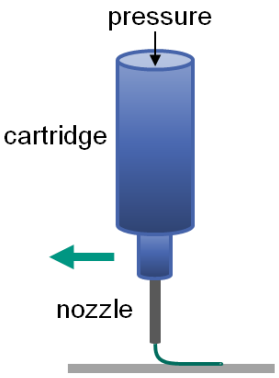

Fig. 18: Schematic of a dispenser. Ink is stored in a reservoir and pushed through a nozzle by applying a defined pressure. The dispenser is moved across the substrate at a certain velocity. Optionally, the substrate is moved while the dispenser remains fixed.

The ink is stored in a cartridge and ejected by applying a defined pressure. For the experiments a cylindrical nozzle made of stainless steel and with a diameter of 124 µm was attached to the cartridge, which was then mounted into a dispensing robot (I&J 7300C, Fisnar Inc., Pine Brook, USA). Operating conditions were 28 bars and line speed of the substrate was 400 mm/s. The resulting fingers were investigated with a 3D laser microscope. Device details and procedure of characterization can be taken from chapter 5.9.

3.6 Heat treatment

The sinter oven used here was designed tailor-made by MUT Advanced Heating Jena GmbH, Germany. The nickel and silver films were both sintered at 800 °C with the fastest available heating rate of 15 K/min in order to imitate the temperature profile of a belt furnace, which is usually utilized in solar cell production. After arriving the maximum temperature, the samples cooled down with purely passive cooling. A 1000 mbar nitrogen atmosphere was employed to sinter the nickel samples in order to avoid any further oxidation during the sintering step. Ambient air was used for the noble metal samples. The sintering atmosphere was partially replaced by 5 vol% of hydrogen to study the influence thereof.

3.7 Sheet Resistance Measurement

The sheet resistance was measured using the Van-der-Pauw method,[91] a four point contact set-up that enables the measurement of the sheet resistance for arbitrary shapes. An electric current is induced between two adjacent contacts and the voltage drop measured between the two remaining, opposite contacts. Following conditions need to be fulfilled when performing the Van-der-Pauw method. The contacts must be placed at the circumference of the sample and need to be sufficiently small. Further, the sample has to exhibit a homogeneous thickness and should not contain any isolated holes.[92]

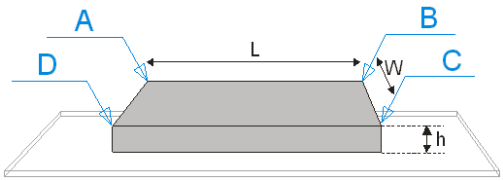

Fig. 19: Set-up for the Van-der-Pauw measurement with four point contacts: A. B, C and D.

For square shaped samples the measured resistance R_{VdP} is given by

$$R_{AB,CD} = \frac{U_{CD}}{I_{AB}} = R_{BC,AD} = \frac{U_{AD}}{I_{BC}} = R_{VdP} \tag{18}$$

and the correlation between sheet resistance R_{sheet} and bulk resistance R for a sample with sheet thickness h is described by the following equation[93]

$$R_{sheet} = \frac{\pi}{ln2} \cdot R_{VdP} = \frac{R}{h} \tag{19}$$

3.8 3D Laser Microscopy

The sheet thicknesses after the sintering process are required for the evaluation of the electric resistance and were measured with a 3D laser microscope (VK-X100 Laser Microscope, Keyence, Neu-Isenburg, Germany).

Lines, which were printed with the dispenser, were characterized at the Institute for Solar Energy Systems in Freiburg, Germany using a high resolution 3D laser microscope (LEXT OLS4000, Olympus Europa SE & Co. KG, Hamburg, Germany). The fingers were characterized by their contact angle α and finger width and height in order to calculate the aspect ratio AR ($AR = \frac{height}{width}$). The contact angle measurement was performed each between the substrate, finger edge and 25 % of the full width towards the finger center.

3.9 Infrared spectroscopy

Infrared (IR) spectroscopy (Bruker, Tensor FT-IR 27) was performed using a diamond attenuated total reflection (ATR) crystal in order to determine the chemical composition of the capillary suspension film during drying. This method is a non-invasive, versatile tool to investigate the IR spectra of materials that are not appropriate (e.g. too thick or strongly absorbing) for transmission spectroscopy.[94]

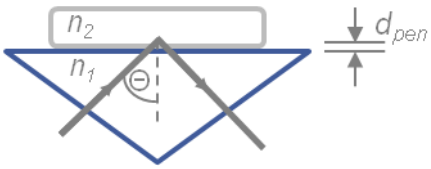

Fig. 20: Interaction of infrared beam at the ATR crystal/sample interface with the specific refractive index n_1 of the internal reflection element and the refractive index of the sample n_2. d_{pen} marks the depth of penetration of the IR beam.

The technique is based on the effect of an evanescent wave and its interaction with an external sample. The IR beam is reflected at the interface with the less dense medium with refractive index n_2 and also extends beyond this interface with the penetration depth d_{pen}. The angle Θ of the incident beam has to exceed a critical value Θ_{crit} to achieve a total internal reflection.

$$\Theta_{crit} = sin^{-1}\frac{n_2}{n_1} \tag{20}$$

n_1 is the refractive index of the internal reflection element and n_2 is the sample`s refractive index. The penetration depth d_{pen} as function of the wavelength λ is given by

$$d_{pen} = \frac{\lambda/n_1}{2\pi\sqrt{(sin^2\Theta - (n_2/n_1)^2)}} \tag{21}$$

The interaction with the sample happens in terms of absorption, where electromagnetic radiation interacts with an electron. Di- and multiatomic molecules with a dipole moment are able to absorb rotational or vibrational energy at characteristic wavelengths.

This effect is used here to trace the existence of the different components of the capillary suspension as function of time in order to investigate the drying behavior. The suspensions were coated onto the ATR crystal with a defined shape of 5×5 mm² using a 100 µm doctor blade and an adhesive tape mask with the desired cut-out area. Before examining the capillary suspensions with TiO_2 particles, the infrared absorbance spectra as function of the wave number $\upsilon = \frac{1}{\lambda}$ of the pure substances where also measured as can be seen in figure 21.

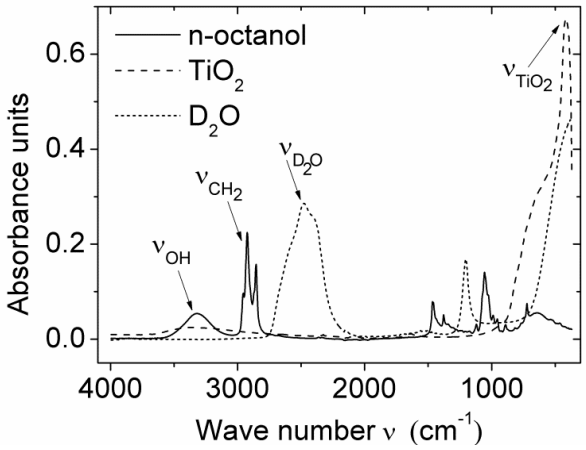

Fig. 21: Infrared absorbance spectra of the pure substances of the capillary suspension annotated with characteristic peaks for tracing the different substances.

4 Results and discussion

4.1 Capillary suspensions with TiO_2 particles - a model system

4.1.1 Influence of the secondary fluid content on the rheological properties

The research results presented here firstly refer to a model system which includes TiO_2 dispersed in n-octanol. Detailed experiments were conducted with TiO_2, before switching the solid phase to less inexpensive materials. As mentioned in the introduction of the capillary suspension phenomenon, a successful network formation can be investigated by measuring different rheological properties of the suspension, such as the yield stress or the visco-elastic properties. Capillary suspensions with TiO_2 particles in n-octanol and water as secondary liquid form a pendular state network with a three-phase contact angle of 79°. Figure 22 shows the absolute values (a) and the normalized yield stress (b) for TiO_2 suspensions with two different volume fractions ($\phi = 0.04$ and 0.05) and with varying amounts of secondary liquid. The yield stress has been normalized by the yield stress value of the pure suspension without added secondary liquid, which is $\sigma_{y,S=0.00} = 12.6$ Pa for $\phi = 0.04$ and $\sigma_{y,S=0.00} = 27.3$ Pa for $\phi = 0.05$. Capillary suspensions could not be obtained for lower volume fractions or higher than ϕ=0.07, where attractive forces among the particles lead to a high yield stress and viscosity without any addition of secondary liquid, which hinders a good sample preparation and a sufficient secondary liquid homogenization. Considering the normalized values, the addition of varying fractions of water leads to an increase of the yield stress by ~1 decade with similar slope for both particle volume fractions, see figure 22b. For the sample with 5 vol% solid loading the yield stress plateaus for $S \geq 0.05$, for the lower volume fraction the maximum yield stress is given for a saturation of $S = 0.05$ and decreases slightly for $S > 0.05$, which is due to the smaller number of particles available for the network formation.

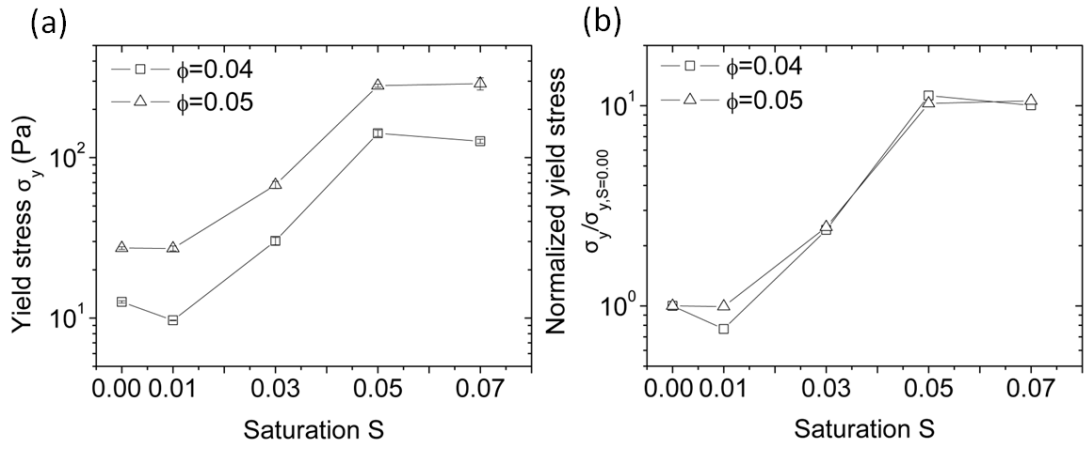

Fig. 22: a) Yield stress as function of the saturation *S* for TiO_2 dispersed in n-octanol ($\phi = 0.04$ and $\phi = 0.05$) and different water fractions varying from S=0.00-0.07. b) Corresponding normalized yield stress values for S=0.00-0.07.

Network formation and network strength can also be quantified using the storage and loss modulus, which characterize the linear visco-elastic properties of the suspension. Figure 23a shows the storage G' and loss modulus G'' as function of the stress amplitude measured at a frequency of 1 Hz for a TiO_2 suspension with $\phi = 0.04$. For the suspension without secondary liquid the moduli G' and G'' have an initial plateau at 2254 Pa resp. 275 Pa. Storage and loss plateau moduli increase gradually for increasing amounts of water with a maximum again at $S = 0.05$ ($G' = 5227$ Pa and $G'' = 343$ Pa), which is a similar behavior as found in the variation of yield stress σ_y with saturation S. For saturations $S > 0.05$, the plateau moduli decrease again. The cross-over stress amplitudes $\sigma_{cross-over}$ behave likewise, see figure 23b. The lowest $\sigma_{cross-over}$ can be found for S=0.00. This value increases for higher amounts of secondary liquid until a saturation of $S = 0.05$ is reached. A further addition of secondary liquid ($S > 0.05$) does not contribute to the extension of the linear visco-elastic regime anymore. The inset shows the correlation of the yield stress σ_y and the corresponding $\sigma_{cross-over}$, which is linear with a slope of $m = 0.59$. Yield stress function and visco-elastic properties both indicate the strongest network at a saturation of $S = 0.05$.

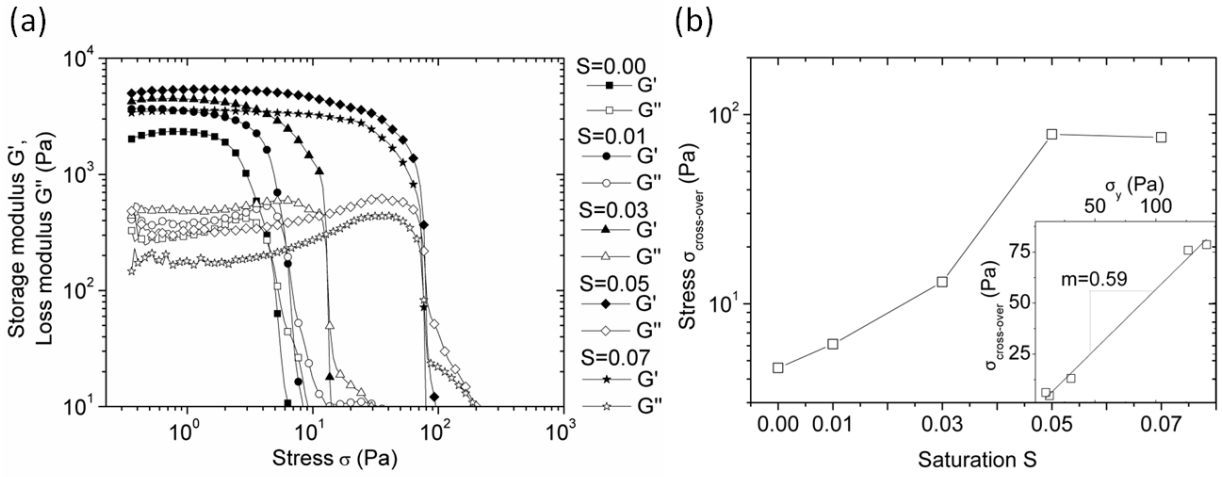

Fig. 23: a) Storage modulus G' and loss modulus G'' for TiO_2 in n-octanol and water as secondary liquid with $S = 0.00 - 0.07$. Measurement frequency f=1Hz. b) Stress at the cross-over of G' and G'' ($\sigma_{cross-over}$) as function of saturation resulting from the oscillatory measurements shown on the right. Inset shows the linear correlation of yield stress σ_y and cross-over stress $\sigma_{cross-over}$.

Also viscosity is affected by the capillary network, as can be seen in figure 24, where viscosity is plotted as function of shear rate $\dot{\gamma}$ for a TiO_2 suspension with n-octanol as bulk phase, water as secondary fluid and a solid volume fraction of $\phi = 0.05$. During the application or coating step, the inks are subjected to high shear rates that vary strongly with the chosen printing technique (e.g. screen printing $\dot{\gamma} \approx 100\ s^{-1}$, dispensing $\dot{\gamma} \approx 10{,}000\ s^{-1}$) followed by a deformation rate close to zero when the ink settles on the substrate.[52,95] Therefore, the inks are required to exhibit low high-shear viscosity that allows the ink to easily flow when passing through the screen mesh or dispensing nozzle during application while also possessing a high low-shear viscosity and a fast network recovery providing

good shape accuracy to the printed structure. Figure 24 shows the rheological response of the capillary suspensions containing TiO_2 particles ($\phi = 0.05$) to different shear rates. Measurements at shear rates below 100 s^{-1} were performed in a rotational rheometer (full symbols) and higher shear rates (up to 10^5 s^{-1}) were achieved using a capillary rheometer (open symbols). The viscosity η is strongly dependent on the amount of secondary liquid in the low shear regime ($\dot{\gamma} < 100$ s^{-1}). In comparison, the viscosity at a shear rate of $\dot{\gamma} = 10$ s^{-1} is the lowest for S=0.00 with $\eta = 4.4$ Pa s. Adding 3 vol% water leads to a small increase of viscosity with $\eta = 5.3$ Pa s and is more pronounced for the suspension with $S = 0.05$, where viscosity rises to the three-fold of the pure suspension ($\eta = 17.0$ Pa s), due to the strong capillary network. In the high shear regime ($\dot{\gamma} > 10^3$ s^{-1}) the viscosity functions coincide and viscosity is solely dependent on the solid volume fraction rather than the stabilization method or colloidal or capillary interactions among particles. This shear rate regime is e.g. relevant for dispensing, where the printing paste is exposed to shear rates of $\dot{\gamma} \sim 10^4$ s^{-1}. Using capillary suspensions flow is not hindered by stabilizing and rheological additives and controlled by the solid loading of the paste, only.

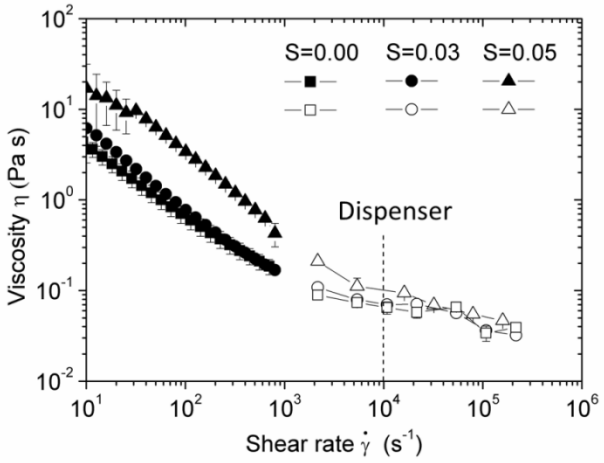

Fig. 24: Low shear (full symbols) and high shear (open symbols) viscosity as function of the shear rate $\dot{\gamma}$ for TiO_2 capillary suspensions in n-octanol and water as secondary liquid with $S = 0.00$, $S = 0.03$ and $S = 0.05$.

4.1.2 Structural recovery of the capillary network after LAOS

For the printing application it is important that the ink shows shear-thinning behavior to easily pass the printer nozzle or screen mesh, while after the coating process a fast recovery of the microstructure is desired in order to avoid spreading of the sample on the substrate. Hoornstra et al. suggested a oscillatory method to measure this material property instead of using a continuous shear method with varying shear rates.[51] Here, the stress amplitudes varied between σ_{LVE} (duration interval 1: 300 s), resembling e.g. storage time of the sample, and $3 \times \sigma_{cross-over}$(duration interval 2: 600s) to imitate a high shear printing process and back again to σ_{LVE} (duration interval 3: 300 s), in order to examine the material response after the printing paste was placed on the substrate. The resulting data for G' and G'' as function of time for three different saturations are shown in figure 25.

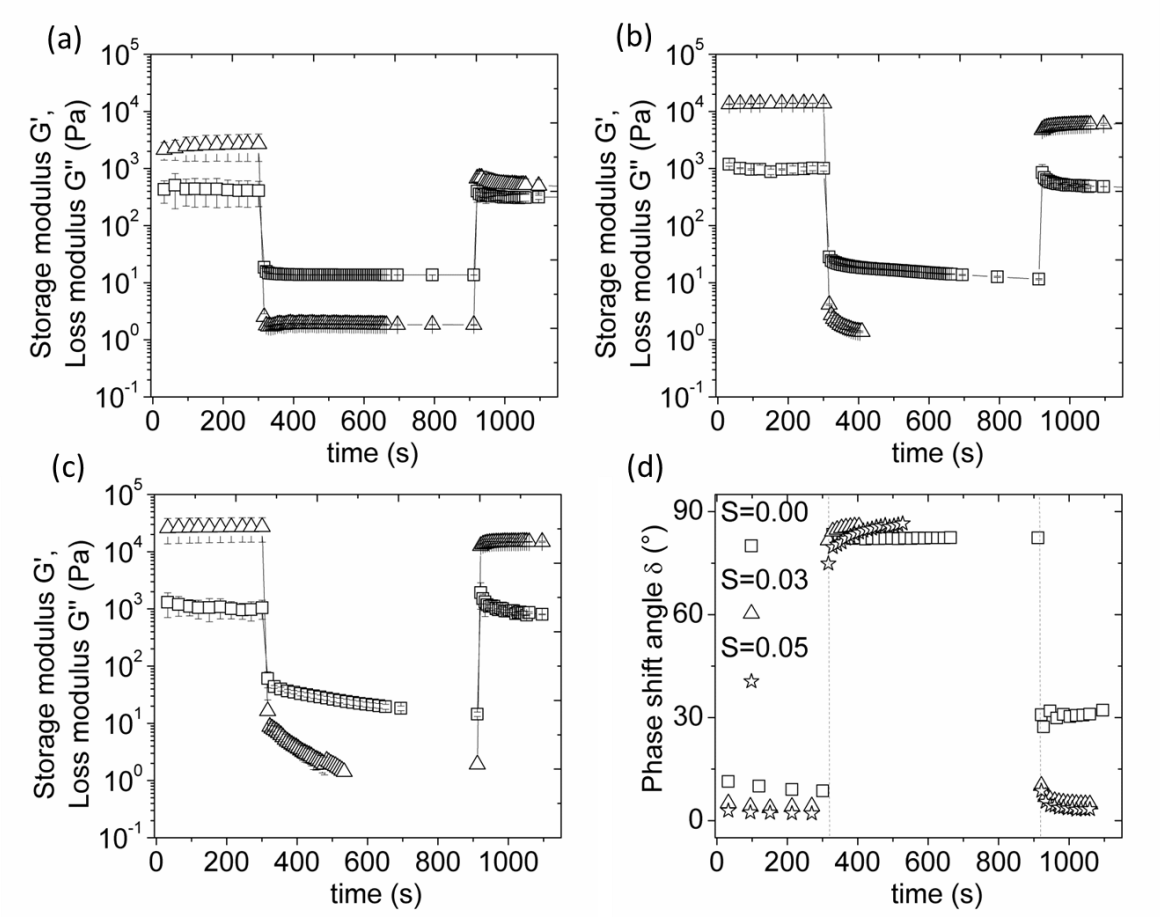

Fig. 25: (a)-(c) Response of TiO_2 capillary suspensions to large amplitude oscillatory shear (LAOS) with $S = 0.00$ (a), $S = 0.03$ (b), $S = 0.05$ (c). Storage modulus G' (symbol: triangles) and loss modulus G'' (symbol: squares) were measured before and after exposing the sample to LAOS. Measurement frequency: 1 Hz. (a) $S = 0.00$, (b) $S = 0.03$, (c) $S = 0.05$. (d) Corresponding phase shift angle δ as function of time.

Figure 25a shows the response of the suspension without secondary liquid. The plateau modulus of G' is approximately one decade higher than the loss modulus. When applying the large amplitude oscillatory shear storage modulus drops by three decades with $G' < G''$ and the moduli remain at a constant value. After the high shear sequence the storage modulus recovers again and is instantly greater than G'', but does not reach the initial plateau value within the period of observation. The final storage modulus reaches only 22 % of the initial value. The addition of the secondary liquid leads to an increase of the initial plateau moduli. Figure 25b shows the response for $S = 0.03$ and 25c describes the response for $S = 0.05$. In the initial rest period with the stress amplitude $\sigma = \sigma_{LVE}$ G' dominates over G'' for both saturations with $S > 0.00$. With the steep increase of the stress amplitude in interval two G' falls below G''. Unlike the pure TiO_2 suspension, the storage moduli of the capillary suspensions do not approach a constant value in interval two but keep falling continuously until they exceed the measurement range. When the stress amplitude is reduced again to the initial value (σ_{LVE}) G' increases instantly to values greater than G'' and maintains a modest increase within the time of observation. The values for the moduli in sequence three are close to the original values at the

beginning of the measurement. For $S = 0.03$ the moduli reaches 41 % of the original value and 60 % is reached for the sample with $S = 0.05$, indicating that the microstructure of the capillary suspension is able to reassemble after the high shear interval. In comparison to previous experiments performed with solar silver pastes by Hoornstra,[51] the capillary suspensions show a remarkably good ability to recover elastic properties within a short time scale (see figure 25). Moreover, the TiO_2 suspension with $S = 0.05$ has an initial storage modulus which is similar to the moduli of commercial pastes investigated by Hoornstra.

The increasing elasticity of the suspension with addition of the secondary liquid can also be seen in figure 25d, where the corresponding phase shift angle δ is plotted as function of time. For $\delta \to 0°$, material approaches ideal elastic behavior, whereas a phase shift angle of $90°$ describes ideal viscous material properties. In interval one the phase shift angle of the suspensions are all close to zero. During interval two the phase shift angles of the capillary suspensions with $S = 0.03$ and $S = 0.05$ slowly approximate $90°$ which can be attributed to a weakening and break down of the network during the large amplitude oscillatory shear which leads to the predominantely viscous behavior. The weaker network due to the Van der Wals forces in the pure TiO_2 suspension is instantly destroyed and δ remains constant during interval two. In the final sequence the capillary suspensions clearly regain elasticity with $\delta \to 0°$ while the phase shift angle of the pure suspension only drops back to a value of ~30°. There is a rapid increase of moduli by about two orders of magnitude within seconds, this initial recovery cannot be resolved with conventional rotational rheometry. The subsequent restructuring kinetics is characterized by the time-evolution of G' and is quantified by fitting G' as function of time following the power law

$$G' = C \times t^b$$

This fit gives the following values for the third interval.

Table 4: Fit parameters for the power law fit

Saturation	*C*	*b*
0.00	739 ±288	-0.11 ±0.02
0.03	4348 ±623	0.06 ±0.02
0.05	11687 ±922	0.07 ±0.02

According to table 4 the pure suspension does not show any increase of the storage modulus within the time of measurement. Whereas the addition of the secondary fluid leads to a increase of the power law index b of comparable order of magnitude for $S = 0.03$ and $S = 0.05$ ($b = 0.06 \pm 0.02$ resp. $0.07 \pm$

0.02), showing that capillary bridges are still being reformed and increase the network strength within the time of observation. Restructuring and aging of capillary suspensions in the capillary state has been investigated by Koos et al. before using hydrophobically modified calcium carbonate suspended in silicone oil ($\phi = 0.11$) with water as secondary liquid.[33] After rejuvenation at a constant shear rate of $\dot{\gamma} = 300$ s^{-1}, storage and loss modulus were monitored either continuously or periodically at a very low amplitude (sample is at "rest") with the first measurement point taken approximately 3 s after rejuvenation, in order to observe the aging and restructuring process. In Koos's experiments both moduli instantly recover to the approximately original value for saturations above a defined value, which is comparable to the material behavior depicted in figure 25. Considering the printing process the strong network due to the capillary bridges within the capillary suspensions, which is able to quickly reform after a high shear interval, is a desired feature in order to prevent spreading of the paste on the substrate and therefore allows for the application for fine line printing.

4.1.3 Printing TiO_2 capillary suspensions

TiO_2 capillary suspensions ($\phi = 0.05$) were printed using a dispenser with a cylindrical nozzle with a diameter of 126 µm and the wet printed lines were examined with a 3D laser microscope. Figure 26 shows the contour of the printed lines for $S = 0.00$, 0.03 and 0.05. Without secondary liquid the suspension spreads across the substrate. Adding 3 vol% of secondary liquid leads to a reduction of the line width, which is even more pronounced with $S = 0.05$.

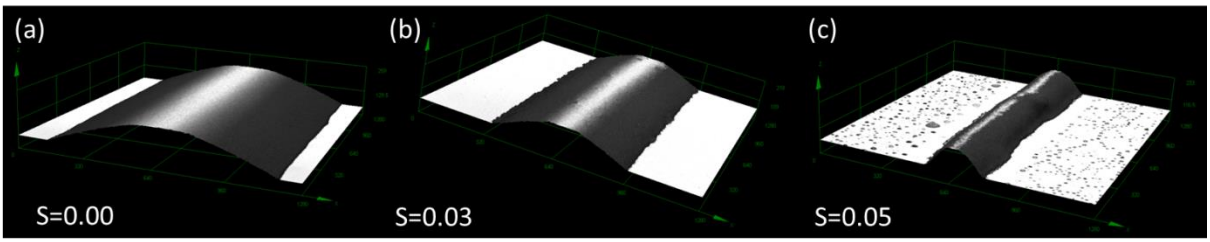

Fig. 26: Wet lines printed with a dispenser using TiO_2 capillary suspensions in n-octanol with added water. Saturation S varies from a) $S = 0.00$, b) 0.03 and c) 0.05.

The evaluation of these images can be taken from figure 27, where line width is plotted as function of the corresponding yield stress of the suspension in figure 27a and the contact angle, formed between substrate and line contour, and aspect ratio as function of saturation in figure 27b. The inset in the left image shows the absolute values of the line width as function of the yield stress. As it is obvious from figure 26, the addition of the secondary liquid to the suspension leads to a strong change of the appearance of the printed line. The line width changes from an average width of 1175 ± 53 µm for a saturation of $S = 0.00$ down to 917 ± 19 µm and 458 ± 52 µm for $S = 0.03$ resp. 0.05, which corresponds to 78% and 39% of the original width achieved with the suspension with no secondary liquid added. The capillary network also leads to an improvement of the printed lines regarding the contact angle α and aspect ratio AR. With $S = 0.03$ the aspect ratio and contact angle remain rather

constant with a small increase in the contact angle. But with $S = 0.05$ the increase of aspect ratio and contact angle is more than two-fold. Keeping the application for the front side metallization in mind, these product properties in general allow for fine line printing and are beneficial to reduce grid shading loss on a solar cell, as the cross sectional profile changes from flat semi-circle to a more triangular shaped profile.

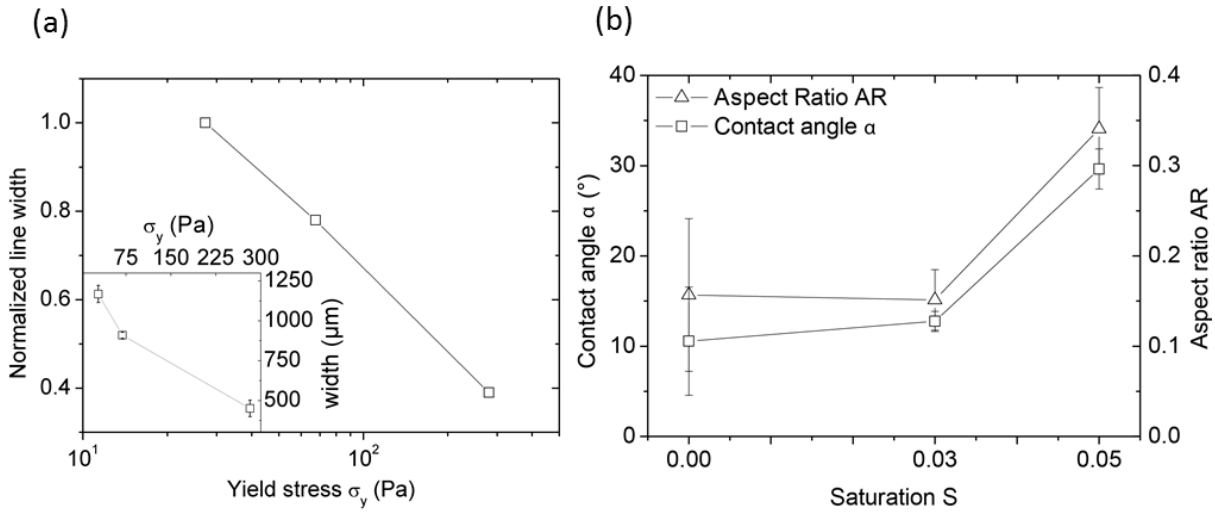

Fig. 27: a) Line width of printed TiO_2 suspensions as function of yield stress for $S = 0.00$, 0.03 and 0.05 (from left to right). b) Corresponding contact angle α and aspect ratio AR without secondary liquid and for $S = 0.03$ and $S = 0.05$.

The aspect ratio with the highest amount of secondary liquid is able to compete and improve upon aspect ratios that were achieved using conventional printing pastes formulations and the screen printing technique.[96] Also novel screen masks as presented by Itoh,[97] which include a special coating of the screen in order to avoid spreading of the printed contacts ($AR \sim 0.19$), are not able to outperform the AR values shown here. Other contacts which have been printed with a dispenser and conventional pastes showed possible aspect ratios of $AR = 0.76$ for semi-circular contact profiles.[95] But it must be kept in mind that also the shape and the associated reflection loss as well as the bulk resistance are crucial for the final efficiency of the solar cell.

4.1.4 Yield stress and crack formation as function of secondary fluid content

Titanium oxide TiO_2 capillary suspensions with n-octanol as bulk phase and water as secondary liquid form a pendular state network with a three phase contact angle of 79°. Thus, the secondary liquid forms pendular bridges between the particles creating a sample-spanning network that avoids sedimentation and further particle aggregation after dispersing. The SEM images in figure 28a show the dry film surfaces of the pure TiO_2 suspension and the capillary suspensions with varying saturation S. The images clearly demonstrate that crack formation during drying is significantly suppressed upon addition of the secondary liquid.

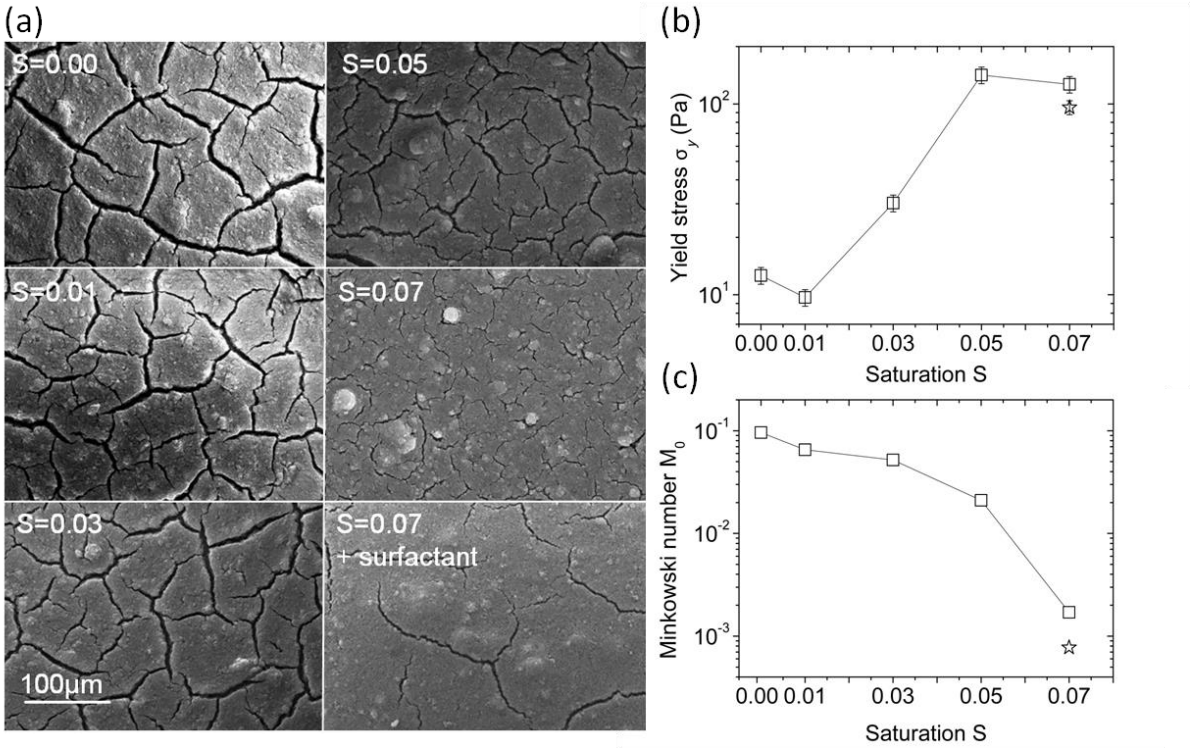

Fig. 28: a) Surface morphology after drying and b) yield stress σ_y prior to drying for TiO_2 particles dispersed in n-octanol with $\phi = 0.04$ and increasing amounts of secondary liquid S. c) Area density M_0 after drying as function of saturation S. The data point at $S = 0.07$ with 10 vol% surfactant Tego Dispers 752W in the secondary liquid is additional shown in the lower right image and as a star in (b) and (c).

A simple quantification of the crack development can be achieved by binarization of the SEM images. The Minkowski number M_0[98] describes the area density of the cracks and the resulting values are shown in figure 28b as a function of saturation, quantitatively characterizing the reduced cracking. For the sample without added secondary liquid ($S = 0.00$), the SEM image reveals a high number and long-range cracks in the dried film. The morphology of the dry particulate films changes when adding increasing amounts of water to the TiO_2 suspension. The visible number of cracks is reduced and the size also changes to narrower and shorter cracks that no longer interconnect to form closed domains. The successful formation of the capillary network is evident from the increasing yield stress as a function of saturation S (figure 28c). Without any added secondary liquid, the suspension yield stress is around 10 Pa and increases by an order of magnitude when adding up to 5% of H_2O. With 7% of secondary liquid in the capillary suspension, the cracks are hardly recognizable and M_0 reaches a minimum – decreasing by two orders of magnitude compared to the sample with $S = 0.00$. However, spherical agglomeration occurs at saturations above the point of maximum network strength (as measured by the yield stress) indicated by the large, round aggregates, which are clearly visible for $S = 0.07$. This phenomenon has also been observed for other capillary suspension systems.[42,99] Here, a small amount of surfactant added to the secondary liquid helps to avoid these aggregates, as shown in

the bottom right image in figure 28a without a significant decrease in the yield stress (star in figure 28c).

The decrease in cracking is not due to variations in the film height, which was kept constant. Calculation of h_{max} according to equation 8 was performed for the pure TiO_2 suspension in order to compare the experimental data with a theoretical approach to the maximum achievable crack-free sheet thickness. Inserting the volume fraction at random close packing $\phi_{rcp} = 0.64$, the coordination number $M = 6$, $\gamma_{\text{octanol}} = 27.3$ mN/m, $G_{TiO_2} = 112.5$ GPa,[100] $\theta = 87°$ and $x_{50,3} = 2.5$ µm in equation 8 results in a maximum crack-free sheet thickness of $h_{max} = 4.12$ cm for the pure TiO_2 suspension. In the experiments presented here the sheet thickness varies between 15.6-17.4 µm, which is more than three decades smaller than the maximum crack-free sheet thickness predicted by equation 8. Therefore, no cracks should be observed here for the pure TiO_2 suspension and this contradicts the findings in this experiment. Referring to the crack formation observed for the pure TiO_2 suspension, it is obvious that the parameters considered in the equation for calculation of h_{max} are not sufficient to estimate the maximum crack-free sheet thickness correctly, especially not for the capillary suspensions. It does not include the contribution of the capillary forces or takes into account the dependency on the ambient conditions and the related drying kinetics, which are decisive for the crack formation, too.

The schematic in figure 29 compares a stabilizer-free suspension with a capillary suspension in the wet film at various times during drying. Initially, both suspensions are completely covered by the bulk solvent. At some later time, $t_1 > 0$, the solvent recedes into the pores and most of the solvent has evaporated at $t_2 \gg t_1$.

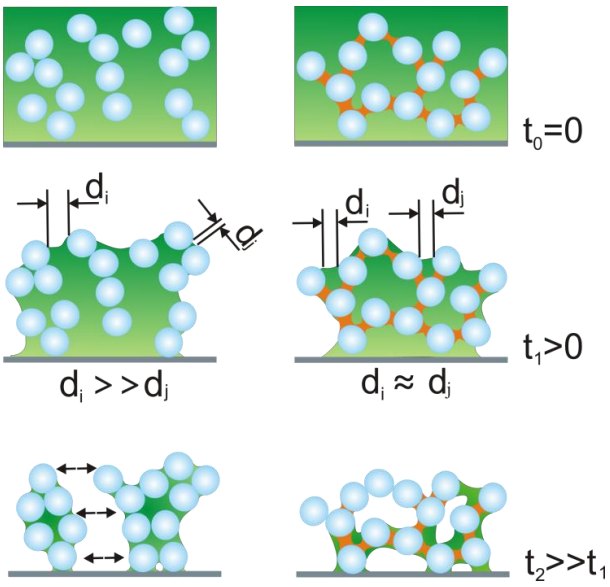

Fig. 29: Particle distribution in a non-stabilized particle suspension (left) and in a capillary suspension (right) at various times during drying.

The non-stabilized particles agglomerate resulting in a broad pore size distribution between particles and the agglomerates. In the case of the capillary suspension, the secondary liquid maintains the homogeneous particle distribution during the initial drying process causing more uniform pore diameters. At a constant bulk solvent contact angle θ and surface tension γ, the capillary pressure p_c in the pores is inversely proportional to the pore radius r_p where smaller pores lead to a higher capillary compression of the surrounding solid while drying.

4.1.5 Crack formation as function of secondary fluid content for ZnO and Al_2O_3 particles

Crack formation was also investigated using ZnO and Al_2O_3 particles and the same solvent combination as for the capillary suspensions with TiO_2 (bulk phase: n-octanol, secondary liquid: water), in order to investigate the universality of this phenomenon. The resulting crack formation occurring in ZnO and Al_2O_3 films after drying as function of the secondary liquid content can be seen in figure 30a and 30c. The corresponding yield stress functions are depicted in figure 30b and 30c, respectively.

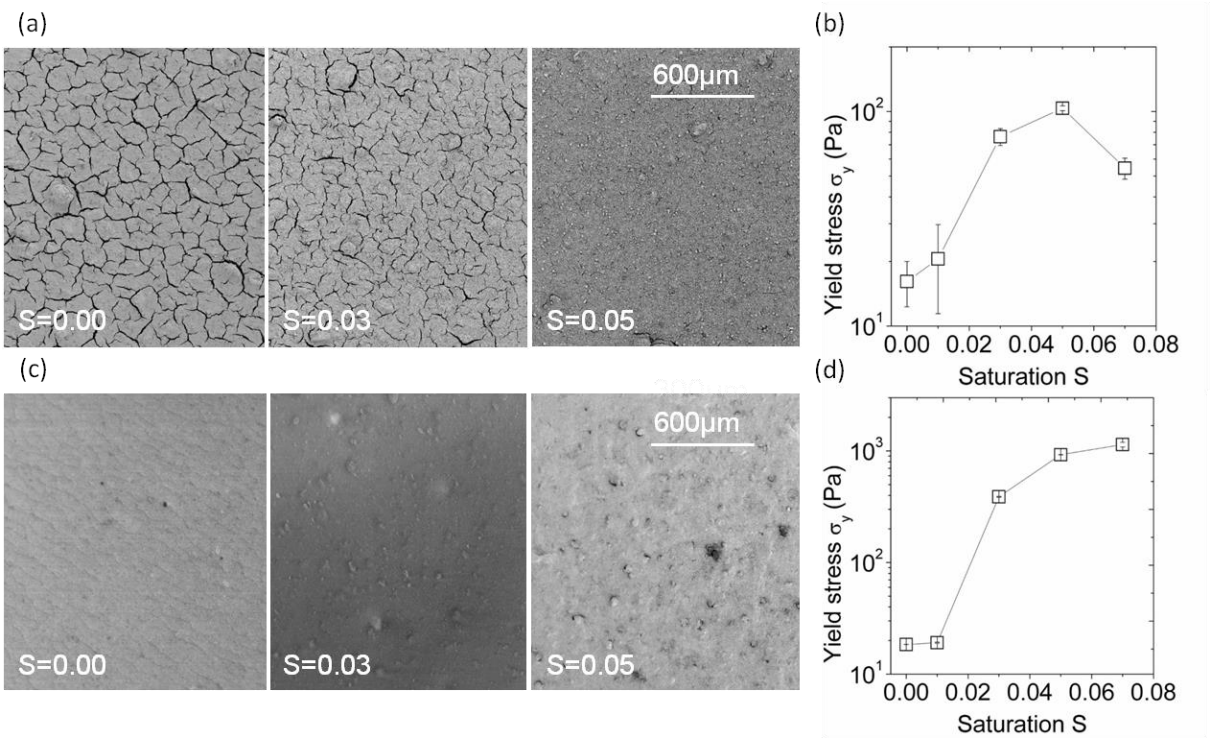

Fig. 30: Dry surface pattern of a) ZnO and c) Al_2O_3 films. Particles were dispersed in n-octanol and stabilized as capillary suspension with H_2O ($\phi_{ZnO} = 0.05$, $\phi_{Al_2O_3} = 0.20$). Yield stress for b) ZnO and d) Al_2O_3 in n-octanol and different fractions of water.

Crack formation of the ZnO films is comparable to the TiO_2 layers, which can be attributed to equal solvent mixture, the metal-oxide characteristics of both solids and the comparable low volume fraction of $\phi_{TiO_2} = 0.04$ and $\phi_{ZnO} = 0.05$. For $S = 0.00$ a high number of deep cracks is visible, which are clearly reduced for $S = 0.03$ and barely visible with $S = 0.05$. After drying the Al_2O_3 suspensions

crack formation is visible for $S = 0.00$ with a regular crack distribution, whereas crack width is not as pronounced as for TiO_2 and ZnO leading to a low contrast in the image. The addition of 3 and 5 vol% of the secondary fluid reduces the cracks, but also leads to the formation of small agglomerates. The differences in crack appearance for $S = 0.00$ between the Al_2O_3 and the ZnO and TiO_2 samples can be assigned to the higher solid loading of the Al_2O_3 suspension with $\phi_{Al_2O_3} = 0.2$. This higher solid loading was chosen in order to investigate the influence of the secondary liquid on the crack formation also for solid volume fractions more applicable in industrial products, such as printing pastes. For similar particle sizes, the distinct higher solid volume fraction of the Al_2O_3 suspensions comes along with a smaller distance between the particles and therefore also reduces the distance a particle can be forced to move due to the drying stress, which results in a smaller crack width. The yield stress functions show the usual characteristics of a capillary suspension where the addition of the secondary liquid leads to a steep increase of the yield stress of approximately one decade with $S = 0.05$ for the ZnO based capillary suspensions and an increase of ~2 decades for the Al_2O_3 suspensions with the maximum not reached within the applied range of saturations.

4.1.6 Drying time as function of secondary fluid content

In order to gain more insight into the change of sample composition while drying, infrared spectroscopy has been employed revealing a distinct change in drying velocity due to the presence of the secondary fluid in the samples. The films were coated onto an attenuated total reflection (ATR) crystal and the resulting absorption intensity of the infrared light as function of the wave number ν and time is depicted in figure 31a-c.

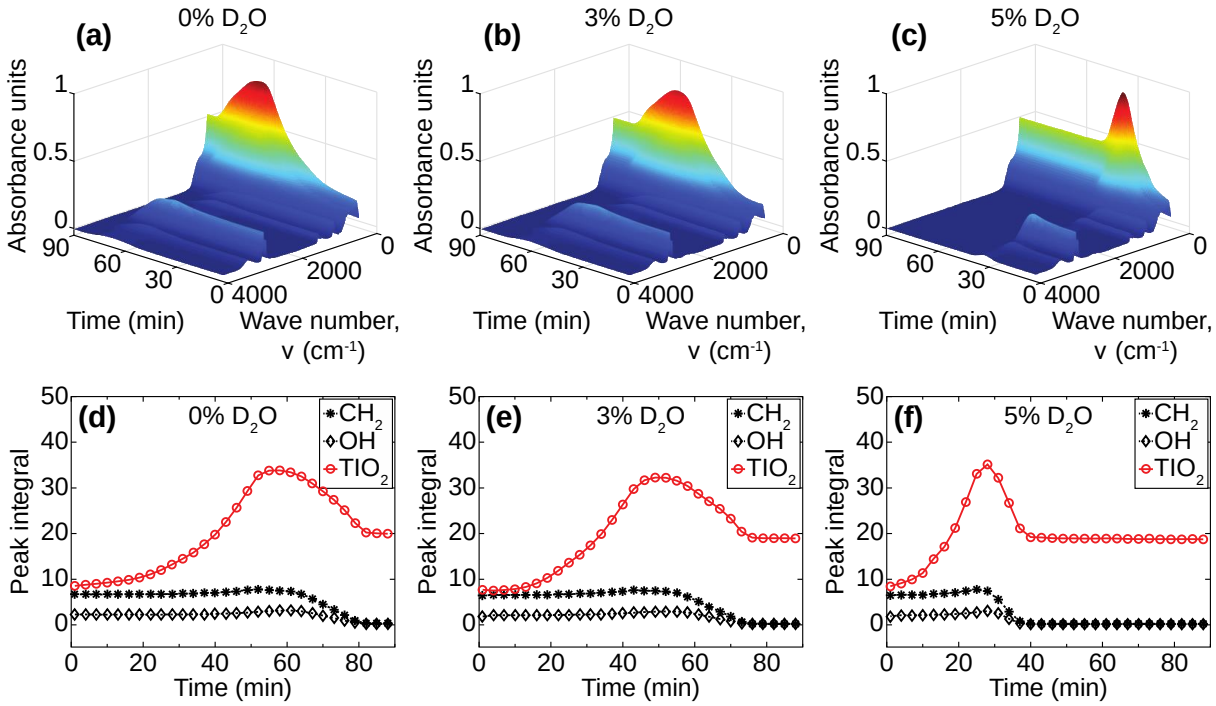

Fig. 31: (a-c) Infrared absorption spectra and (d-f) surface integrals of TiO_2 capillary suspensions with three different D_2O saturations as function of drying time.

The absorbance spectra of the pure substances can be found in Figure 21. The suspensions were prepared with deuterium oxide D_2O as secondary liquid with a clearly distinguishable peak at 2476 cm^{-1} not interfering with the n-octanol absorption peaks, e.g. the methylene stretching resonance frequency $\nu_{CH_2} = 2930$ cm^{-1} and the alcohol specific OH-band at $\nu_{OH} \approx 3330$ cm^{-1}.[94] TiO_2 shows resonance at a frequency of $\nu_{TiO_2} \approx 419$ cm^{-1} presumably corresponding to the Ti-O lattice vibration.[101,102] The area under each characteristic resonance peak was calculated for $\upsilon_i \pm 20$ cm^{-1} and plotted as a function of time in figure 31d-f. Significant differences can be found for the drying kinetics depending on saturation. The time-resolved absorption spectra for the sample with $S = 0$ are shown in figure 31a,d. After 81 minutes, the absorption at the characteristic frequencies ν_{OH} and ν_{CH_2}, indicating the residual solvent, has disappeared. The dry film state is reached and the only remaining peak visible, at a wavelength of 419 cm^{-1}, is attributed to the solid TiO_2. The maximum of the TiO_2 peak intensity at approximately 60 minutes is due to a superposition of contributions from all components in this frequency range and does not correspond to any changes in the Ti-O lattice. The time at which only the TiO_2 peak remains and the intensity of this peak is constant is assumed to correspond to the state where the thin film is completely dry. Adding D_2O to the suspension shows a decrease of the drying time, with 3% D_2O, the dry state is reached after 75 minutes (figure 31b,e) and this is further reduced to 42 minutes for 5% D_2O (Figure 31c,f). To understand how the addition of a secondary fluid reduces the time to evaporate the bulk solvent, we assume that the bulk fluid evaporates first, although n-octanol has a lower vapor pressure at ambient conditions ($p_{v,\,\mathrm{octanol},\ 20°C} = 0.031$ mbar, $p_{v,\,H_2O,\,20°C} = 23.37$ mbar). The interfacial tension (8.52 mN/m)[103] between the two liquids, the low solubility of water in n-octanol (0.3 g/l),[73] and the negative Laplace pressure due to the concave shape of the pendular bridges, prevents the rapid evaporation of the secondary liquid keeping the water trapped in the pendular bridges until the bulk octanol surrounding the bridges is removed. These bridges remain during the initial drying steps holding the particles in their initial position corresponding to a homogeneous inter-particle pore size distribution during the drying process. As the gaps between particles are filled with the solvent with a higher vapor pressure, the total drying time decreases with increasing amount of secondary fluid, as can be seen in the IR absorbance spectra in figure 31.

4.2 Capillary suspensions with metal particles

4.2.1 Rheological properties

The following experiments were conducted with nickel and silver particles. The latter is implemented for example in the paste formulation for printing the front side metallization of silicon solar cells, where a high conductivity is required. Nickel pastes are used in high temperature applications. These conductive pastes must be stable when stored despite the large difference in density between the inorganic particles and bulk solvent. Such storage often occurs at rest or under very low shear rates

(e.g., mild agitation). Therefore, the inks must either have a high viscosity in the low-shear regime, which decreases the sedimentation rate, or better yet, by having a yield stress directly preventing particle mobility. The sample-spanning particle network present in capillary suspensions is able to fulfill these requirements as can be easily seen from the change in texture shown in figure 33a for a nickel in paraffin oil suspension with increasing amounts of added secondary liquid, here a mixture of the reducing agent dimethylformamide (DMF) and water (1:1 by volume). The pure suspension with $\phi = 0.20$ is a weak gel. With increasing amounts of the secondary liquid mixture (3 – 10 vol%), the weak gel changes to a strong and stiff gel with clearly different texture. This textural difference is indicative of a high yield stress where the sample-spanning network is able to hold the weight of the sample and prevent particle sedimentation during, e.g., storage.

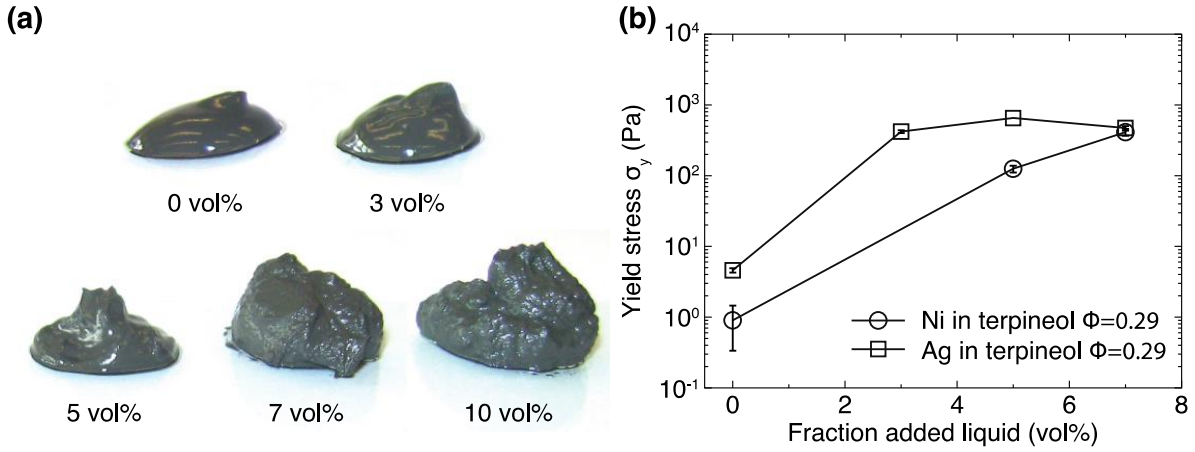

Fig. 32: a) Nickel particles in paraffin oil ($\phi = 0.20$) with increasing amounts of water-DMF-mixture as a secondary liquid. The samples change from a weak gel without added fluid to a strong, stiff gel with added secondary liquid due to the formation of a capillary state network. b) Increase in the yield stress σ_y for nickel and silver particles dispersed in terpineol with increasing amounts of distilled water. Both systems are in the capillary state and have a solid volume fraction of $\phi = 0.29$.

Nickel and silver particles were dispersed in terpineol, a solvent commonly used in printing pastes for front side metallization of solar cells to study the change in flow behavior due to an added secondary liquid systematically. The employed solid volume fraction of $\phi = 0.29$ (≈82 wt% Ag and ≈80 wt% Ni), is in the range of the solid fractions commonly applied in such pastes (60-90 wt%).[80] Adding the secondary liquid, distilled water, leads to a strong increase in the suspension yield stress σ_y as can be seen in figure 32b. The yield stress of the pure suspension is 5 Pa for silver and 1 Pa in case of the nickel. This value increases by 400-fold for nickel and 140-fold for silver when adding 7 vol% and 5 vol%, respectively, of secondary liquid as measured to the total liquid volume. Distilled water does not preferentially wet the nickel or silver particles in terpineol, forming contact angles of 130° and 156° placing these mixtures in the capillary state. The particle clusters including small volumes of secondary liquid form a sample-spanning network as evident from the strong increase in yield stress with increasing amount of secondary liquid.[8] The capillary network allows for a stabilization of the

particles without additional polymeric stabilizers, which are commonly used in other paste formulations,[104,105] maintaining homogeneous mixtures during storage. Experiments with other systems have shown that capillary suspensions remain stable for long periods, even months, without phase separation.[33]

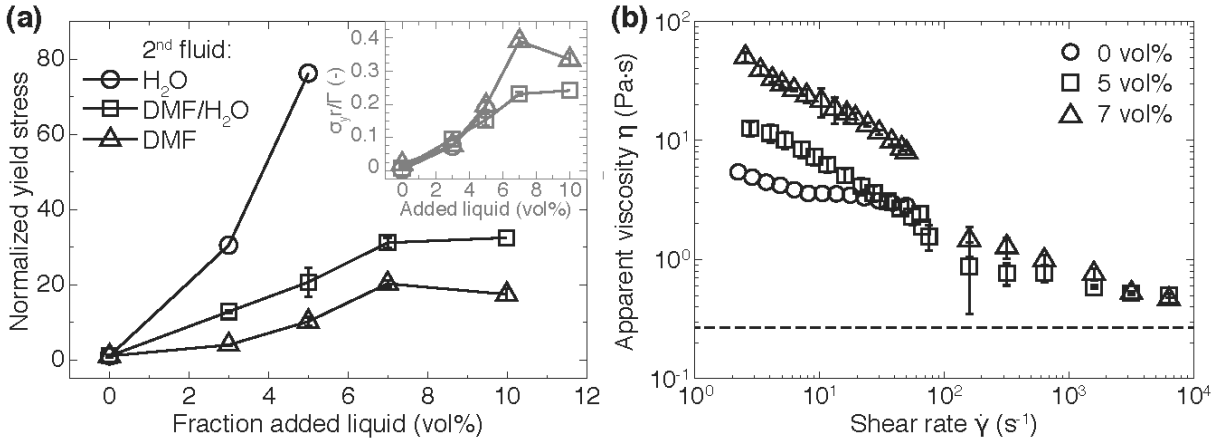

Fig. 33: a) Normalized yield stress as function of secondary fluid content for nickel capillary suspensions with paraffin oil as bulk fluid and different secondary liquids: DMF, DMF/H_2O-mixture (1:1 by vol.), and pure H_2O. The inset shows the yield stress σ_y normalized by the Laplace pressure (Γ/r). The solid volume fraction for all material combinations shown is $\phi = 0.20$. b) Viscosity η of nickel in terpineol suspensions ($\phi = 0.29$) as function of shear rate $\dot{\gamma}$ for varying water fractions. The dashed line shows the estimated high shear viscosity for the given solid loading assuming hard sphere particles.[106]

The strength of a capillary network is directly linked with the interfacial tension between the bulk and secondary liquid.[7] As such, a variation of the secondary liquid, including e.g. solvent mixtures, opens another possible route to adjust the flow behavior in order to meet the requirements of the desired printing technique or to improve the quality of the print in addition to varying the solids loading. Figure 33a shows the influence of the secondary liquid on the yield stress of the three phase system for nickel capillary suspensions with $\phi = 0.20$ in paraffin oil and three different secondary liquids: pure DMF, a DMF and water mixture (1:1 by volume), and pure water. The corresponding interfacial tensions for these combinations can be taken from table 5. DMF has the lowest interfacial tension of 6.0 mN/m, followed by the aqueous DMF mixture (15.6 mN/m). Pure water forms here the highest interfacial tension with 48 mN/m in the presence of paraffin oil. This trend in interfacial tension corresponds directly to the measured yield stress, i.e. network strength. Pure H_2O provides the steepest increase of the normalized yield stress when increasing the secondary fluid amount. For the case of the DMF/H_2O mixture, a maximum in network strength is reached with 7 vol% added liquid followed by a plateau of the yield stress. The pure DMF also has a maximum in the normalized yield stress at 7 vol%, but shows a loss in network strength at higher added fluid contents. The yield stress values for the aqueous DMF capillary suspensions are higher than the pure DMF capillary suspensions at each secondary fluid content due to the higher interfacial tension.

Table 5: Particles and solvent combinations used for capillary suspension formulations described in this paper along with their interfacial tension. All of the capillary networks were in the capillary state where the secondary liquid does not preferentially wet the particles.

	Bulk phase	Secondary liquid	Interfacial tension Γ [mN/m]	Network type
Nickel				
	Terpineol	Water	8.5	Capillary state
	Paraffin oil	Water	48.0[107]	Capillary state
	Paraffin oil	DMF/water (1:1)	15.6	Capillary state
	Paraffin oil	DMF	6.0	Capillary state
Silver				
	Terpineol	Water	8.5	Capillary state

This direct influence of the interfacial tension Γ can also be seen in the inset to figure 34a showing the yield stress σ_y normalized by the Laplace pressure Γ/r, where r is the mean particle radius. The curves overlap for the lower secondary fluid contents, but the DMF and DMF/H_2O curves diverge for the higher amounts. This divergence might be due to differing cluster structures presumably occurring at higher secondary fluid content.[8]

During the application or coating step, the inks are subjected to high shear rates that vary strongly with the chosen printing technique (e.g., screen printing $\dot{\gamma} \approx 100$ s^{-1}, dispensing $\dot{\gamma} \approx 10{,}000$ s^{-1}) followed by a deformation rate close to zero when the ink settles on the substrate.[52,95] Therefore, the inks are required to exhibit low high-shear viscosity that allows the ink to easily flow when passing through the screen mesh or dispensing nozzle during application. At the same time it should possess a high low-shear viscosity and a fast network recovery providing good shape accuracy to the printed structure. Figure 33b shows the rheological response of the capillary suspensions containing nickel particles ($\phi = 0.29$) to different shear rates. Measurements at shear rates below 100 s^{-1} were performed with a rotational rheometer and higher shear rates (up to 10^4 s^{-1}) were achieved using a capillary rheometer. As already shown for the TiO_2 capillary suspensions (see figure 24), the viscosity η is strongly dependent on the amount of secondary liquid in the low shear regime ($\dot{\gamma} < 100$ s^{-1}). Comparing η at $\dot{\gamma} = 10$ s^{-1} shows an increase of one decade for 7 vol% of secondary liquid when compared to the pure nickel suspension. All of the samples shown here demonstrate shear-thinning behavior. In the high shear regime ($\dot{\gamma} > 100$ s^{-1}) the viscosity functions of the capillary suspensions begin to coincide and approach a plateau value $\eta = 3.5\eta_{\text{solvent}}$ estimated for the given particle loading of $\phi = 0.29$ using the phenomenological model of Quemada.[106] This is expected since at these high shear rates, the viscosity should be solely determined by the solid volume fraction and demonstrates that the capillary network is completely broken. The pure nickel suspension is not stable at very higher shear rates, leading to

phase separation during the capillary rheometry measurements and these data are excluded from the figure.

4.2.2 Electrical properties

Nickel as well as silver capillary suspensions with different amount of secondary fluid were coated on quartz glass substrates and sintered at 800 °C in order to compare their electronic properties with those of model Ni and Ag suspensions including different binders and thixotropic agents as well as commercially available silver pastes. The heating rate in the sinter oven was 15 K/min, the fastest heating rate achievable, in order to simulate the firing profile in a belt furnace during solar cell production. The resulting sheet resistance R_{sheet} after annealing was measured using the Van-der-Pauw method and used to calculate the bulk resistance $R = R_{sheet} \cdot d$ together with the corresponding sheet thicknesses d after annealing. Corresponding data for the systems mentioned above are displayed in figure 34.[91,93]

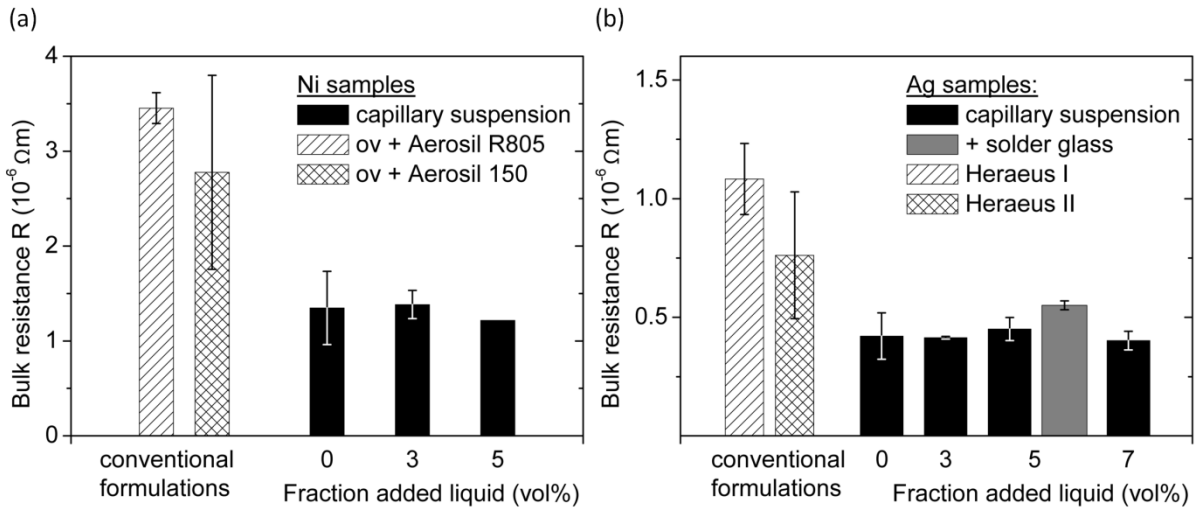

Fig. 34: Bulk resistance *R* for a) nickel and b) silver capillary suspensions ($\phi_{Ag/Ni} = 0.29$) compared to commercial paste formulations. For the nickel, the conventional formulations were prepared according to a Heraeus patent with an organic vehicle (ov) and two different thixotropic agents (Aerosil R805 and Aerosil 150) using the same particle fraction. Heraeus I and II are commerical silver pastes (solid volume fraction 90.0 and 90.5 wt%, respectively). In addition, a silver capillary suspension with 5 vol% water and 5 wt% solder glass is also shown ($\phi_{total} = 0.33$). Variance in sheet thickness was measured and considered in the calculation of the bulk resistance.

The bulk resistance of nickel based capillary suspensions along with two other commercial formulations are shown in figure 34a and the silver based suspensions and two commercial silver screen printing inks from Heraeus Precious Metals (denoted as Heraeus I and II) are shown in figure 34b. The capillary suspensions prepared with nickel and silver show no distinct trend with increasing amount of secondary liquid. The average bulk resistance of the nickel capillary suspensions is $R_{\text{Ni, capillary suspensions}} = 1.3 \pm 0.1 \times 10^{-6}$ Ωm and $R_{\text{Ag, capillary suspensions}} = 0.42 \pm 0.02 \times 10^{-6}$ Ωm for the silver capillary suspensions. Obviously, the addition of secondary liquid to the wet suspensions

does not affect the electronic properties of the produced nickel and silver layers. We can, therefore, ensure stability and tune the rheology of the paste to meet the demands of different printing methods without significantly varying the conductivity. However, these capillary suspension formulations clearly differ from conventional formulations including stabilizer, binder and rheology modifier. The conventional nickel suspensions were prepared following a patent for the formulation of an organic vehicle (abbreviated as ov in the figure) that is used for silver based screen printing pastes, but also suggested for other metal particles such as nickel.[80] The bulk solvent in these formulations was the same as used in the capillary suspensions (terpineol). Polyvinyl pyrrolidon (PVP) is added as an organic binder and surfactant to the pure nickel-terpineol suspension and ethyl cellulose as an additional binder or thickener as described in more detail in the experimental section. Two common thixotropic agents are then added to this organic vehicle: the hydrophobic Aerosil® R805 or the hydrophilic Aerosil® 150.[108] The pastes were prepared following the patent (as is described in the experimental section) and were subjected to the same heat treatment used for the capillary suspensions. The bulk resistance of these conventional formulations is increased by a factor of two ($2.8 \pm 1.0 \times 10^{-6}$ Ωm) for the Aerosil 150 and threefold for the Aerosil R805 formulation ($3.5 \pm 0.2 \times 10^{-6}$ Ωm) compared to the nickel capillary suspensions (figure 35a) despite having the same loading of nickel particles. The higher bulk resistance may be attributed to the interference of additive residues in the organic vehicle as has been previously reported.[3–6] This is supported by sheet thickness measurements shown in figure 35. Figure 35a shows the sheet thicknesses of the nickel based suspensions. The capillary suspensions exhibit an average sheet thickness of 185 ± 13 µm and the thickness of the conventional nickel formulations is about 10 % higher according to the increased total solids volume caused by the addition of the non-volatile additives that remain in the layer even after sintering. (The volume fraction of nickel, $\phi_{\mathrm{Ni}} = 0.29$ is the same for both the capillary and conventional formulations).

A similar difference in bulk resistance is found when silver capillary suspensions are compared to commercial silver pastes including additional components, e.g. thixotropic agent, polymeric stabilizer and other additives (figure 34b). The two commercial formulations, Heraeus I and II exhibit a bulk resistance $R_{\mathrm{Heraeous\,I}} = 0.76 \pm 0.27 \times 10^{-6}$ Ωm and $R_{\mathrm{Heraeus\,II}} = 1.1 \pm 0.15 \times 10^{-6}$ Ωm, respectively that is about double the value of the silver capillary suspensions when coated and sintered under similar conditions. Presumably, the additives in the commercial pastes do not evaporate or decay completely during the firing step and diminish the conductive properties of the silver layer. The additives may have an additional effect on the structure of the sintered layer here. The capillary silver suspensions exhibit a substantially lower sheet thickness (123 ± 5 µm) than corresponding nickel samples (185 ± 13) µm. With a much higher melting point of 1455 °C (961 °C for silver), the nickel samples do not undergo as strong densification as the silver samples during the sintering procedure applied here. However, the commercial silver pastes exhibit a sheet thickness even higher than the nickel samples and this cannot solely be attributed to the remaining additives or the different particle

loading. Based on the solid loading reported by the supplier and assuming that the paste consists of silver and terpineol, we estimate an upper limit of silver content $\phi_{\mathrm{Ag}} = 0.44$ and accordingly a sheet thicknesses of 180 µm is expected for the conventional silver formulations. As shown in figure 36b the measured values of 242 µm (Heraeus I) and 293 µm (Heraeus II) exceed this value by far. Therefore, we hypothesize that the additives prevent a complete collapse of the particle network during sintering. Such a particle network would have fewer particle contacts than the denser capillary suspension layer and, accordingly, a lower conductivity, i.e. higher resistance.

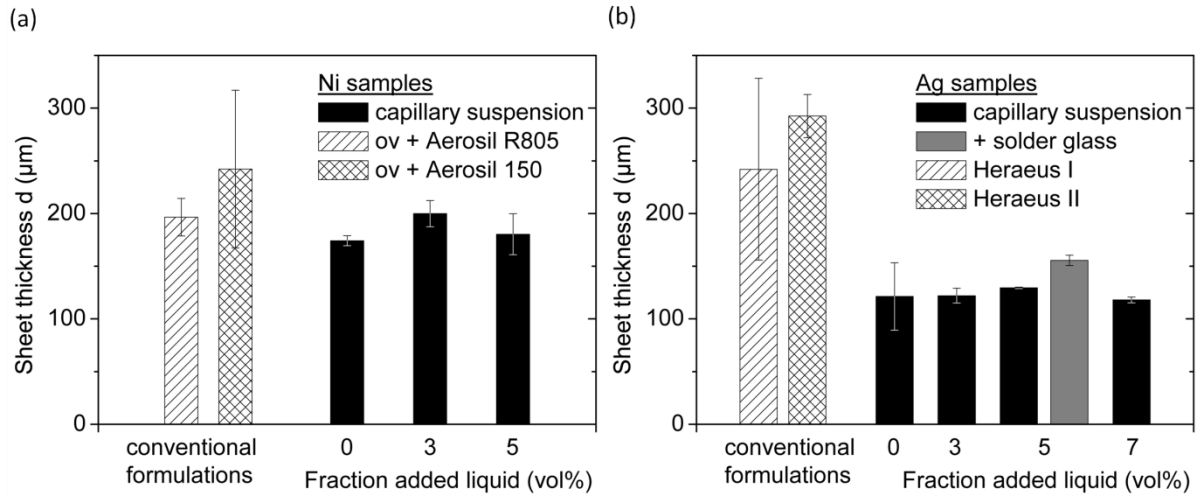

Fig. 35: Sheet thickness obtained for a) nickel and b) silver capillary suspensions ($\phi_{\mathrm{Ag/Ni}} = 0.29$) compared to commercial paste formulations. For the nickel system, the conventional formulations were prepared according to a patent (ref) using an organic vehicle (ov) and two different thixotropic agents (Aerosil R805 and Aerosil 150) using the same particle fraction. Heraeus I and II are commercial silver pastes (solid volume fraction 90.0 and 90.5 wt%, respectively). In addition, data for a silver capillary suspension with 5 vol% water and 5 wt% solder glass is also shown ($\phi_{\mathrm{total}} = 0.33$).

4.2.3 Shape Profile of wet contact lines

Capillary suspensions exhibit a high yield stress and pronounced shear thinning. The clear advantage of this unique flow behavior in comparison to the pure metal particle suspension is demonstrated in an application oriented printing test, corresponding results are shown in figure 36. A top view on the wet contact lines taken directly following the application of the capillary suspension with terpineol continuous phase on a glass substrate with a doctor blade and 300 µm wide slot stencil is shown in figure 36a for the nickel suspension ($\phi = 0.29$) and 36c for the silver suspension ($\phi = 0.29$) with an average maximum line height of 190 ± 27 µm. The top images show the line widths obtained for the suspensions without any secondary liquid and the bottom with added water. Figure 36b and figure 36d show the cross sectional height profiles for nickel and silver capillary suspensions, respectively, normalized to their maximum height. Profiles are plotted as function of the x-position from the center, thus the distinct changes in shape are clearly visible. The pure suspensions both spread on the substrate far beyond the 300 µm mask (denoted by the vertical lines in the images) with the nickel

suspension demonstrating a spreading of the pure solvent beyond the borders of the paste due to the limited stability, i.e. phase separation. For the nickel capillary suspension with 5 vol% added water, less solvent spreads under the glass stencil. Thus solvent loss is reduced and the line width decreases from 1008 ± 163 µm with no added secondary liquid in the sample to 500 ± 37 µm. The error intervals given here and in the subsequent part of this section reflect the variation of the line width along the printed line, i.e. y-direction.

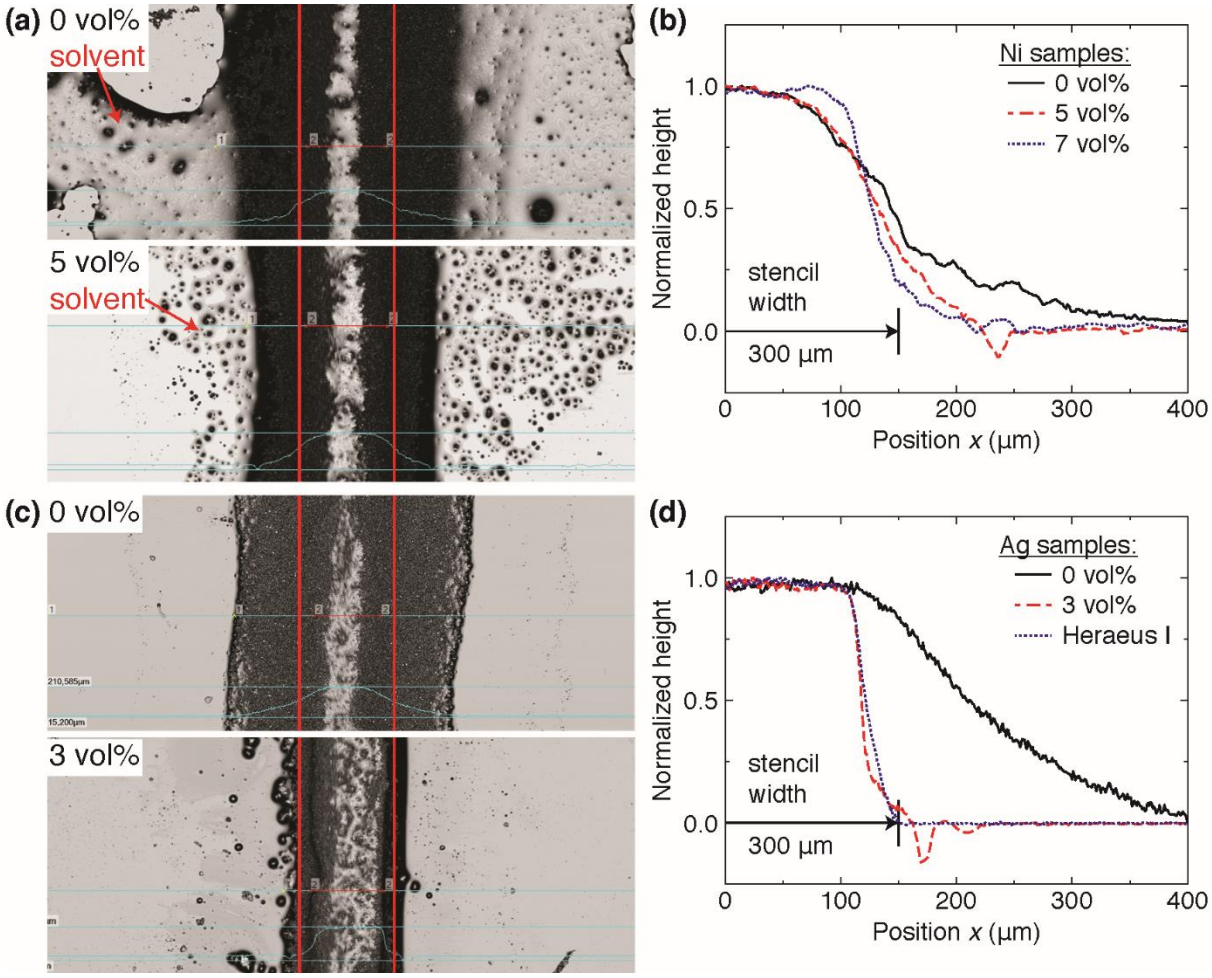

Fig. 36: Wet contact lines for a) nickel and c) silver suspensions using a mask of width 300 µm (red vertical lines). The light grey areas and black spots are from the pure solvent, where the contrast is controlled by the drop height. Cross sectional profile for lines printed with b) nickel and d) silver capillary suspensions. All suspensions were prepared in terpineol with varying amounts added water and have a solid fraction $\phi = 0.29$. Additionally, a commercial silver sample (Heraeus I) is plotted for comparison with the silver capillary suspensions.

The line width further drops to 470 ± 28 µm and the height profile changes from bell-shaped to almost rectangular with a flat top and minimal spreading when 7 vol% of water is added. Hence, the addition of the secondary liquid leads to a decrease of the line width and an improved uniformity of the profile along the direction of the printed line. The dip of the profile with 5 vol% added liquid close to the sample edges are attributed to measurement errors: Surface topology of the crack-free wet lines has been measured with a 3D laser scanning microscope. Negative values can occur due to the

reflection of the beam from the bottom interface or imperfections within the substrate instead from the top interface of the glass substrate. This type of error, due to the sharp discontinuity in reflection, occurs at the edge of the printed line and reflective substrate.

A similar correlation between amount of secondary liquid and line width is found for the silver samples (see figure 36c and 36d). Adding just 3 vol% of water to the silver suspension reduces spreading and the line width decreases from 644 ± 143 µm to 322 ± 30 µm. Moreover, the cross section changes from bell-shaped into a rectangular shape. The required lower amount of secondary liquid corresponds to the higher yield stress of the silver suspensions at a given amount of added liquid compared to the nickel system. Additionally, figure 36d shows the profile of a commercial silver sample (Heraeus I) obtained under similar application conditions. The rectangularity (area under the profile compared to the minimum bounding rectangle) of this profile is 0.74 and the corresponding value for the capillary suspension with 3 vol% added water is 0.67. This demonstrates that the capillary suspension formulation is competitive to the conventional formulation with regard to shape accuracy but the sharp rectangular profile is achieved at lower particle loading compared to the commercial paste and without non-volatile organic additives. Such a rectangular line profile increases the cross-sectional area while maintaining a small footprint. This should result in a high conductivity when printing, e.g. small scale circuit boards with fine lines.

4.2.4 Capillary suspensions with nickel flakes

Capillary suspensions were also created using nickel flakes with an average particle size of 11 µm and an aspect ratio of 20:1. Flake shaped particles have been suggested for conductive pastes in order to increase the contact area between adjacent particles and thus reduce the contact resistance at the grain boundaries.[109] The formulation of capillary suspensions with nickel flakes only was not able due to the strong shear-thickening characteristic of the nickel flake suspensions. Therefore, mixtures of flakes and spheres (sphere size: 3-7µm) were created with a constant solid loading of $\phi = 0.25$ and three different flake fractions (5 vol%, 3 vol% and 1 vol%). Paraffin oil served as bulk fluid and DMF as secondary liquid. Figure 37a shows the yield stress as function of the added secondary liquid for the different solid compositions. The yield stress values without added secondary liquid are for all solid compositions in the range of 31 ± 5 Pa. For 5 vol% of flakes the yield stress decreases with increasing amount of secondary liquid, thus a capillary network formation cannot be observed. For 3 vol% and 1 vol% of flakes in the solids mixture the yield stress values increase by a factor of 5.6 resp. 4.5 with the addition of 10 vol% and 7 vol% DMF. Figure 37a gives evidence that the nickel flakes do not contribute to the capillary network formation and that a minimum amount of nickel spheres is necessary for this material system to form a stable capillary network.

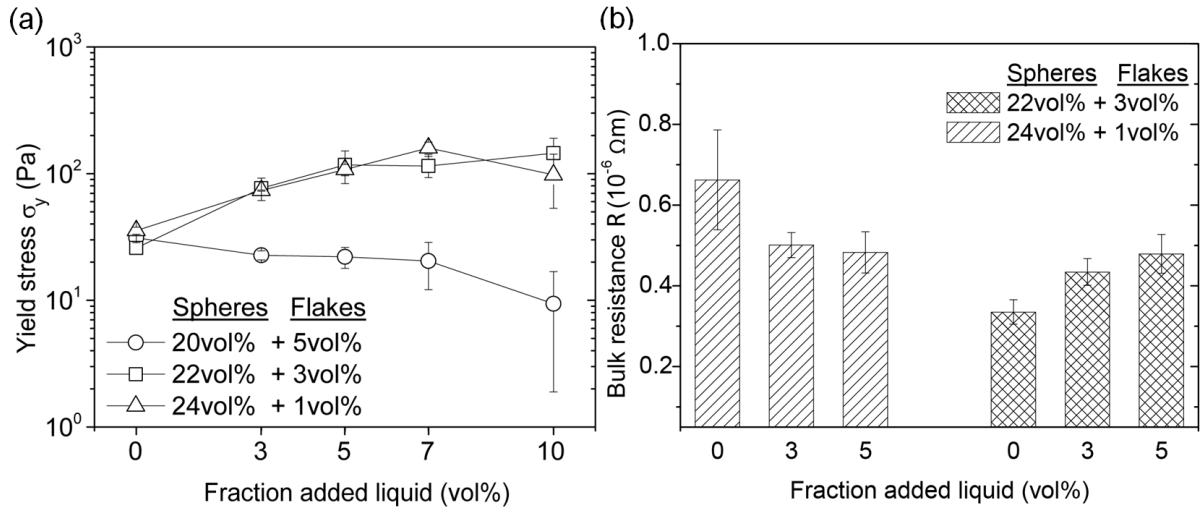

Fig. 37: a) Yield stress as function of added secondary liquid amount for three different solid compositions of nickel spheres and flakes. Bulk fluid: paraffin oil, secondary liquid: DMF. b) Bulk resistance for two different solid compositions as function of the secondary liquid amount. Total solid loading $\phi = 0.25$ is constant for all samples shown here.)

The solid compositions, which were suitable for the formulation as capillary suspension, were coated on quartz substrates and sintered. The final bulk resistance of the 1×1 cm² sized nickel films is shown in figure 37b. For 3 vol% of flakes the measured bulk resistance shows no clear dependency on the fraction of secondary liquid. Bulk resistance is in the range of $5.5 \pm 1.0 \times 10^{-7}$ Ωm. With the smallest flake fraction of 1 vol% the bulk resistance measurements show a small increase of the bulk resistance with increasing DMF fractions. The bulk resistance values are in the range of $4.2 \pm 0.7 \times 10^{-7}$Ωm. In comparison with the capillary suspensions, which were created purely with nickel spheres dispersed in terpineol and water as secondary liquid, bulk resistance values are approximately half a decade lower here. This could be attributed to the flake shaped particles which provide a higher area of contact between the planar surfaces of the flakes in contrary to the point contacts formed between the nickel spheres. Another possibility is the longer conductive path along the longitudinal axis of a single particle without grain boundaries. An influence of the reducing agent DMF could not be observed here and it is assumed that the amount of added DMF is not sufficient to reduce surface oxidation from the total particle surface area. Another explanation could be the network type, here capillary state, where the secondary liquid wets the particles worse than the bulk fluid and therefore has a smaller wetting contact area on the particle surface as it is possible with a pendular state system. Considering the sheet thickness after the sintering process, which is depicted in figure 38, the addition of the secondary fluid leads to an increase of the coated and sintered layer. This can be attributed to the capillary network which obviously persists the coating step and does not collapse entirely during sintering as annealing temperature is far below the melting point of nickel. For the capillary suspensions with 3 vol% and 5 vol% of added secondary liquid the sheet thickness values are in the range of 154 ± 10 µm with 3 vol% flakes in the solid composition and 182 ± 18µm with only 1 vol% of flakes.

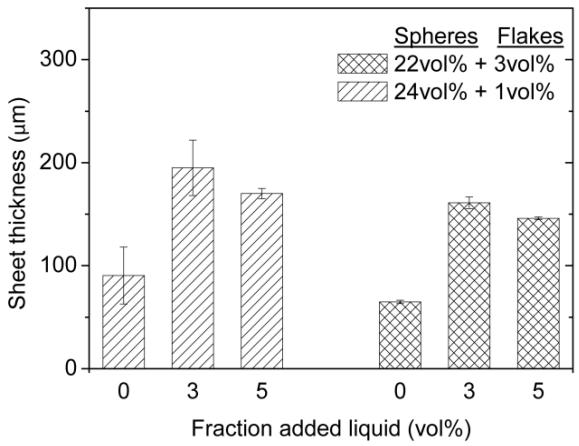

Fig. 38: Sheet thickness of capillary suspensions made with a mixture of nickel spheres and flakes measured after the sintering process.

Sheet thickness was not affected, when using the terpineol as bulk fluid and water as secondary liquid. With similar interfacial tensions ($\gamma_{terpineol/water} = 8.5$ mN/m, $\gamma_{paraffin\ oil/DMF} = 6.0$ mN/m) and three-phase contact angles ($\theta_{Ni,terpineol,water} = 137$ °, $\theta_{Ni,paraffin\ oil,DMF} = 130$ °) differences must arise from the irregular shape of the nickel flakes disturbing an even particle distribution. Considering the increase of the yield stress as function of the added secondary liquid for the nickel spheres dispersed in terpineol, discussed in chapter 6.2.1, and for the spheres and flakes mixtures dispersed in paraffin oil, the latter results in a less steep increase of the yield stress (approx. fivefold) and thus to a weaker capillary network. This leads to the assumption that the secondary fluid is not incorporated into the capillary network solely as single droplets in small particle clusters, but partially remains present as emulsion droplets finally leading to bigger voids in the coated layer.

4.2.5 Comparison of nitrogen and hydrogen as sintering atmosphere

Another approach to increase the conductivity of the sintered nickel layer by reduction of the surface oxidation on the metal particles is to add hydrogen during the sintering process.[110] This parameter was investigated with nickel particles (size: 3-7µm, $\phi = 0.15$) dispersed in paraffin oil using water as a secondary liquid. Alternatively, a aqueous silver nano dispersion ($\phi_{Ag} = 0.013$), stabilized with PVP, was synthesized and used as secondary liquid, in order to examine the influence on the electric properties. The melting point of silver is 961 °C, which corresponds to two-thirds of the nickel melting temperature, and could therefore form solid bridges with good conductivity between the particles at the applied sintering temperature of 800 °C. Figure 39a shows the yield stress as function of the added secondary liquid.

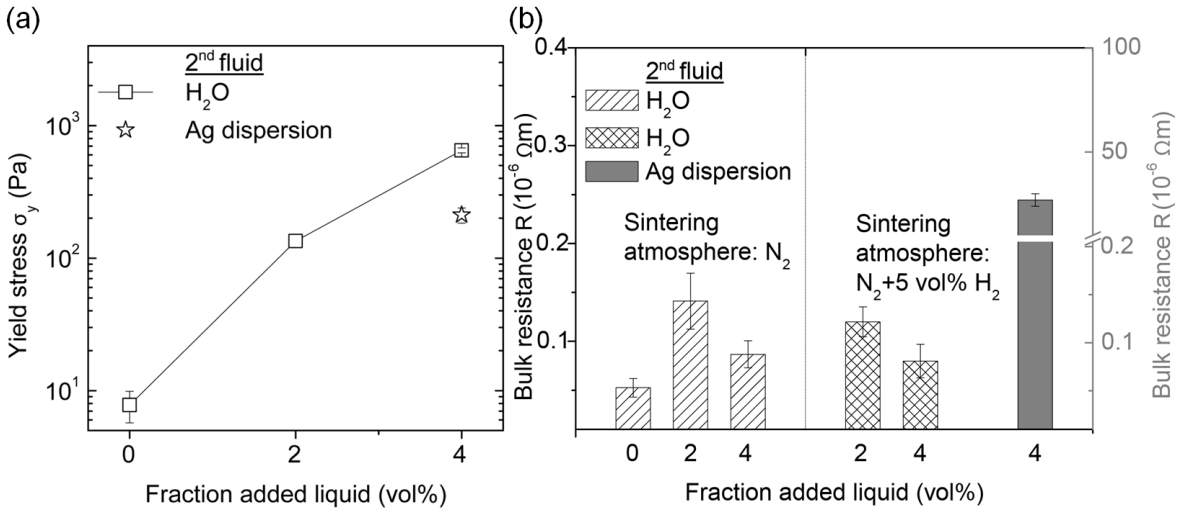

Fig. 39: a) Yield stress of nickel spheres dispersed in paraffin oil and different amounts of water as secondary liquid. Additionally yield stress of a capillary suspension is plotted where an aqueous silver dispersion was used as secondary liquid. b) Corresponding bulk resistance for two different sintering atmospheres: pure nitrogen and a mixture of nitrogen and 5 vol% hydrogen.

As seen in chapter 4.2.1, nickel spheres, dispersed in paraffin oil, form a strong capillary network when small amounts of water are added. With $\phi = 0.15$ the pure nickel suspension in paraffin oil has a yield stress of 8 Pa and increases to 134 Pa when adding 2 vol% of water. With 4 vol% secondary liquid this yield stress increases further to 650 Pa. The addition of 4 vol% of the aqueous silver nanoparticles dispersion yields a lower value of 211 Pa, which can be attributed to the PVP molecules and their influence on the interfacial tension.[111] According to equation 2 in section 2.1 the capillary force between two particles connected by a liquid bridge is depends linearly on the interfacial tension. Consequently, the reduction of the interfacial tension due to the presence of PVP leads to a weaker network and hence to a lower yield stress.

The resulting bulk resistance, which was measured after sintering the nickel pastes in nitrogen atmosphere and additionally also in a nitrogen/hydrogen mixture (19:1 by volume) can be seen in figure 39b. The bulk resistance values of the samples sintered in pure nitrogen and with water as secondary liquid are in the range of $0.93 \pm 0.5 \times 10^{-6}$ Ωm and resistance appears to be independent of the secondary liquid amount. The bulk resistance shows no significant shift, when changing the sintering atmosphere to the nitrogen/hydrogen mixture, with an average value of $1.00 \pm 0.28 \times 10^{-6}$ Ωm. The sample with 0 vol% H_2O sintered in the gas mixture is not depicted here as the value ($4.36 \pm 3.37 \times 10^{-3}$ Ωm) exceeds the other measurement values by far, which is more likely due to sample handling errors rather than a material specific phenomenon. Using the silver nanoparticle dispersion as secondary liquid does not lead to the desired improved conductivity resp. lower bulk resistance in comparison to the samples created with pure water as secondary liquid. Instead the bulk

resistance is strongly increased to a value of $26.90 \pm 0.30 \times 10^{-6}$ Ωm, which is approximately the 27-fold of the average value for the silver free samples regardless of the chosen sintering atmosphere.

The influence of the reductive hydrogen could be more pronounced for a different sintering profile with longer duration of the maximum temperature or alternatively with a higher hydrogen fraction than it is stated in [110]. The average sheet thickness of the samples with water as secondary liquid was 162 ± 68 µm. Adding the silver dispersion as secondary liquid yields an average sheet thickness of 277 ± 55 µm, which is clearly higher than without the PVP stabilized silver particles. This supports the assumption that the presence of polymers as stabilizer hinders the formation of a dense particle structure and, taking the high bulk resistance values into account, a good contacting of the particles, even after the high temperature treatment. The presence of the Ag nanoparticles appears to be less influential and it is assumed that the concentration of Ag within the secondary liquid (1.3 vol%) was chosen too low to show an effect and that the stabilizer PVP dominates the final product properties. A measurement of the solids content in the silver dispersion showed, that PVP was not separated by centrifugation after the synthesis but remains in the secondary liquid ($\phi_{PVP} \approx 0.1$). An insulating oxidation layer on the silver particles AgO can be excluded because AgO decomposes into silver and oxygen when exposed to processing temperatures above 400 °C.[112]

4.2.6 Using particles with a polydisperse size distribution

Another approach to improve the electronic properties of the sintered layers is to change the particle size distribution in order to achieve a denser particle packing and reduce the non-conductive voids within the layer. Random close packing for a monomodal particle size distribution is 0.63, but greater for polydisperse systems, where the maximum packing fraction depends strongly on respective size distribution. In this experiment the nickel spheres are partially replaced by sub-micron sized nickel particles ($\phi_{sub-micron\ Ni} = 0.034$). The total volume fraction of nickel ($\phi = 0.15$) remains constant. The resulting yield stress of the capillary suspensions with 2 vol% and 4 vol% added water are depicted in figure 40a. In comparison to the values which were achieved for the capillary suspension with purely 3-7µm sized particles, the sample with 2 vol% added secondary liquid show a similar yield stress, whereas the sample with 4 vol% secondary liquid differ strongly. The sample with sub-micron particles has a yield stress of 230 Pa, which is just a third of the yield stress value when using particles with a diameter of 3-7 µm only. As already seen for the capillary suspensions prepared with spherical and flake shaped particles, the nickel spheres with a size of 3-7 µm contribute well to the formation of a capillary network. For the here displayed examples, the additional nickel particles of different size or shape do not strengthen this network further.

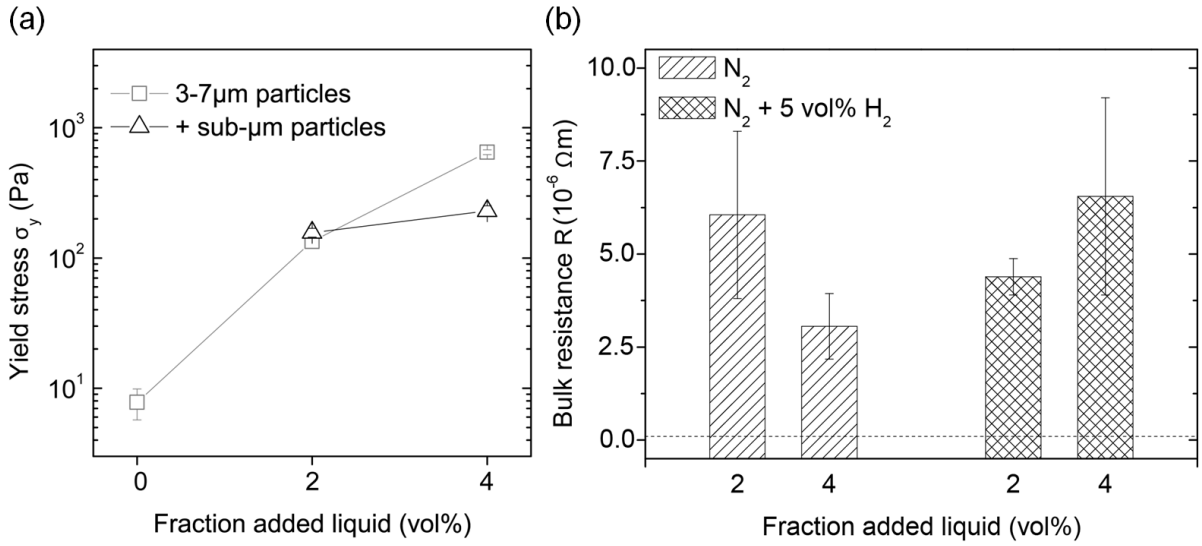

Fig. 40: a) Yield stress for nickel based capillary suspensions made with particles with a diameter of 3-7 µm and additionally sub-micron sized particles as function of the secondary liquid content. Yield stress function with purely 3-7 µm sized particles is also given for comparison. b) Bulk resistance for the sinterd capillary suspensions made with polydisperse sized nickel particles as function of the added secondary liquid amount. Nickel was dispersed in paraffin oil with water as secondary liquid. Sintering atmosphere was nitrogen and alternatively a nitrogen/hydrogen mixture.

Considering the yield stress function for the polydisperse nickel particle samples in figure 40a, the capillary network appears to be saturated with 2 vol% of secondary liquid and a further increase of the secondary liquid amount does not lead to a significant yield stress increase anymore as it could be seen for the samples made with the nickel particles with a range of size of 3-7 µm only. Figure 40b shows the bulk resistance values which were achieved when using the particle mixture for preparing the capillary suspensions with 2 vol% and 4 vol% added secondary liquid after sintering in nitrogen and additionally also in the nitrogen/hydrogen gas mixture. The dashed line marks the average resistance value for the 3-7µm sized nickel spheres sintered in nitrogen, taken from figure 39. This line of reference shows that the admixture of different particle sizes does not yield an improved conductivity, because bulk resistance is clearly increased. The samples sintered in nitrogen lead to resistance values of $R = 6.05 \pm 2.25 \times 10^{-6}$ and $R = 3.06 \pm 0.88 \times 10^{-6}$ for 2 vol% and 4 vol% added secondary liquid, respectively. Similar to the previous example, the change of the sintering atmosphere to the nitrogen/hydrogen mixture does not lead to a remarkable change of the bulk resistance. The sample prepared with 2 vol% of water and sintered in the H_2/N_2 atmosphere has a resistance of $R = 4.39 \pm 0.49 \times 10^{-6}$ Ωm and is slightly lower than the sample with 4 vol% added secondary liquid with a resistance of $R = 6.55 \pm 2.65 \times 10^{-6}$ Ωm. Considering the measurement error, the sintering atmosphere and amount of secondary fluid do not influence the resulting bulk resistance. Whereas the grain size clearly affects the electronic properties and leads to a significant higher average bulk resistance. Due the addition of the sub-micron particles at constant solid loading, the total number of grain boundaries is increased and current flow is hindered by a serial connection of contact resistances,

which are, in the worst case, covered by an insulating oxidation layer. The average sheet thickness of the samples was 150 ± 37 µm. In comparison to the samples prepared with purely 3-7µm sized particles (average sheet thickness: 162 ± 68 µm) no significant densification of the sintered layer could be observed.

4.2.7 Metal capillary suspensions with low solid loading

High volume fractions of metal, e.g. silver, are preferred in conductive pastes in order to achieve a dense packed structure in the final product with good conductivity. Nevertheless, also lower volume fractions than presented so far are possible for the formulation as capillary suspension. Silver particles, dispersed in diisononyl phthalate, form a three-phase contact angle of 145° when water is added to the system. Therefore this material combination is placed in the pendular state. Silver capillary suspensions have been prepared containing 9 vol% of silver particles and the yield stress was measured in order to examine the formation of the capillary network. For the reference suspension without added secondary liquid yield stress was not measureable, with no distinct and sudden increase of the deformation as function of the applied stress. After adding 0.3 vol% of water to the suspension and homogenization, the capillary network is formed along with a yield stress of 1707 ± 187 Pa. Figure 41 shows the suspension without added secondary liquid on the left. Sample slumps down and a solvent ring, due to the phase separation is clearly visible. The sample with 0.3 vol% water is shown on the right side. The sample maintains the shape due to the formation of the capillary network and the strong yield stress. Consequently, the range of the solid loading for metal particles, investigated here, can vary strongly between 9 vol% and 29 vol% and depends on the chosen solvent combination.

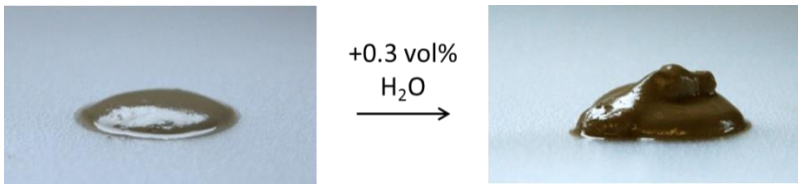

Fig. 41: Silver particles dispersed in DINP. Left: without added secondary liquid. Right: After the addition of 0.3 vol% of water.

5 Summary

In summary, this thesis has shown that the capillary suspension concept can be used to stabilize inorganic particles used in conductive pastes for printed electronic applications without using polymeric or other non-volatile organic additives, which can remain in the sintered part thereby reducing conductivity. Capillary suspension based silver and nickel pastes suitable for screen printing resulted in an at least twofold higher conductivity of the corresponding sintered layer compared to conventional, commercial pastes processed under similar conditions. The yield stress of these capillary suspensions can be tuned to provide stability of the pastes during storage, processing or application, and the degree of shear thinning can be adjusted to enable easy flow through printing meshes or nozzles. This tunable rheology is demonstrated here using both nickel and silver particles with a combination of bulk solvents and secondary fluids, but can be applied to other combinations using inorganic or even organic conductive particles. Furthermore, the unique flow behavior results in a high shape accuracy of the printed pattern. Lines with almost rectangular cross section are demonstrated. Such lines with a high aspect ratio are desired for small scale circuits and even more complex, e.g. triangular shapes advantageous for the front side metallization of solar cells may also be possible. In addition to these benefits directly related to the unique flow behavior, the capillary suspension concept offers a significant advantage in printed electronic applications due to the lack of non-volatile organic additives. This high purity formulation results in a denser layer with higher conductivity in comparison to conventional formulations.

Beyond the significant key improvements demonstrated here, the capillary suspension concept offers additional opportunities particularly relevant for printed electronic applications. A wide variety of particle sizes and shapes in addition to possible solvent combinations can be used. This offers not only an additional degree of freedom to obtain a desired flow profile, admixtures of micron and sub-micron sized particles may be used to achieve a more dense particle packing as shown for the nickel particles. Here, the admixture of micron and sub-micron particles led to a densification of the sintered layer by 7 %, even though the bulk resistance increased by at least thirtyfold, which is attributed to the increased number of grain boundaries and therefore higher number of contact resistances per volume. Formulation of capillary suspensions with micron sized spherical nickel particles and nickel flakes was also achieved, provided that a major fraction of the solid volume content (minimum 88 %) consists of nickel spheres in order to form a stable network. Bulk resistance of the flake and sphere admixtures showed an improvement of the electronic properties by a factor of 2, possible due to the greater contact area between adjacent flakes and the longer conductive path along the longitudinal axis of the flakes. The investigation of the influence of the sintering atmosphere using either nitrogen or a mixture of nitrogen and reductive hydrogen showed that the resulting bulk resistance values do not decrease when 5 vol% of reductive hydrogen is present during the annealing process. The possible

volume fraction of particles necessary for a successful capillary network formation ranges from 9-29 vol% and is shown here for silver in different solvent combinations.

Finally, the secondary fluid may be chosen as a highly efficient reducing agent (e.g. DMF) selectively removing oxidized surface layers in the particle contact regions. The nickel suspensions examined in this thesis focused on the capillary state networks formed with DMF in paraffin oil and no effect was found. In conclusion, it is suggested to investigate the application of DMF as secondary liquid within a pendular state system. This thesis has shown that the capillary suspension concept is an innovative formulation platform ideally suited to design pastes for printed electronic applications with improved processing and conductivity properties. This formulation method requires less expensive ingredients (e.g. water rather than specialized polymers) and offers a promising pathway to increase the conductivity beyond the twofold increase shown here. The proposed high conductivity formulation concept may even enable silver to be replaced, e.g. in large scale applications like solar cells, by more abundant conductive materials such as copper in the future.

The formulation of capillary suspensions based on metal oxides was successful for TiO_2, ZnO and Al_2O_3 using n-octanol as bulk solvent and water as secondary liquid. For these kind of material systems, a route to create crack-free particulate films is demonstrated with minimal processing and material cost just by adding small amounts of a secondary liquid to a suspension thus introducing capillary bridges between particles. Microscopy images reveal a remarkable change in the crack pattern of dry films made from suspensions with varying amounts of secondary liquid for TiO_2, ZnO and Al_2O_3 systems. Moreover, IR spectroscopy revealed that the drying rate could be remarkably increased using the capillary suspension concept. Significantly, the capillary suspension concept offers a promising pathway for time-efficient production of crack-free films from high purity formulations since additional organic stabilizing agents or polymeric additives used to prevent sedimentation, to control flow properties, or to prevent cracking are superfluous. These additives are often undesirable since they remain in the dry film degrading the properties, e.g. the conductivity in printed electronics, and may even persist after sintering.

Further material properties regarding the application of capillary suspensions as printing pastes were performed with the model system, here TiO_2 capillary suspensions. Printing requirements are met regarding the shear thinning viscosity function and the fast structural recovery after exposure to high shear processing steps. The line width is clearly decreased by addition of the secondary liquid, which also led to higher aspect ratios. After the addition of 5 vol% of water the line width reduced to 40 % of the width which was achieved when printing the suspension without added secondary liquid.

Summing up all the benefits, this thesis has proven the capillary suspensions concept as innovative tool for the formulation of printing pastes. Using many different inorganic particles and a wide range

of solvent combinations this phenomenon is able to be adapted flexibly to various printing techniques meeting respective processing requirements.

Future work should focus on the usage of the secondary liquid also as carrier for chemical reactions. One example shown in this thesis was the investigation of a capillary state system with nickel and a reducing agent (DMF) as secondary liquid, in order to improve the conductivity. But, more preferable and promising is a pendular state material system where the droplets are placed exactly at the point of contact between the particles. Also the possibility of adding nanoparticles to the secondary liquid is a good method in order to reduce the temperature during the firing process which is beneficial for example for less heat stable substrates. In this case, an improved formulation for the secondary liquid is necessary which contains fewer stabilizers than utilized in this work.
In general the capillary suspension phenomenon should be also approved for other particles, such as for example copper, and other printing techniques in order to further investigate the flexibility and versatility of this innovative stabilization method.

References

1. Zervos, H. Printed Electronics : a ‘ Game Changing ’ Technology. 2–3 (2015). Available at: http://www.semi.org/en/IndustrySegments/ctr_041175. (Accessed: 17th June 2015)

2. Mitzi, D. B. *Solution processing of inorganic materials*. (Wiley, 2009).

3. Mathews, N., Lam, Y. M., Mhaisalkar, S. G. & Grimsdale, A. C. Printing materials for electronic devices. *Int. J. Mater. Res.* **101,** 236–250 (2010).

4. Park, I. *et al.* Nanoscale patterning and electronics on flexible substrate by direct nanoimprinting of metallic nanoparticles. *Adv. Mater.* **20,** 489–496 (2008).

5. Habas, S. E., Platt, H. a S., Van Hest, M. F. a M. & Ginley, D. S. Low-cost inorganic solar cells: From ink to printed device. *Chem. Rev.* **110,** 6571–6594 (2010).

6. Kamyshny, A., Steinke, J. & Magdassi, S. Metal-based Inkjet Inks for Printed Electronics. *Open Appl. Phys. Journal,* **4,** 19–36 (2011).

7. Koos, E. & Willenbacher, N. Capillary forces in suspension rheology. *Science* **331,** 897–900 (2011).

8. Koos, E. & Willenbacher, N. Particle configurations and gelation in capillary suspensions. *Soft Matter* **8,** 3988 (2012).

9. Koos, E., Johannsmeier, J., Schwebler, L. & Willenbacher, N. Tuning suspension rheology using capillary forces. *Soft Matter* **8,** 6620 (2012).

10. Koos, E. Capillary suspensions: Particle networks formed through the capillary force. *Curr. Opin. Colloid Interface Sci.* **19,** 575–584 (2014).

11. Velankar, S. S. A non-equilibrium state diagram for liquid/fluid/particle mixtures. *Soft Matter* (2015). doi:10.1039/C5SM01901J

12. Bitsch, B. *et al.* A novel slurry concept for the fabrication of lithium-ion battery electrodes with beneficial properties. *J. Power Sources* **265,** 81–90 (2014).

13. Shoji, H. *et al.* Effect of Heat Treatment on Dielectric Properties of X7R Designated MLCs with Ni Internal Electrodes. *J. Mater. Synth. Process.* **6,** 415–418 (1998).

14. Vollmann, M., Hagenbeck, R. & Waser, R. Grain-Boundary Defect Chemistry of Acceptor-Doped Titanates: Inversion Layer and Low-Field Conduction. *J. Am. Ceram. Soc.* **80,** 2301–2314 (1997).

15. Antolini, E., Ferretti, M. & Gemme, S. Preparation of porous nickel electrodes for molten carbonate fuel cells by non-aqueous tape casting. *J. Mater. Sci.* **31,** 2187–2192 (1996).

16. Park, J. H. *et al.* Close-packed SiO2/poly(methyl methacrylate) binary nanoparticles-coated polyethylene separators for lithium-ion batteries. *J. Power Sources* **195,** 8306–8310 (2010).

17. Bardosova, M., Dillon, F. C., Pemble, M. E., Povey, I. M. & Tredgold, R. H. Langmuir-Blodgett assembly of colloidal photonic crystals using silica particles prepared without the use of surfactant molecules. *J. Colloid Interface Sci.* **333,** 816–9 (2009).

18. Prevo, B. G., Hon, E. W. & Velev, O. D. Assembly and characterization of colloid-based antireflective coatings on multicrystalline silicon solar cells. *J. Mater. Chem.* **17,** 791–799 (2007).

19. Özgür, C. & Şan, O. Fabrication of superhydrophilic membrane filters using spherical glass particles obtained by ultrasonic spray pyrolysis. *Ceram. Int.* **37,** 965–970 (2011).

20. Winnik, M. A. Latex film formation. *Curr. Opin. Colloid Interface Sci.* **2,** 192–199 (1997).

21. Almanza-Workman, A. M., Taussig, C. P., Jeans, A. H. & Cobene, R. L. Fabrication of three-dimensional imprint lithography templates by colloidal dispersions. *J. Mater. Chem.* **21,** 14185 (2011).

22. Tang, X. Crack-free TiO2 thin films with selfassembling nano-particles fabricated through in-situ sol–gel processing in reverse micelles. *Surf. Coatings Technol.* **221,** 37–43 (2013).

23. Herminghaus, S. Dynamics of wet granular matter. *Adv. Phys.* **54,** 221–261 (2005).

24. Koos, E. Capillary suspensions: Particle networks formed through the capillary force. *Curr. Opin. Colloid Interface Sci.* **19,** 575–584 (2014).

25. Herzig, E. M. Bijel a novel composite material from colloids on liquid-liquid interfaces School of Physics. (University of Edinburgh, 2008).

26. Herminghaus, S. *Wet granular material: a truly complex fluid*. (World Scientific Publishing Co. Pte. Ltd., 2013).

27. Schubert, H. Capillary forces - modeling and application in particulate technology. *Powder Technology* **37,** 105–116 (1984).

28. Butt, H. J. & Kappl, M. Normal capillary forces. *Adv. Colloid Interface Sci.* **146,** 48–60 (2009).

29. Mehrotra, V. P. & Sastry, K. V. S. Pendular bond strength between unequal-sized spherical particles. *Powder Technol.* **25,** 203–214 (1980).

30. Gao, C. Theory of menisci and its applications. *Appl. Phys. Lett.* **71,** 1801–1803 (1997).

31. Butt, H.-J. Capillary Forces: Influence of Roughness and Heterogeneity. *Langmuir* **24,** 4715–4721 (2008).

32. Megias-Alguacil, D. & Gauckler, L. J. Capillary forces between two solid spheres linked by a concave liquid bridge: Regions of existence and forces mapping. *AIChE J.* **55,** 1103–1109 (2009).

33. Koos, E., Kannowade, W. & Willenbacher, N. Restructuring and aging in a capillary suspension. *Rheol. Acta* **53,** 947–957 (2014).

34. Pietsch, W. Haftkraft, Kapillardruck. Flüssigkeitsvolumen und Grenzwinkel einer Flüssigkeitsbrücke zwischen zwei Kugel. *Chemie Ing. Tech.* **15,** 885–893 (1967).

35. Bossler, F. & Koos, E. Structure of particle networks in capillary suspensions with wetting and non-wetting fluids. *Langmuir* (2016). doi:10.1021/acs.langmuir.5b04246

36. Strauch, S. & Herminghaus, S. Wet granular matter: a truly complex fluid. *Soft Matter* **8,** 8271–8280 (2012).

37. Kenneth A. Brakke. The Surface Evolver. *Exp. Math.* **1,** 141–165 (1992).

38. Manoharan, V. N., Elsesser, M. T. & Pine, D. J. Dense Packing and Symmetry in Small Clusters of Microspheres. *Science (80-.).* **301,** 483–487 (2003).

39. Fortini, A. Clustering and gelation of hard spheres induced by the Pickering effect. *Phys. Rev. E* **84,** 1–5 (2012).

40. Hoffmann, S., Koos, E. & Willenbacher, N. Using capillary bridges to tune stability and flow behavior of food suspensions. *Food Hydrocoll.* **40,** 44–52 (2014).

41. Zhang, Y. *et al.* Capillary Foams: Stabilization and Functionalization of Porous Liquids and Solids. *Langmuir* **31,** 2669–2676 (2015).

42. Dittmann, J., Koos, E. & Willenbacher, N. Ceramic Capillary Suspensions: Novel Processing Route for Macroporous Ceramic Materials. *J. Am. Ceram. Soc.* **96,** (2012).

43. Caglar, U. Studies of Inkjet Printing Technology with Focus on Electronic Materials. 81 (Tampere University of Technology, 2009). doi:978-952-15-2317-5

44. Ju, M. *et al.* Double screen printed metallization of crystalline silicon solar cells as low as 30 µm metal line width for mass production. *Sol. Energy Mater. Sol. Cells* **100,** 204–208 (2012).

45. Lewis, N. S. Toward cost-effective solar energy use. *Science* **315,** 798–801 (2007).

46. Buzby, D. High Aspect Ratio Screen Printing of Fine Line Conductive Thick Film Ink Crystalline Silicon Solar Cells. in *Printed Electronics & Membrane Switch Symposium* (2010).

47. Mette, A. New Concepts for Front Side Metallization of Industrial Silicon Solar Cells. (Albert-Ludwigs-Universität Freiburg im Breisgau, 2007).

48. STLER. Silicon solar cell scheme. Available at: http://static1.squarespace.com/static/53fd7af9e4b0f7be79dfaf45/t/541b9c8ce4b0462bd0ee3aa4/1411095693135/?format=750w. (Accessed: 29th January 2016)

49. Green, M. A. *Solar Cells - Operating Principles, Technology and System Application*. (University of NSW, 1992).

50. Horzel, J. *et al.* Advantages of a new metallisation structure for the front side of solar cells. in *13th European Photovoltaic Solar Energy Conference and Exhibition. Proceedings of the International Conference* 1368–73 (1995).

51. Hoornstra, J., Weeber, A. W., Moor, H. H. C. De & Sinke, W. C. The Improtance of Paste Rheology in Improving Fine Line, Thick Film Screen Printing of Front Side Metallization. in *Proceedings of 14th EPSEC* 823–826 (1997).

52. Alias, R. & Shapee, S. M. in *Rheology* (ed. De Vicente, J.) (InTech, 2012).

53. Binder, S. What an ideal metallization ink should look like - Ink development with respect to deposition technology. in *2nd Workshop on Metallization for Crystalline Silicon Solar Cells* (2010).

54. Song, L., Chen, C., Guo, T. & Zhang, W. Organic vehicle for electroconductive paste. (2013).

55. BASF. *PVP and more …*. Available at: www.luvitec.com. (Accessed: 18th Feb 2016)

56. SIGMA-ALDRICH. Terpineol. Available at: http://www.sigmaaldrich.com/catalog/product/sial/77663?lang=de&region=DE. (Accessed: 10th February 2016)

57. Nakahara, A. & Matsuo, Y. Imprinting memory into paste to control crack formation in drying process. *J. Stat. Mech. Theory Exp.* **2006,** P07016–P07016 (2006).

58. Leung, K.-T., Jozsa, L., Ravasz, M. & Neda, Z. Pattern formation: Spiral cracks without twisting. *Nature* **410,** 166 (2001).

59. Zarzycki, J., Prassas, M. & Phalippou, J. Synthesis of glasses from gels: the problem of monolithic gels. *J. Mater. Sci.* **17,** 3371–3379 (1982).

60. Dufresne, E. R. *et al.* Dynamics of fracture in drying suspensions. *Langmuir* **22,** 7144–7 (2006).

61. Dufresne, E. R. *et al.* Flow and Fracture in Drying Nanoparticle Suspensions. *Phys. Rev. Lett.* **91,** 224501 (2003).

62. Xu, Y., German, G. K., Mertz, A. F. & Dufresne, E. R. Imaging stress and strain in the fracture of drying colloidal films. *Soft Matter* **9,** 3735 (2013).

63. Man, W. & Russel, W. Direct Measurements of Critical Stresses and Cracking in Thin Films of Colloid Dispersions. *Phys. Rev. Lett.* **100,** 198302 (2008).

64. Tirumkudulu, M. S. & Russel, W. B. Cracking in Drying Latex Films. *Langmuir* **21,** 4938–4948 (2005).

65. Singh, K. & Tirumkudulu, M. Cracking in Drying Colloidal Films. *Phys. Rev. Lett.* **98,** 218302 (2007).

66. Scherer, G. W. Theory of Drying. *J. Am. Ceram. Soc.* **73,** 3–14 (1990).

67. Fratzl, P., Gupta, H. S., Fischer, F. D. & Kolednik, O. Hindered Crack Propagation in Materials with Periodically Varying Young's Modulus—Lessons from Biological Materials. *Adv. Mater.* **19,** 2657–2661 (2007).

68. Weingärtner, H. *Chemische Thermodynamik: Einführung für Chemiker und Chemieingenieure*. 221 (B. G. Teubner Verlag, 2003).

69. Ho, C. K. & Udell, K. S. Mass transfer limited drying of porous media containing an immobile binary liquid mixture. *Int. J. Heat Mass Transf.* **38,** 339–350 (1995).

70. Schwarzbach, J. & Schlünder, E. U. Fluidized bed drying of materials wetted with a binary liquid mixture. *Chem. Eng. Process. Process Intensif.* **32,** 13–32 (1993).

71. Terpineol. Available at: http://www.nky-kk.co.jp/english/products/terpineol.html. (Accessed: 25th June 2015)

72. Carl Roth. Low viscosity paraffin oil. Available at: https://www.carlroth.com/downloads/spez/de/9/SPEZ_9190_DE.pdf. (Accessed: 4th August 2016)

73. Merck KGaA. n-Octanol Safety Data Sheet. 1–10 (2013). Available at: http://www.merckmillipore.com/DE/de/product/1-Octanol,MDA_CHEM-820931#anchor_MSD. (Accessed: 17th March 2013)

74. BASF. DINP Diisononyl Phthalate. (2004). Available at: http://www2.basf.us/plasticizers/pdfs/TDS_DINP_October_2004.pdf. (Accessed: 4th August 2016)

75. in *Landolt-Börnstein - Group IV Physical Chemistry* (ed. Lechner, M. D.) **25,** 1–4 (Springer Berlin Heidelberg, 2009).

76. Thermexcel. Physical characteristics of water (at the atmospheric pressure). (2003). Available at: http://www.thermexcel.com/english/tables/eau_atm.htm. (Accessed: 8th August 2016)

77. NOVAMET. HCA-1 Conductive Nickel Flake. Available at: http://novametcorp.net/pdf/Datasheets/Novamet Conductive Nickel Flake HCA-1 01-15.pdf. (Accessed: 24th February 2016)

78. Hering, E., Bressler, K. & Gutekunst, J. *Elektronik für Ingenieure und Naturwissenschaftler*. (Springer Science and Business Media, 2014).

79. Pastoriza-Santos, I. & Liz-Marzán, L. M. Reduction of silver nanoparticles in DMF . Formation of monolayers and stable colloids. *Pure Appl. Chem.* **72,** 83–90 (2000).

80. Song, L., Chen, C., Guo, T. & Zhang, W. EP 2 590 177 A2. **2,** (2013).

81. Kim, J. Reduction of Silver Nitrate in Ethanol by Poly (N-vinylpyrrolidone). *J. Ind. Eng. Chem.* **13,** 566–570 (2007).

82. Shang, J., Flury, M., Harsh, J. B. & Zollars, R. L. Comparison of different methods to measure contact angles of soil colloids. *J. Colloid Interface Sci.* **328,** 299–307 (2008).

83. KRÜSS. *Practical contact angle measurement - Technical Note*. **TN314e,** 1–4 (2008).

84. Song, B. & Springer, J. Determination of Interfacial Tension from the Profile of a Pendant Drop Using Computer-Aided Image Processing. *J. Colloid Interface Sci.* **184,** 64–76 (1996).

85. Bashforth, F. & Adams, J. C. *An Attempt to test the Theory of Capillary Action*. (Cambridge University Press, 1883).

86. Arashiro, E. Y. & Demarquette, N. R. Use of the pendant drop method to measure interfacial tension between molten polymers. *Mater. Res.* **2,** 23–32 (1999).

87. Wollgarten, S. Food capillary suspensions. (Karlsruhe Institute of Technology, 2015).

88. Tadros, T. F. *Rheology of Dispersions*. (WILEY-VCH Verlag & Co. KGaA, 2012).

89. Mezger, T. G. *The Rheology Handbook*. (Vincentz Network GmbH& Co KG, 2006).

90. Pahl, M., Gleissle, W. & Hans-Martin Laun. *Praktische Rheologie der Kunststoffe und Elastomere*. (VDI Verlag GmbH, 1991).

91. Van der Pauw, L. J. A method of measuring specific resistivity and hall effect of discs of arbitrary shape. *Philips Res. Reports* **13,** 1–9 (1958).

92. Singh, Y. Electrical Resistivity Measurements: a Review. in *International Journal of Modern Physics: Conference Series* **22,** 745–756 (2013).

93. Van der Pauw Measurements. Available at: http://www.microwaves101.com/encyclopedias/van-der-pauw-measurements. (Accessed: 3rd January 2016)

94. Günzler, H. & Gremlich, H.-U. *IR Spectroscopy An Introduction*. (Wiley-VCH Verlag GmbH, 2002).

95. Pospischil, M. *et al.* Process Development for a High-throughput Fine Line Metallization Approach Based on Dispensing Technology. *Energy Procedia* **43,** 111–116 (2013).

96. Zhang, D., Moyer, J. & Zhang, W. Front contact pastes with increased aspect ratio to achieve higher efficiency on screen printed solar cells. 1321–1324 (2009).

97. Itoh, U. *et al.* Screen printed finger electrode with high aspect ratio by single printing for crystal Si solar cell using novel screen mask. *Conf. Rec. IEEE Photovolt. Spec. Conf.* 2167–2170 (2012). doi:10.1109/PVSC.2012.6318026

98. Vogel, H. J., Hoffmann, H. & Roth, K. Studies of crack dynamics in clay soil: I. Experimental methods, results, and morphological quantification. *Geoderma* **125,** 203–211 (2005).

99. Domenech, T. & Velankar, S. S. On the rheology of pendular gels and morphological developments in paste-like ternary systems based on capillary attraction. *Soft Matter* **11,** 1500–1516 (2015).

100. AZO Materials. Titanium Dioxide. Available at: http://www.azom.com/properties.aspx?ArticleID=1179. (Accessed: 18th Oct 2015)

101. Kumar, P. M., Badrinarayanan, S. & Sastry, M. Nanocrystalline TiO2 studied by optical, FTIR and X-ray photoelectron spectroscopy: correlation to presence of surface states. *Thin Solid Films* **358,** 122–130 (2000).

102. Gao, Y., Masuda, Y., Peng, Z., Yonezawa, T. & Koumoto, K. Room temperature deposition of a TiO2 thin film from aqueous peroxotitanate solution. *J. Mater. Chem.* **13,** 608–613 (2003).

103. Demond, A. H. & Lindner, A. S. Estimation of Interfacial Tension between Organic Liquids and Water. *Environ. Sci. Technol.* **27,** 2318–2331 (1993).

104. Faddoul, R., Reverdy-Bruas, N., Blayo, A., Haas, T. & Zeilmann, C. Optimisation of silver paste for flexography printing on LTCC substrate. *Microelectron. Reliab.* **52,** 1483–1491 (2012).

105. Wu, Y., Eliyahu, J., Liu, P. & Hu, N.-X. Conductive Silver Paste and Conductive Film formed using the same. (2012).

106. Quemada, D. Rheology of concentrated disperse systems and minimum energy dissipation principle - I. Viscosity-concentration relationship. *Rheol. Acta* **16,** 82–94 (1977).

107. Keene, B. J. Surface Tensions. Available at: http://www.kayelaby.npl.co.uk/general_physics/2_2/2_2_5.html> (2015). (Accessed: 26th Aug 2015)

108. Evonik. AEROSIL® fumed silica - more than just a powder. Available at: https://www.google.de/url?sa=t&rct=j&q=&esrc=s&source=web&cd=1&cad=rja&uact=8&ved=0ahUKEwisxLjTmOzNAhWrCpoKHSSBA20QFggeMAA&url=http://www.aerosil.com/product/aerosil/en/products/Pages/default.aspx&usg=AFQjCNErtqtJch_Cb0Rb0Sw37RdX6sYF8Q&sig2=pubK38oLJswyJl. (Accessed: 19th Aug 2015)

109. Kuder, H. R., Sanchez, J. G., Gao, X. & Grossmann, M. Sinterable silver flake adhesive for use in electronics. (2012).

110. Kirtley, J., Eigenbrodt, B. & Walker, R. In Situ Optical Studies of Oxidation Kinetics of Ni/YSZ Cermet Anodes. *ECS Trans.* **33,** 25–37 (2010).

111. Noskov, B. a, Akentiev, a V & Miller, R. Dynamic Surface Properties of Poly(vinylpyrrolidone) Solutions. *J. Colloid Interface Sci.* **255,** 417–424 (2002).

112. Weaver, J. F. & Hoflund, G. B. Surface Characterization Study of the Thermal Decomposition of AgO. *Chem. Mater.* **6,** 8519–8524 (1994).

List of figures

Fig. 1. Left: Ternary diagram of particle-liquid-liquid systems showing the approximate regions of stability as a function of the relative volume fractions. Right: Corresponding diagram showing the particle-liquid-liquid systems in the different states, when increasing the fraction of the preferentially wetting liquid.[24] 4
Fig. 2: Pendular, liquid bridge between two adjacent particles. Left: Particles directly in contact. Right: particles are separated by distance s.[26,27] 5
Fig. 3: (a) Yield stress as function of saturation S shown for a capillary state network: polyvinyl chloride (PVC) particles in water with diisononyl phtalate (DINP) as secondary liquid. And for a pendular state network: hematite particles suspended in DINP with water as secondary liquid.[10] (b) 3D network of capillary suspensions with varying three phase contact angles: 40°(a), 61°(b) and 94°(c).[35] The secondary liquid is highlighted yellow. The secondary liquid fraction during sample preparation was equal for each image. 7
Fig. 4: Minimum energy regions for various particle clusters as a function of the normalized secondary fluid droplet volume V_l and the wetting angle θ.[8] 8
Fig. 5: Scheme of a silicon solar cell with a p- and n-type layer. The electric circuit is closed by the back and front contacts on the cell.[48] 9
Fig. 6: Incident light hits the silicone surface by direct reflection from the metallization and by indirect reflection from the glass/air interface. From left to right: Profile of a typically plated contact, an advanced plated contact[50] and a screen printed contact.[47] 10
Fig. 7: a) Schematic of screen printing: squeegee pushes the ink through a pretreated mesh.[3] b) Shear rate and viscosity function for a screen printing process as function of time.[52] 11
Fig. 8: Overview of weight fractions of polymers, solvents and solids in a thick film printing paste (average is abbreviated with Ave in the image).[46] 11
Fig. 9: Crack patterns: (a) isotropic cellular, (b) radial, (c) lamellar and (d) spiral crack growth. [57,58] Image width of (a) is 150 mm, the discs in (b) and (c) each have a diameter of 500 mm. 12
Fig. 10: (a) Particle size distribution q_3 by volume for the used nickel spheres and flakes, ZnO and TiO_2. Irregular shapes of the (b) nickel flakes and (c) TiO_2 particles. 15
Fig. 11: Conductivity and temperature as function of time for nickel particles in a DMF-water solution. 17
Fig. 12: Sessile drop of fluid B placed on a solid surface surrounded by fluid A with $\rho_A < \rho_B$. The three phase contact angle θ_{2l} is formed between baseline (substrate) and the droplet contour tangent. 18
Fig. 13: Geometry of a pendant drop.[86] 20
Fig. 14: (a) Plate/plate geometry with radius R_{plate} and gap height h_{gap}. (b) Vane geometry with diameter d_{vane}.[87] 20

Fig. 15: Deformation as function of shear stress for TiO_2 particles suspended in octanol with S=0.05 and the evaluation of the yield stress σ_y via tangent method. 21
Fig. 16: Schematic of a capillary rheometer. The piston is moved with velocity v towards the capillary with length L_{nozzle} and diameter D_{nozzle}. The pressure transducer P records the difference in pressure between sample chamber and the ambient pressure. 22
Fig. 17: Left: Storage and loss modulus as function of applied stress in an amplitude sweep measurement. Right: Example of the applied stress as function of time (in a structure recovery measurement). The critical stress values σ_{LVE} and $\sigma_{cross\text{-}over}$ have been determined in the preceding amplitude sweep. Frequency f=1 Hz is kept constant for all three stress periods. 24
Fig. 18: Schematic of a dispenser. Ink is stored in a reservoir and pushed through a nozzle by applying a defined pressure. The dispenser is moved across the substrate at a certain velocity. Optionally, the substrate is moved while the dispenser remains fixed. 25
Fig. 19 Set-up for the Van-der-Pauw measurement with four point contacts: A. B, C and D. 26
Fig. 20: Interaction of infrared beam at the ATR crystal/sample interface with the specific refractive index n_1 of the internal reflection element and the refractive index of the sample n_2. d_{pen} marks the depth of penetration of the IR beam. 27
Fig. 21: Infrared absorbance spectra of the pure substances of the capillary suspension annotated with characteristic peaks for tracing the different substances. 28
Fig. 22: a) Yield stress as function of the saturation S for TiO_2 dispersed in n-octanol ($\phi = 0.04$ and $\phi = 0.05$) and different water fractions varying from S=0.00-0.07. b) Corresponding normalized yield stress values for S=0.00-0.07. 29
Fig. 23: a) Storage modulus $G'$and loss modulus G'' for TiO_2 in n-octanol and water as secondary liquid with $S = 0.00 - 0.07$. Measurement frequency f=1Hz. b) Stress at the cross-over of G' and G'' ($\sigma_{cross\text{-}over}$) as function of saturation resulting from the oscillatory measurements shown on the right. Inset shows the linear correlation of yield stress σ_y and cross-over stress $\sigma_{cross\text{-}over}$. 30
Fig. 24: Low shear (full symbols) and high shear (open symbols) viscosity as function of the shear rate $\dot{\gamma}$ for TiO_2 capillary suspensions in n-octanol and water as secondary liquid with $S = 0.00$, $S = 0.03$ and $S = 0.05$. 31
Fig. 25: (a)-(c) Response of TiO_2 capillary suspensions to large amplitude oscillatory shear (LAOS) with $S = 0.00$ (a), $S = 0.03$ (b), $S = 0.05$ (c). Storage modulus G' (symbol: triangles) and loss modulus G'' (symbol: squares) were measured before and after exposing the sample to LAOS. Measurement frequency: 1 Hz. (a) $S = 0.00$, (b) $S = 0.03$, (c) $S = 0.05$. (d) Corresponding phase shift angle δ as function of time. 32
Fig. 26: Wet lines printed with a dispenser using TiO_2 capillary suspensions in n-octanol with added water. Saturation S varies from a) $S = 0.00$, b) 0.03 and c) 0.05. 34

Fig. 27: a) Line width of printed TiO_2 suspensions as function of yield stress for $S = 0.00$, 0.03 and 0.05 (from left to right). b) Corresponding contact angle α and aspect ratio AR without secondary liquid and for S=0.03 and $S = 0.05$. 35
Fig. 28: a) Surface morphology after drying and b) yield stress σ_y prior to drying for TiO2 particles dispersed in n-octanol with $\phi = 0.04$ and increasing amounts of secondary liquid S. c) Area density M_0 after drying as function of saturation S. The data point at $S = 0.07$ with 10 vol% surfactant Tego Dispers 752W in the secondary liquid is additional shown in the lower right image and as a star in (b) and (c)..... 36
Fig. 29: Particle distribution in a non-stabilized particle suspension (left) and in a capillary suspension (right) at various times during drying..... 37
Fig. 30: Dry surface pattern of a) ZnO and c) Al_2O_3 films. Particles were dispersed in n-octanol and stabilized as capillary suspension with H_2O ($\phi_{\mathrm{ZnO}} = 0.05$, $\phi_{\mathrm{Al_2O_3}} = 0.20$). Yield stress for b) ZnO and d) Al_2O_3 in n-octanol and different fractions of water..... 38
Fig. 31: (a-c) Infrared absorption spectra and (d-f) surface integrals of TiO_2 capillary suspensions with three different D_2O saturations as function of drying time..... 39
Fig. 32: a) Nickel particles in paraffin oil ($\phi = 0.20$) with increasing amounts of water-DMF-mixture as a secondary liquid. The samples change from a weak gel without added fluid to a strong, stiff gel with added secondary liquid due to the formation of a capillary state network. b) Increase in the yield stress σ_y for nickel and silver particles dispersed in terpineol with increasing amounts of distilled water. Both systems are in the capillary state and have a solid volume fraction of $\phi = 0.29$..... 41
Fig. 33: a) Normalized yield stress as function of secondary fluid content for nickel capillary suspensions with paraffin oil as bulk fluid and different secondary liquids: DMF, DMF/H_2O-mixture (1:1 by vol.), and pure H_2O. The inset shows the yield stress σ_y normalized by the Laplace pressure (Γ/r). The solid volume fraction for all material combinations shown is $\phi = 0.20$. b) Viscosity η of nickel in terpineol suspensions ($\phi = 0.29$) as function of shear rate $\dot{\gamma}$ for varying water fractions. The dashed line shows the estimated high shear viscosity for the given solid loading assuming hard sphere particles.[105]..... 42
Fig. 34: Bulk resistance R for a) nickel and b) silver capillary suspensions ($\phi_{Ag/Ni} = 0.29$) compared to commercial paste formulations. For the nickel, the conventional formulations were prepared according to a Heraeus patent with an organic vehicle (ov) and two different thixotropic agents (Aerosil R805 and Aerosil 150) using the same particle fraction. Heraeus I and II are commerical silver pastes (solid volume fraction 90.0 and 90.5 wt%, respectively). In addition, a silver capillary suspension with 5 vol% water and 5 wt% solder glass is also shown ($\phi_{total} = 0.33$). Variance in sheet thickness was measured and considered in the calculation of the bulk resistance. 44
Fig. 35: Sheet thickness obtained for a) nickel and b) silver capillary suspensions ($\phi_{\mathrm{Ag/Ni}} = 0.29$) compared to commercial paste formulations. For the nickel system, the conventional formulations were prepared according to a patent (ref) using an organic vehicle (ov) and two different thixotropic

agents (Aerosil R805 and Aerosil 150) using the same particle fraction. Heraeus I and II are commercial silver pastes (solid volume fraction 90.0 and 90.5 wt%, respectively). In addition, data for a silver capillary suspension with 5 vol% water and 5 wt% solder glass is also shown ($\phi_{\text{total}} = 0.33$). 46
Fig. 36: Wet contact lines for a) nickel and c) silver suspensions using a mask of width 300 µm (red vertical lines). The light grey areas and black spots are from the pure solvent, where the contrast is controlled by the drop height. Cross sectional profile for lines printed with b) nickel and d) silver capillary suspensions. All suspensions were prepared in terpineol with varying amounts added water and have a solid fraction $\phi = 0.29$. Additionally, a commercial silver sample (Heraeus I) is plotted for comparison with the silver capillary suspensions. 47
Fig. 37: a) Yield stress as function of added secondary liquid amount for three different solid compositions of nickel spheres and flakes. Bulk fluid: paraffin oil, secondary liquid: DMF. b) Bulk resistance for two different solid compositions as function of the secondary liquid amount. Total solid loading $\phi = 0.25$ is constant for all samples shown here.)..... 49
Fig. 38: Sheet thickness of capillary suspensions made with a mixture of nickel spheres and flakes measured after the sintering process..... 50
Fig. 39: a) Yield stress of nickel spheres dispersed in paraffin oil and different amounts of water as secondary liquid. Additionally yield stress of a capillary suspension is plotted where an aqueous silver dispersion was used as secondary liquid. b) Corresponding bulk resistance for two different sintering atmospheres: pure nitrogen and a mixture of nitrogen and 5 vol% hydrogen..... 51
Fig. 40: a) Yield stress for nickel based capillary suspensions made with particles with a diameter of 3-7 µm and additionally sub-micron sized particles as function of the secondary liquid content. Yield stress function with purely 3-7 µm sized particles is also given for comparison. b) Bulk resistance for the sinterd capillary suspensions made with polydisperse sized nickel particles as function of the added secondary liquid amount. Nickel was dispersed in paraffin oil with water as secondary liquid. Sintering atmosphere was nitrogen and alternatively a nitrogen/hydrogen mixture. 53
Fig. 41: Silver particles dispersed in DINP. Left: without added secondary liquid. Right: After the addition of 0.3 vol% of water. 54